UC Berkeley
UC Berkeley Electronic Theses and Dissertations

Title

Investigating the Structure and Downstream Biology Effects of the Juxtamembrane Domain of the Epidermal Growth Factor Receptor

Permalink

https://escholarship.org/uc/item/90n0542c

Author

Chang, Hsun-Hui

Publication Date

2022

Peer reviewed|Thesis/dissertation

Investigating the Structure and Downstream Biology Effects of the Juxtamembrane Domain of

the Epidermal Growth Factor Receptor

By

Hsun-Hui Chang

A dissertation submitted in partial satisfaction of the

requirements for the degree of

Doctor of Philosophy

in

Chemistry

in the

Graduate Division

of the

University of California, Berkeley

Committee in charge:

Professor Alanna Schepartz, Chair
Professor Eunyong Park
Professor Christopher Chang

Spring 2023

Abstract

Investigating the Structure and Downstream Biology Effects of the Juxtamembrane Domain of the Epidermal Growth Factor Receptor

Hsun-Hui Chang
2022

The Epidermal Growth Factor Receptor (EGFR),[1] also known as ErbB1 or HER1 in humans, is a member of the ErbB family.[2] EGFR is a receptor tyrosine kinase (RTK) responsible for communicating cellular signaling across the plasma membrane related to cell proliferation, metabolism, and migration.[3,4] EGFR mutations and overexpression are known to be related to cancer.[5–7] Thus, understanding EGFR biology and the molecular mechanism of EGFR activation can lead to important therapeutic strategies. The importance of the juxtamembrane (JM) domain of the EGFR has gathered attention as evidence showed that its intermolecular and intramolecular interactions are crucial for EGFR function.

In this dissertation, I describe my graduate work in four chapters detailing the study of the EGFR JM function and its role in regulating the downstream biology of the EGFR.

Chapter 1: This chapter builds on the literature review and previous efforts, introducing the role and importance of EGFR in cellular biology, and the role of the JM domain in EGFR activation. In this chapter, JM structure and the manipulation to affect EGFR signaling were described.

Chapter 2: This chapter describes peptides mimicking the JM domain dimer in activated EGFR used for high-resolution structural studies. The designs of these JM-mimicking peptides were detailed. Peptide synthesis, purification, and characterizations that reveal the secondary structure were discussed.

Chapter 3: Looking beyond the JM domain, the structural study described in this chapter focused on peptides containing both the transmembrane domain (TM) and the JM domain segment to investigate the allosteric relationship within EGFR. Preparation and characterization of membrane mimics that stabilize TM-containing peptides were reported.

Chapter 4: In the final chapter, I report a collaborative work I partake that reveals the effect of JM structure and conformation on EGFR biology in terms of cellular trafficking and receptor degradation. Another preliminary work using APEX2-based proximity labeling toward mass spectrometry proteomics was reported. Finally, this chapter summarized the outlook on future directions following the groundwork laid out in the scope of this dissertation.

Acknowledgements

These past five years have been such a journey. I am grateful to so many people that are generous with supporting one another and sharing their talents. First, I am incredibly grateful for Professor Alanna Schepartz and her mentorship as my thesis advisor. Alanna is a mentor that has an incredible infectious passion for science and that has affected me and the people around me. Her participation in discussing my work and growth has been a great inspiration for me. I learn from her how to be a responsible and diligent scientist. I am grateful for her support and input on my research as well as on a personal level. For the past few years, the lab and the world have seen some unprecedented changes. However, Alanna has been a strong and supportive presence in our lives during these uncertain times. Alanna is dedicated to cultivating a positive and collaborative lab environment and people have followed her vision. It is wonderful to work in such an environment. I am grateful for her leadership and scientific insight.

I would like to thank my former committee members Professor Pat Loria and Professor Elsa Yan at Yale University for their guidance in the early stages of my Ph.D. program. I would like to thank my current committee members Professor Christopher Chang, Professor Eunyong Park, Professor John Kuriyan, and Professor Daniel Nomura for joining my committee on short notice during the height of the COVID lockdown, right after our lab settled in UC Berkeley. I am grateful for the resources I enjoyed during my time at UC Berkeley. I would like to thank Jeff Pelton and Mark Kelly for helping me with NMR training, experimental advice, and data collection. Thank you to Miriam Hood from the Marqusee Lab who trained me to use their circular dichroism instrument and answers my questions. Thank you to Alison Lui from the Landry lab who trained me to use their dynamic light scattering instrument and shared her data processing tools with me. Thanks to Karen Wong for her brilliance and generosity in her job that not only make all our lives easier, but her warm presence brings joy to my lab life.

I am forever grateful for all who I have had the fortune to work with during my Ph.D. journey. First, my mentors: Dr. Deepto Mozumdar, Dr. Rebecca Wissner, and Dr. Kim Quach. Deepto is such an enthusiast when it comes to science and music. I enjoyed working with him and exchanging thoughts on music and TV shows. I am grateful to be able to share my lab life and personal life with such a friend and a mentor. Rebecca was my mentor when I was a first-year Ph.D. rotating student. She showed me how to be a scientist, how to balance one's focus between multiple goals, and how to train oneself in unfamiliar tasks. Kim was my mentor in the second year of my Ph.D. He trained me on the ins and outs of peptide chemistry, which helped me immensely to propel my research in the initiation stages. Thank you to Dr. Susan Knox and Dr. Aarushi Gupta for letting me join their outings and gatherings which always make me feel included. Thank you to Neville Dadina, Kelsey Zhang, and Tent Tangpradabkul for being the source of joy and warmth in the lab. Life in the lab is always better when they are around. Thank you to Neville and Kelsey for being my cell-lab family. I am always experiencing their generosity when I needed help with cell lab work or microscopy questions. Thank you to Pixie Piszkiewicz, Noah Hamlish, Héctor L. Torres Vera, Riley Fricke, and Meghan Pressimone for bringing care and warmth to the corners of the lab. Thanks to Raina Kasera for being an excellent mentee asking important questions and dedicating her time to the projects. Thank you to all the lab members that I have not named one by one for having the fortune to work with. I have always felt supported professionally and personally in the lab. Although I only spent two years at Yale University, I am grateful to the member is the Loria research group for welcoming me into their

Table of Contents

Chapter 1. The juxtamembrane domain of the epidermal growth factor receptor is a critical regulatory domain for the receptor function

Chapter 1. The juxtamembrane domain of the epidermal growth factor receptor is a critical regulatory domain for the receptor function

1.1.   Introduction

The Epidermal Growth Factor Receptor (EGFR),[1] also known as ErbB1 or HER1 in humans, is a receptor tyrosine kinase (RTK) belonging to the ErbB family[2] involved in cell proliferation, metabolism, and migration.[3,4] It is also known to be related to many human cancers.[5–7] Seven growth factors have been identified to bind to EGFR and regulate cellular responses.[8] These growth factors including epidermal growth factor (EGF), transforming growth factor α (TGF-α), epigen (EPI), epiregulin (ER), betacellulin (BC), heparin-binding EGF (HB-EGF), and amphiregulin (AR). The binding of the growth factor activates EGFR and transmits extracellular information into distinct intracellular phenotypes (**Figure 1.1**).[9–15]

EGFR is a single-pass transmembrane protein that is 1186-amino-acid long and consists of five domains. The five domains are the extracellular domain (ECD), the transmembrane domain (TM), the juxtamembrane domain (JM), the kinase domain (KD), and the C-terminal tail (C-tail) (**Figure 1.2.A**).[16] Upon binding of growth factors to its ECD, EGFR activates and dimerizes forming several dimerization contact points with its homodimer counterpart: ECD, TM, JM, and KD. Structural changes propagated from the ECD, through the TM, and the JM, and subsequently activated the kinase domain (KD).[16–18] Autophosphorylation of the EGFR leads to C-term phosphorylation patterns that could be recognized by intracellular protein partners to transduce information to downstream signaling pathways (**Figure 1.2.B**). The EGFR activation mechanism was revealed from high-resolution structures of the EGFR ECD bound the growth factors (EGF,[19,20] TGF-α,[20,21] EPI,[13] and ER[13]), showing distinct structures induced by specific growth factors. However, these studies only answered how growth factor identities were decoded by the ECD. The questions on how this information is propagated across the membrane allosterically via EGFR activation remain abundant. Since the 2000s, the 37-residue small segment at the intracellular side juxtamembrane domain (JM) has gathered attention.[22–26] It is believed to be the key to how EGFR encodes information decoded from ECD, and subsequently facilitated autophosphorylation and protein partner interaction.

1.2.   The juxtamembrane domain

The juxtamembrane domain is a short segment following the C-terminal of the TM, located at the center bridging the EGFR signal-receiving domain ECD, and the functional KD. Abnormality in this region is discovered to be related to cancer: (i) Mutation within the JM can was found in lung cancer,[27] and (ii) binding to inhibit JM dimerization suppressed cancer cell proliferation.[28] These finding that the abnormal JM domain activity is oncogenic hinted at the important regulatory role JM serves in EGFR signal transduction.

The deletion of the JM segment significantly affects EGFR function. EGFR constructs lacking JM segment showed reduced dimerization *in vitro*,[23] reduced tyrosine kinase activity (~65-95% *in vitro*; 95% *in cellulo*),[25] and reduced catalytic efficiency (~10-70 fold reduction in kcat/Km *in vitro*).[23] EGFR constructs where the JM was replaced by an unstructured sequence (GGS)$_{10}$ resulted in reduced autophosphorylation *in cellulo*.[22]

The importance of the JM domain can be explained by its structural importance in the activated EGFR dimer. The JM domain can be further divided into JM-A and JM-B segments (**Figure 1.2.A**).

In an activated EGFR dimer, the JM-A segment forms α-helices and assembles into an antiparallel coiled coil and interacts with the plasma membrane,[23,29] and the JM-B interacts with the KD. The JM-B segment contributes to the stabilization of the active asymmetric kinase dimer.[17] Crystallography structure of EGFR[27] and HER4[23,30] reveal interactions between the JM-B and kinase domain. In this crystal structure, the JM-B connected to the asymmetric 'receiver' kinase latches around the C-lobe of the 'activator' kinase (**Figure 1.3**). This was further collaborated by alanine scanning mutagenesis of the JM-B identifying the residue responsible for interactions that affect growth-factor-dependent autophosphorylation activity *in cellulo*.[27]

1.3.   JM-A coiled coil conformation encodes the identity of the ECD-bound growth factor

The mechanism proposed on charge-stabilization between the plasma membrane and JM-A coiled coil conformation[23,29] lead to the hypothesis that there is a relationship between JM-A structure tunability and EGFR signaling. To investigate the JM-A conformation, Schepartz and colleagues made use of a chemical biology tool called the bipartite tetracysteine display.[31–33] (**Figure 1.4**) Bipartite tetracysteine display uses a bis-arsenical dye as ReAsH[31–34] (**Figure 1.4.A**) as a fluorescence sensor. The ReAsH dye is fluorogenic when the two arsenic center coordinate to the four proximate Cys side chains, restricting the rotational motion of the As-Aryl bond rotation that quenches the fluorescence (**Figure 1.4.A**).[35] Thus, this chemical tool is useful in reporting on protein conformation, commonly used to detect the presence of coiled coil conformation.[31,33] With properly designed tetracysteine motifs, ReAsH fluorescence assay can report on protein conformation even in complex environments such as mammalian cells.[31,32]

In the initial study done in the Schepartz group, Scheck and colleagues designed a series of full-length EGFR variants with rationally placed Cys side chain pairs in the JM region to test the hypothesis that the intracellular JM-A segment assembles into an antiparallel coiled coil upon EGF binding *in cellulo*.[36] Results reported that when mammalian cells expressing full-length EGFR were treated with EGF, the JM-A dimer adopts an antiparallel coiled coil conformation,[36] consistent with previously reported JM-A structure (**Figure 1.4.B**).[23]

This 'EGF-type' conformation, the coiled coil dimer is characterized by a hydrophobic inter-helix interface resembling a leucine-zipper (with L655, L658, and L659 interacting with the coiled coil counterpart), and exposing the charged residues (K652, R656, R657, E661, and E663) on the outside of the coiled coil.[23,36] An alternatively coiled coil conformation was observed when cells expressing EGFR were treated with TGF-α. This "TGF-α type' conformation forms an inter-helix interface exhibiting polar interaction and exposing hydrophobic leucine residues (**Figure 1.4.C**).[36] This 2012 work done by Scheck and colleagues demonstrated the presence of two distinct JM-A coiled coil dimer conformations induced allosterically by growth factor EGF and TGF-α binding.

The subsequent work done by Doerner and colleagues investigating seven different growth factors binding on EGFR revealed that these growth factors bring about 'EGF-type' and 'TGF-α-type' outcomes. EGF or HB-EGF binding to EGFR induced hydrophobic inter-helix interface 'EGF-type' coiled coil while TGF-α, EPI, ER, and AR binding induced polar inter-helix interface 'TGF-α-type' coiled coil (**Figure 1.5**). A third conformation with an intermediate coiled coil interface was also identified with the binding of BC.[37] Notably, the division between the EGF-type growth factor (EGF, HB-EGF) and the TGF-α-type growth factor (TGF-α, EPI, ER, and AR) correlates to the downstream signaling outcomes elicited by these two groups of growth factors.[11,13–15] EGF, HB, or BC leads to greater receptor downregulation and a shorter signaling pulse, whereas activation

with TGF- α,[15] AR, ER,[13] or EPI[13] promote receptor recycling,[9,11,38] sustained signaling,[39,40] and increased cell proliferation.[41,42] These previous studies revealed that binding of a growth factor to the ECD induces the formation of one of the two rotationally isomeric coiled coil conformations of the JM, demonstrating the allosteric relationship between the ECD and the JM domains of EGFR.

1.4.   Allosteric coupling of the JM-A coiled coil structures to the TM domains of EGFR

As described in the previous section, the allosteric relationship between the ECD and the JM has been reported. Rationally, the subsequent investigation focused on how the allosteric network communicates the extracellular ECD structural information to the intracellular JM. Overlaying crystal structures of the EGFR EGF-bound ECD[19] and TGF-α-bound ECD[21] exhibit clear structural differences in ECD subdomain IV. Thus, the attention was expended on the TM, the domain that sits between the ECM and the JM, which has been hypothesized to propagate ECD structural changes across the membrane. To probe TM structure, Sinclair and colleagues first focused on probing the TM homodimer structural interaction via inter-chain cross-linking experiments (**Figure 1.6.A**).[43] Using a series of EGFR variants of single cysteine substitution within the TM, the authors were able to identify changes in TM dimer cross-linking with dependent on the ECD growth factor binding. The level of EGFR TM (particularly at residues 624-629) cross-links was high when ECD binds EGF, HB-EGF, BC and low when binds TGF-α, AR, demonstrating a growth-factor-dependent TM dimer conformation (**Figure 1.6.B**). The authors then investigated the structural relationship between the TM and the JM *in silico* via molecular modeling (Rosetta-MPDock)[44–46] and Monte Carlo simulations (MPRelax)[45–47] starting with the reported the NMR structure of the TM-JM fragment.[48] The EGFR TM-JM conformational *in silico* landscape yielded TM-JM conformations distribution with the following observations: (i) larger TM cross-angles were associated with the formation of the TGF-α-type coiled coil within the JM, and (ii) differences in the TM helix dimer cross-location translate into different JM coiled coil conformation (**Figure 1.6.C**).

Finally, the authors studied TM mutants at the traditional GXXXG motif[49–51] to investigate the effects on the JM coiled coil conformation. GXXXG motif residues (G625, G628, or A629) were mutated to either a small, non-polar residue (Ala or Gly), bulky and hydrophobic residue (Phe), or amino acids (G625I and G628V) that affect EGFR activity. G625I and G628V were reported to disrupt the dimerization of TM.[52,53] G628V resulted in reduced levels of receptor internalization and persistent EGFR activation and signaling towards MAPK.[54] Using bipartite tetracysteine display and mutagenesis, Sinclair and colleagues identified TM mutations that can switch the JM conformation bias to either the EGF-type or TGF-α-type coiled coil.

1.5.   Decoupling of the JM-A coiled coil conformation and the growth factor identity

In the previous section, I described the work by Sinclair and colleagues to identify TM mutations that can switch the JM conformation bias to either the EGF-type or TGF-α-type coiled coil (**Figure 1.6**).[55] A set of EGFR variants with a single mutation on the Gly residue at position 628 were identified. When Gly was mutated to another small, non-polar residue Ala (G628A), the mutation was conservative and was assumed to exhibit no significant changes in structure. The effect on JM thus was expected to be consistent with the wild type. When Gly was mutated to bulky and

hydrophobic residue Phe (G628F), the JM conformation exhibited the EGF-type coiled coil when treated with either EGF or TGF-α. When Gly was mutated to known mutation Val (G628V),[54] the JM conformation exhibited the TGF-α-type coiled coil in cases when the receptor was treated with EGF or TGF-α. This set of G628 mutations demonstrated allosteric control of the JM domain with TM mutations, as well as decoupled the JM coiled coil conformation and the ECD-bound growth factor identity.

1.6.   The juxtamembrane domain is a hotspot for cellular interactions

In addition to its role in supporting kinase activation, the JM region of EGFR is also a hotspot of interactions with diverse cellular components, many of which modulate EGFR signaling and downstream biology. One example is the electrostatic interaction of basic residues in the JM-A with the anionic phospholipids present in the inner leaflet of the cell membrane.[29,56,57] This interaction provides an additional layer of receptor auto-inhibition in the absence of growth factor activation,[26,56] by reducing the proximity of JM-A helices from adjacent monomers thereby preventing their dimerization. The JM region has also been shown to interact with many intracellular proteins, such as calmodulin,[29,58–62] the Nck adaptor protein,[63] the stimulatory GTP binding protein (GaS),[64] the phosphatidylinositol-4-phosphate kinase (PI4P, or PIP),[65] the protein kinase C (PKC),[66–69] p38 MAPK,[70,71] AP2,[72,73] TRAF4,[74] and ARNO (**Figure 1.7**).[75] **Table 1** lists the details of (1) the experiments evaluating these interactions, (2) the binding sites of these protein interactors, and (3) their observed and proposed biological effects. Notably, the JM contains many sites and cryptic motifs that were recognized by intracellular machinery to elicit receptor upregulation (T669; phosphorylation by p38MAPK reduces EGFR downregulation), receptor downregulation (T654; phosphorylation by protein kinase C attenuates EGFR activity), a dileucine motif (recognized by AP-2 for clathrin-mediated endocytosis), basolateral sorting[76] and nuclear translocation.[77]

1.7.   Conclusion

In this chapter, I discussed the importance of the juxtamembrane region of the EGFR to the receptor's function in cellular signaling. The JM has been proven to be essential for EGFR activation that deletion of the JM region[23,25] or replacement with unstructured sequence[22] leads to reduced EGFR kinase activity. Both JM-A and JM-B segments are crucial to EGFR function. The latter interacts with the KD to support kinase dimerization and activation.[17,27] The former encodes the ECD information discovered by the important bipartite tetracysteine display[31,33] method expanded by the Schepartz group.[32,35] These studies not only revealed the allosteric relationship between the ECD and the JM through the discovery of distinct JM coiled coil conformation encoding the growth factor identity.[36,37] These studies also correlated the JM coiled coil structure alteration to cellular responses downstream of EGFR activation events. The understanding of the EGFR mechanism was further broadened by the studies, focusing on the allosteric relationship to the TM domain. The TM cross-angles and cross-locations were correlated to different JM coiled coil conformation *in silico*.[55] The decoupling of the JM structure with the growth factor identity ECM by TM mutations *in cellulo* opened the door to more opportunities to ask important questions with the control on JM conformation. Finally, the role of JM as the interaction hotspot of cellular interactions was reviewed. These interactions are involved in a host of cellular biology: from kinase signaling to receptor upregulation and

downregulation, from endocytosis to nuclear translocation. Overall, previous studies demonstrated the modulatory roles of the JM in EGFR through structural and functional studies.
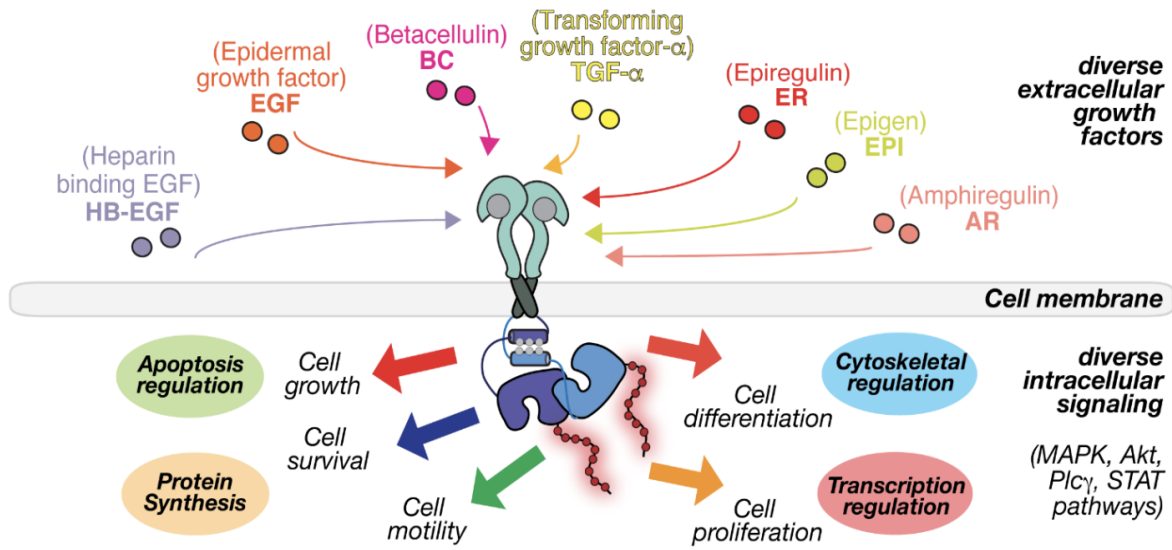
Figure 1.1. Schematic illustration of EGFR growth factor and the diverse downstream signaling outcomes that are critical for cellular functions. Figure adapted from Ref. [78]
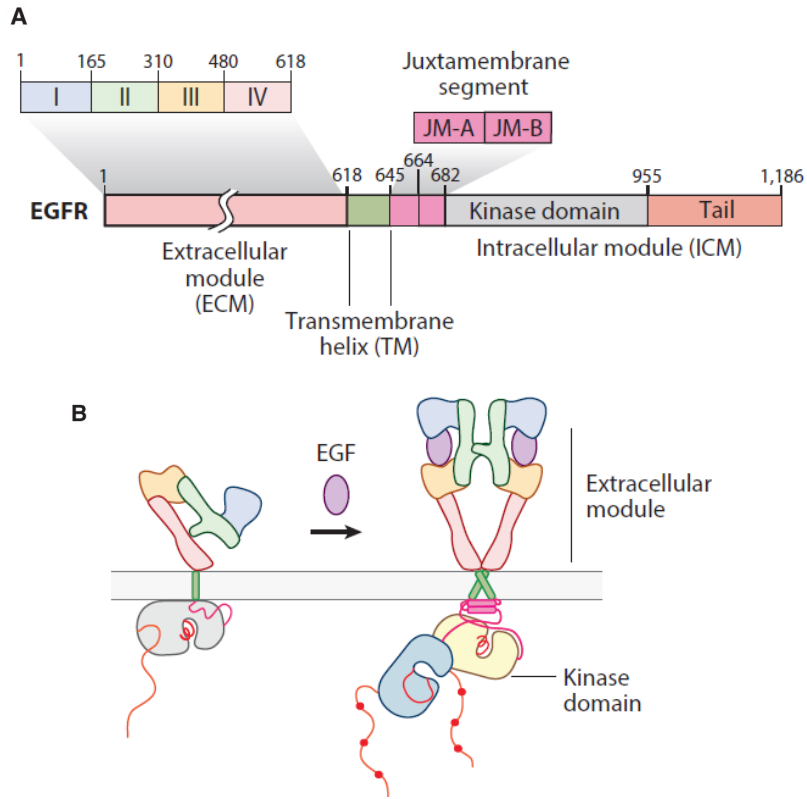
Figure 1.2. The epidermal growth factor receptor – structure, mechanism of activation, and intracellular signaling. (A) Schematic illustration of the domains of EGFR, including the extracellular domain (ECD), the transmembrane domain (TM), the juxtamembrane domain (JM), the kinase domain (KD), and the C-terminal tail (C-tail). (B) Schematic illustration of the growth-factor-induced EGFR activation upon EGF binding. Figure adapted from Ref. [79]

8
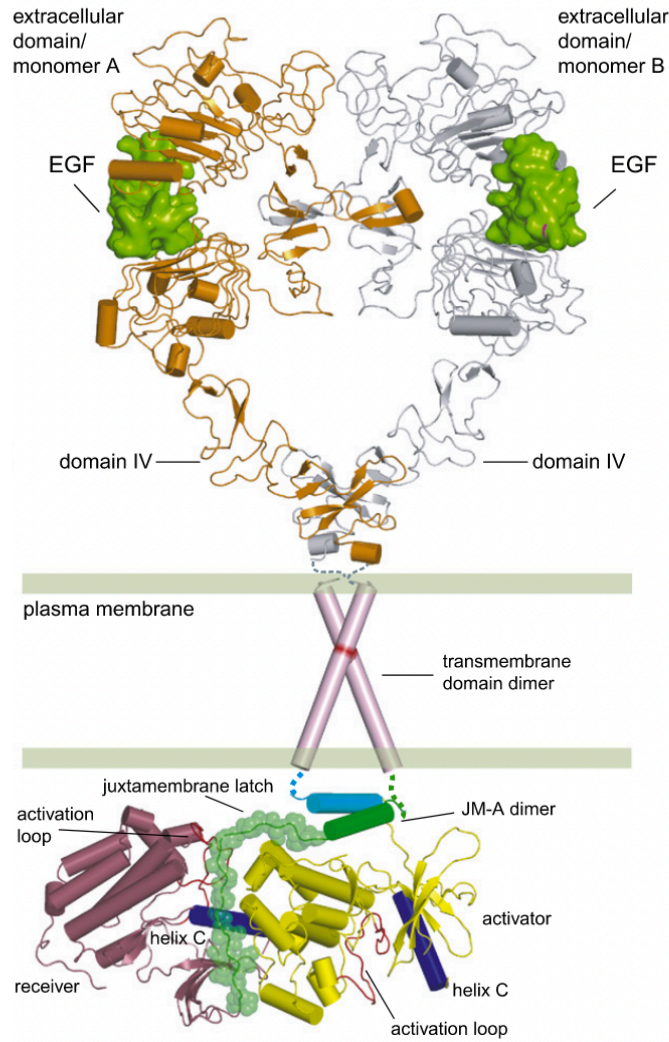
Figure 1.3. A model for the activated EGF receptor. Two EGF-bound EGF receptors in an active dimeric assembly. This model illustrated dimeric JM-A helices forming antiparallel coiled coil and JM-B latch around the 'receiver' kinase. Figure adapted from Ref. [23]
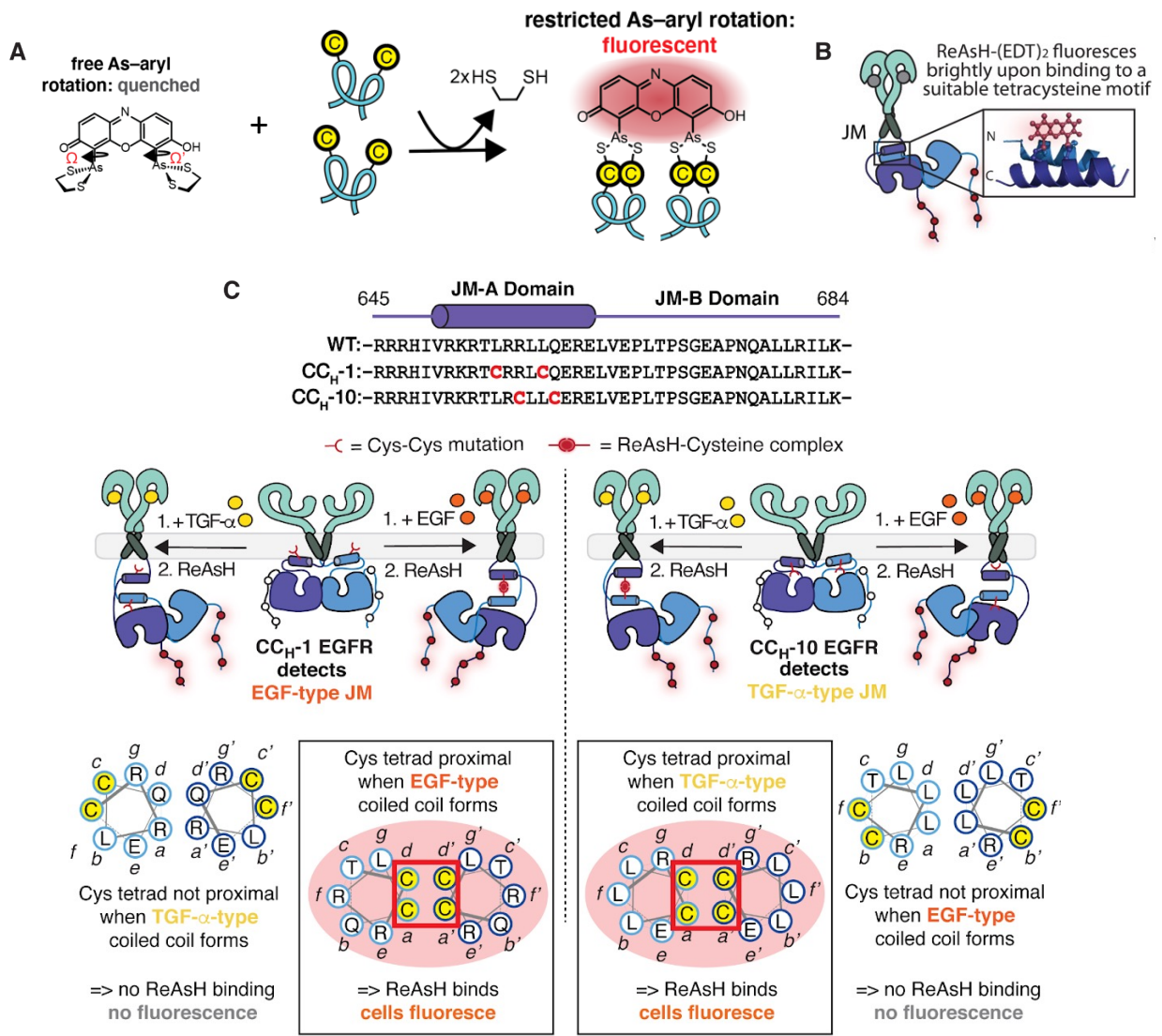
Figure 1.4. Using the chemical biology tool bipartite tetracysteine display to study protein domain conformation (A) The fluorescence sensor ReAsH dye is fluorogenic when it coordinates to the four proximate Cys side chains. (B) ReAsH binding to cysteine side chains of antiparallel α-helices to detect the presence of coiled coil conformation. (C) EGFR constructs CC$_H$-1 and CC$_H$-10 replacing residues in the JM-A that report either 'EGF-type' or 'TGF-α-type' coiled coils. The CC$_H$-1 construct has the Leu at the inter-helix interface replaced with four Cys. Thus, when a 'EGF-type coiled coil' forms, the proximal Cys replace the two ethanedithiol ligands from the ReAsH dye and result in an increased fluorescence signal. The CC$_H$-10 construct has the Gln and Arg polar residues at the inter-helix interface replaced with four Cys. Thus, when a 'TGF-α-type coiled coil' forms, the proximal Cys replace the two ethanedithiol ligands from the ReAsH dye and result in an increased fluorescence signal. Figure adapted from Ref. [80]

10
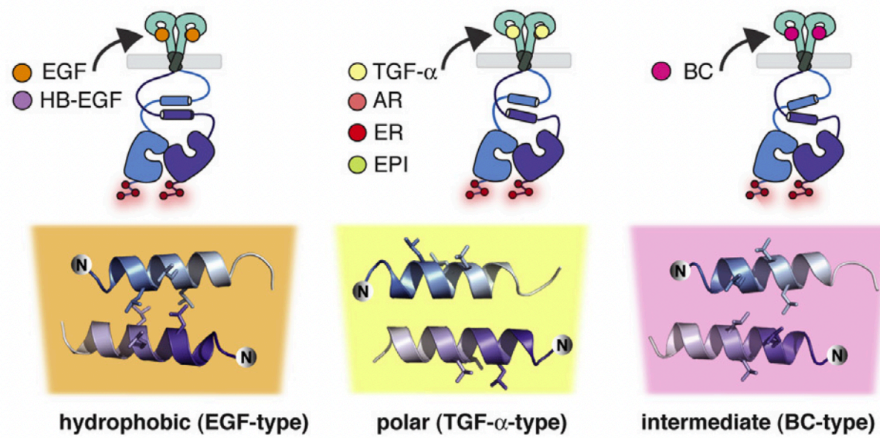
Figure 1.5. Growth factor identity is encoded in JM-A coiled coil conformation. EGFR exhibits three ligand-stimulated JM-A conformations. Activation by EGF and HB-EGF induces hydrophobic inter-helix interface 'EGF-type' coiled coil while TGF-α, AR, ER, and EPI activation induces polar inter-helix interface 'TGF-α-type' coiled coil. BC-activated EGFR adopts an intermediary conformation. Figure adapted from Ref. [37]
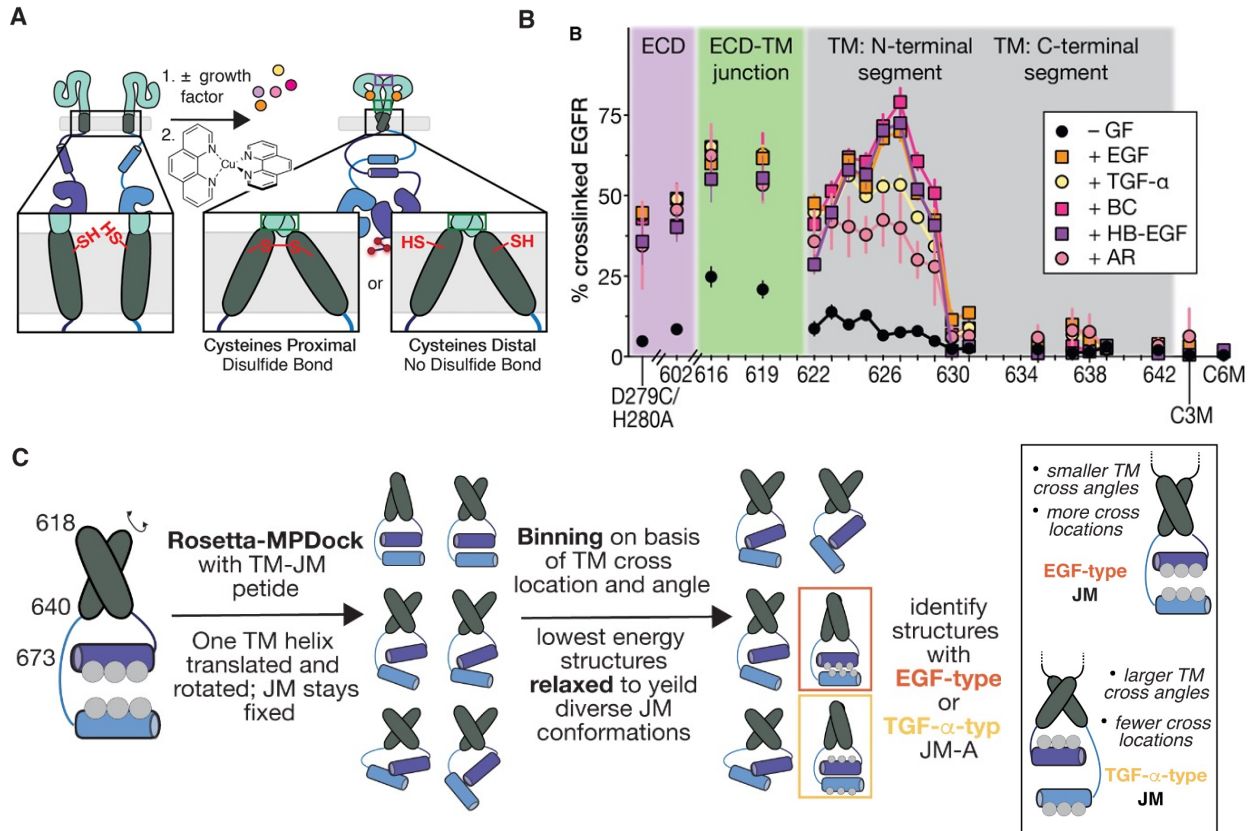
Figure 1.6. Inter-chain cross-linking experiments studying the growth factor dependency of TM dimer conformation. (A) Experimental scheme of cross-linking experiments with EGFR variants having proximal and distal Cys residues. Upon growth factor treatment, proximal Cys residues in TM dimer form disulfide bonds, while distal residues do not. (B) Plot illustrating the percent of cross-linked EGFR observed in cells expressing each Cys variant and treated with the indicated growth factor. The level of EGFR TM (particularly at residues 624–629) cross-linking was high when ECD bound EGF, HB-EGF, BC and low when bound TGF-α, AR. (C) Computational Modeling of the EGFR TM-JM segment with Rosetta-MPDock and MPrelax to model the EGFR TM-JM conformational landscape. The *in silico* study revealed that (i) larger TM cross-angles were associated with the formation of the TGF-α-type coiled coil within the JM, and (ii) differences in the TM helix dimer cross-location translate into different JM coiled coil conformation. Figure adapted from Ref. [55]
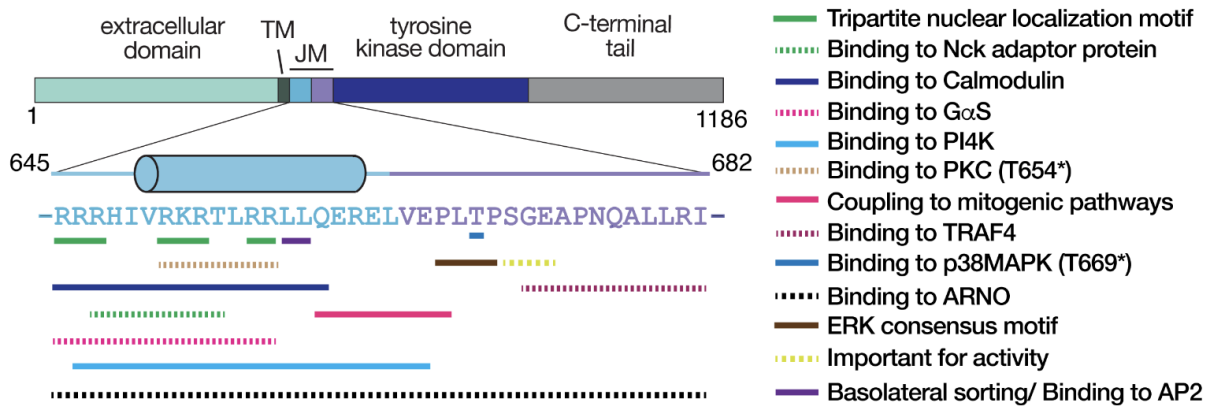
Figure 1.7. Sequence motifs and protein binding sites in the juxtamembrane region. Schematic illustration of the location and sequence of known cryptic motifs and protein binding sites in the juxtamembrane segment of EGFR. See also **Table 1.1.**

Table 1.1. Protein interactions with the juxtamembrane domain of EGFR

Protein interactor	Interaction region	Method / Construct	Effect / Exp summary	Ref
Calmodulin (CaM)	R645–Q660	Cross-linkage Assay / CaM and GST-JM (R645–Q660)	CaM binding is Ca^{2+}-dependent; pT654 inhibit binding (with T654D, and PKC treatment)	[59]
	R647, T654	SPR / CaM and immobilised GST-JM (M644–F688)		[58]
	R645-Q660	Radioactive probe conjugated JM (R645–Q660)	The presence of Ca^{2+}/CaM induced dissociation of JM from the PC/PS membrane	[62]
	R645-Q660	Fluorescence probe conjugated JM (R645–Q660)		[60]
	R645-Q660	FRET / EGFR TM-JM peptide (R645-Q660)	The presence of Ca^{2+}/CaM induced dissociation of JM from the POPC membrane containing PIP2	[29]
	R645-Q660	EGFR Activation Assay *in cellulo* with electrophoresis and immunoblotting	CaM antagonist treatment, CaM-KO in cells, chelation of Ca^{2+}, and mutagenesis CaM-binding domain inhibit EGFR activation	[61]
Nck adaptor protein	H648, I649, R647-T654	^{13}C-^1H HSQC of JM peptide (R645-672 and 644-674) titrated with unlabeled GB1-Nck1-2	The EGFR JM interacts with Nck adaptor protein	[63]
Stimulatory GTP binding protein (GaS)	R645-R657	IP and immunoblotting of GaS treated with EGFR JM peptides (R645-R657 and 679-692)	Phosphorylation of GaS	[64]
Phosphatidyl inositol-4-phosphate kinase (PI4P, or PIP)	R645-E657	IP and immunoblotting of treated with EGFR JM peptide (R645-R657)	Increased PI4P kinase activity	[65]
Protein kinase C (PKC)		A431 cells / ^{32}P labeling phosphorylation assay	PKC is related to the phosphorylation of the EGFR	[66,81]
	T654	A431 cells / ^{32}P labeling phosphorylation assay	Phosphorylation of T654 of the EGFR	[67,68]

	T654	A432 cells / B82 cells transfected with WT- and T654A-EGFR / I-125 EGF binding assay	Binding of EGF was lost for WT-EGFR upon PKC activation (by phorbol esters)	[82]
	T654	CHO cells transfected with WT- and T654E-EGFR / I-125 EGF binding assay	Binding of EGF was lost for WT-EGFR upon PKC activation; T654E-EGFR has lower tyrosine phosphorylation compared with WT-EGFR upon PKC activation	[69]
p38 MAPK	T669	A431 cells / ^{32}P labeling phosphorylation assay	Identified T669 phosphorylation in EGFR may mediate its changes in the binding and kinase state	[70]
	T669	MDA-MB-468 and CHO-K1 cells / WT- and T669A-EGFR constructs / Western blotting / ^{32}P labeling phosphorylation assay	Phosphorylation of T669 of the EGFR; T669 phosphorylation by cisplatin-induced p38 activation is essential for EGFR internalization	[71]
AP-2		NR6 cells / L679A and L680A-EGFR constructs / Internalization and recycling assay with I-125 EGF radioactivity measurements / Lamp-1 immunostaining and confocal microscopy	L679, L680 dileucine motif is critical for EGFR post-internalization endosomal sorting to late-endosome/lysosome degradation pathway	[72,73]
		PAE cells / L1010A, L1011A-EGFR constructs / ^{35}S-methionine-labeled EGFR degradation assay / I-125 EGF binding assay / Phosphorylation assay by immunoblotting	L1010, L1011 dileucine motif is critical for (a) EGFR degradation, (b) EGFR down-regulation, and (c) phosphorylation of beta-2 subunit of the clathrin adaptor complex AP-2	[83]
TRAF4	672-682	HeLa cells / 672-682 deleted EGFR / EGFR phosphorylation assay by immunoblotting / ^{15}N HSQC	TRAF4 is bind to the JM-B (672-682) of EGFR and is essential for EGF-induced activation	[74]
ARNO	EGFR-JM (645-682)	Microscale thermophoresis (MST) between EGFR-JM and Sec7 domain of ARNO / [^{1}H,^{15}N] HSQC EGFR-JM titrated with ARNO-Sec7	ARNO binds to the JM region competes with the binding interaction of the JM with CaM and anionic phospholipids	[75]

Protein kinase D (PKD)	T654, T669	CHO-K1 cells / T654- and T669-phospho-mimic mutants / Kinase-null PKD1 mutant (K612W) / eGFR-EGFR for Raster image correlation spectroscopy (RICS)	Phosphorylation of T654/T669 by PKD shifts the monomer-dimer equilibrium of EGF-bound EGFR towards the monomeric state; T654/T669 is PKD1 phosphorylation site; PKD1 activation is essential for EGFR monomerization; T654/T669 phosphorylation is crucial for monomerization	[84]

Chapter 2. Resolving high-resolution JM coiled coil conformation structure with JM-mimicking peptides

2.1. Abstract

As demonstrated in the literature review in chapter 1, the EGFR JM confirmation is an important allosteric switch in the EGFR activation and mechanism. Specifically, the two distinct coiled coil conformations—the 'EGF-type coiled coil' having the Leu residues at the inter-helix interface, and the 'TGF-α-type coiled coil' having the polar residues Gln and Arg at the inter-helix interface— and their role in encoding EGFR activation information. The role and the allosteric relationship between JM coiled coil and the ECD or the KD have been studied with bipartite tetracysteine display.[36,37,55] Although there have been reported NMR structures of the EGF-stimulated EGF-type coiled coil,[23,48] high-resolution JM conformation switching structures have yet to be reported. Inspired by previous designs[23] that mimic the JM domain dimer and building off previously discovered JM mutations that favor the formation of EGF-type and TGF-α-type coiled coil JM,[80] the studies described in this chapter focus on the JM-dimer-mimic peptides with these JM-switching mutations. The use of peptide mimics limits the molecule size for better molecular tumbling in structural characterization. The peptides were prepared with solid-phase peptide synthesis. The secondary structure and stability of the peptide were investigated with circular dichroism (CD). Solvent optimizations were evaluated with both CD and nuclear magnetic resonance (NMR) experiments.

2.2. Introduction

There are numerous powerful tools for the study of high-resolution protein structures. Cryogenic electron microscopy (cryo-EM) studies successfully resolved distinct ECM quaternary structures when bound to either EGF or TGF-α.[85] The cryo-EM experiments revealed the two states of ECD membrane-proximal tips and the difference in the ability of EGF and TGF-α to maintain conformation EGF and TGF-α differ in their ability to maintain the oncological-relevant conformation. Cryo-EM is a powerful tool in structural biology for solving complex biological structures.[86] It has several advantages over X-ray crystallography and NMR spectroscopy: requiring smaller amounts of sample and is less demanding on sample purity.[86] However, determining protein structure at atomic resolution remains challenging, especially for domains smaller than ~20 kDa.[87,88] Although there have been examples of α-helical structures resolved[89] and coiled coil structures studied[90] with cryo-EM, the resolution of the model at best reaches secondary structure topology (resolution > 6 Å). This might not be enough to resolve the subtle rotameric differences in the 'EGF-type' and 'TGF-α-type' coiled coil of JM. Besides cryo-EM, X-ray crystallography is a powerful tool for revealing high-resolution structures.[91–93] However, the concern over the technique is the effect of crystal packing on the protein structure. Dehydration reduces intermolecular packing spaces within the crystals, affecting atomic positions, and could lead to more compact side chains arrangement than the native, fully hydrated conditions.[94]

Nuclear magnetic resonance (NMR) is a technique with methods used for high-resolution protein structural studies under solution conditions. The JM antiparallel coiled coil conformation has been reported to exhibit the EGF-stimulated EGF-type coiled coil conformation using JM-dimer-mimicking peptide.[23] Following these footsteps, this study aimed to resolve the alternative JM structure of the EGF-type and the TGF-α-type coiled coil with established NMR methods.

2.2.1. Peptide mimicking JM dimer forms an antiparallel coiled coil

To investigate the JM structure, Jura and colleagues performed EGFR activity assays of alanine and glycine substitutions at the JM-A. Results suggested the LRRLL motif as the interaction site of the JM-A in the helical dimer.[23] From this, the initial model was built based on the coiled coil model reported by Woolfson and colleagues.[95] Taking the charge effect into consideration, Jura and colleagues deduced that parallel coiled coil conformation would be highly unlikely due to the close placement of several basic residues at the N-terminal ends of the two helices in a parallel coiled coil, making it energetically unfavorable. The finding that mutation R662E has little to no effect on EGFR activity also argued against the ion-paired parallel conformation (**Figure 2.1.A**) because the mutation is expected to destabilize the dimer (**Figure 2.1.B**). The more favorable antiparallel coiled coil conformation was supported and further resolved with NMR measurements on a 35-residue peptide. The peptide consists of two copies of the JM-A segment sequence attached by a 5-residue short flexible linker (**Figure 2.2**).[23] The peptide was synthesized so that the first and last Leu residues in the LRRLL motif and the second Glu in the first segment were labeled for NMR through-space Nuclear Overhauser Effect (NOE) experiments (L655 and L659 were labeled with ^{15}N, and E663 was labeled with ^{15}N and ^{13}C.). The NOE experimental data revealed the conformation of the JM-dimer-mimicking peptide assembled into an antiparallel coiled coil with specific antiparallel interaction. The first Leu of the LRRLL motif was at the *d* position of the helical wheel heptad and the second two Leu were at the *g* and *a* position (**Figure 2.1.C**).

2.2.2. JM-switching mutations at the JM

Jura and colleagues used a JM-dimer-mimicking peptide and NOE experiments to resolve the EGF-type coiled coil (**Figure 2.1.C**). To probe the variability of the JM conformation between the EGF-type and TGF-α-type coiled coil, mutagenesis that alters the JM conformation was investigated by members of the Schepartz group. Studies done by Mozumdar and colleagues identified EGFR variants with mutations in the JM[80] that decouples the well-established relationship between JM coiled coil status and growth factor identity.[37,55,96] In the helical wheel projections of a coiled coil structure, the *e* and *g* positions can form salt bridges that influence coiled coil stability and orientation.[97] On the other hand, changes at the *a* and *d* positions influence the oligomeric state (**Figure 2.3**).[98] Mozumdar and colleagues hypothesized that the relative stability of the EGF-type and TGF-α-type coiled coils in wild-type EGFR dimer was influenced by the salt bridge interactions. Predictably, the presence or absence of coiled coil-specific salt-bridging residues at positions *e* and *g* can be used to control the coiled coil conformation. The removal of one or more interactions that stabilized one JM coiled coil would raise its free energy relative to the other and shift the equilibrium between the two structures. The variants identified will bias towards one or the other coiled coil, resulting in the decoupling of coiled coil conformation and growth factor identity.

The identified EGFR variants are E661R and K652A/R656A (variant labeled KRAA) amino acid substitutions selectively disrupt salt bridges unique to either the TGF-α- or EGF-type JM coiled coils (**Figure 2.3.A**). The Glu to Arg mutation in E661R was located at distal *c* and *c'* positions when the JM dimer conformation exhibits an EGF-type coiled coil but was located at proximal *e* and *e'* positions in TGF-α-type coiled coil. As a result, the JM in E661R would favor the EGF-type coiled coil structure because the Glu to Arg charge-reversing mutation of E661R disrupts the salt bridge

for the stabilizing effect in the TGF-α-type coiled coil (**Figure 2.3.B**). In the case of K652A/R656A EGFR (KRAA), the four Ala residues were located at distal *c,g* and *c',g'* positions in TGF-α-type coiled coil but at proximal *e,a* and *e',a'* positions in EGF-type coiled coil. Thus, the JM in KRAA would therefore favor the formation of TGF-α-type coiled coil for the same reason of salt bridge disruption (**Figure 2.3.B**). The JM coiled coil conformations of E661R and KRAA were validated using the bipartite tetracysteine display method to show that the E661R and KRAA mutation biased the JM coiled coil to form either EGF-type or TGF-α-type coiled coil *in cellulo*.[80]

2.3. Results

2.3.1. Solid-state peptide synthesis, peptide purification, and peptide characterization

Peptides were made adapting the reported JM-dimer-mimicking design and applying the E661R and KRAA mutations to bias the JM coiled coil structure into favoring the formation of either the EGF-type or TGF-α-type. The peptides of interest were listed in **Table 2.1**. The original JM-dimer-mimicking peptide was a 35-residue peptide consisting of two identical 15-residue JM-A sequences (K_{652}RTLRRLLQERELVE$_{666}$) flanking a short 5-residue glycine-serine linker (N-K_{652}RTLRRLLQERELVE$_{666}$-GSGSG-K_{652}RTLRRLLQERELVE$_{666}$-C).[99] It was coined the Jura_35 peptide. The EGF-type-coiled-coil-favoring mutation E661R and the TGF-α-type-coiled-coil-favoring mutation KRAA led to the design of E661R_35 and KRAA_35 peptides (**Table 2.1**). The two mutations in E661R_35 increased the charge of the peptide from +4 to +8 in the reported sodium acetate buffer of pH 5.1. However, the four mutations to Ala in KRAA_35 resulted in a neutral peptide hence poor solubility in aqueous solutions. To increase peptide solubility, the first segment in the peptide design expended at the N-terminal to include six more residues from the TM domain to obtain an overall +4 charge at pH 5.1. The new peptide was coined the KRAA_41 indicating the amino acid number as 41 (**Table 2.1**). KRAA_42 with an additional Tyr residue at the N-terminal of KRAA_41 for concentration determination with UV absorbance at 280 nm was also synthesized and purified. The peptides of interest were synthesized using a semi-automatic solid-phase peptide synthesis (SPPS) instrument, cleaved from the solid-support resin, lyophilized, and purified using reversed-phase high-performance liquid chromatography (RP-HPLC). The purified fractions were characterized by liquid chromatography-mass spectrometry (LC-MS) and analytical ultra high performance liquid chromatography (UPLC) (**Figure 2.4**). The RF-HPLC-purified E661R_35 fraction contained two species with very similar retention times (**Figure 2.4.B**). Since the E661R_35 is expected to form the EGF-type coiled coil, which the structure has already been reported.[23] The subsequent characterization will focus on the TGF-α-type-coiled-coil-favoring KRAA_41 and KRAA_42 variants.

2.3.2. The JM-dimer-mimicking peptides exhibit stable α-helical structure with the addition of cosolvent or detergent

Circular dichroism (CD) is a common tool to confirm the secondary structures of peptides and proteins.[100–102] The JM-dimer-mimicking tandem peptides were expected to exhibit two α-helices to form the coiled-coil structure. CD experiments were done to also monitor the stability of the peptides. It is helpful to confirm that the α-helical structures were maintained in the peptides for hours in the buffer condition, which is the time required for the collection of 2D NMR experiments. However, it is hard to unambiguously distinguish between random coil and α-helix

from the CD spectra since the sodium acetate buffer gives rise to large noise in the wavelength region below 200 nm that masks the characteristic CD signals of α-helix. The addition of cosolvent trifluoroethanol (TFE) was shown to promote the helical secondary structure of unstructured peptides in an aqueous buffer by providing a more hydrophobic environment.[103–105] The presence of TFE promoted the α-helical secondary structure of the Jura_35 (**Figure 2.5**). However, the addition of TFE resulted in the precipitation of peptides KRAA_41 and KRAA_42. To address this, an alternative secondary structure stabilizing additive was explored. Detergent sodium dodecyl sulfate (SDS) has been shown to promote α-helix in the prion protein.[106] The presence of SDS in solutions containing the KRAA_42 resulted in the stabilization of the α-helical secondary structure for up to 22 hrs (**Figure 2.6**).

2.3.3. Investigating concentration-dependent oligomerization of the JM-dimer-mimicking peptides

One of the ways to investigate the oligomeric state of coiled coil structure is with concentration effect experiments. The hypothesis is that if α-helical structures of the peptide are stabilized by intermolecular coiled coil interactions, the normalized CD signal will increase in intensity with increasing peptide concentration that favors the formation of multimers. In contrast, intramolecular coiled coil stabilization of α-helical results in concentration-independent CD spectra. Results showed no concentration dependence of α-helical secondary structure in KRAA_42 within the concentration range of 50–200 µM (**Figure 2.7**). Comparatively, Jura and colleagues studied the concentration-dependent line broadening of TOCSY signals of Leu methyl and Val methyl of Jura_35 peptide at 200 µM, 0.5 mM, and 2 mM under identical conditions. Concentration-dependent line broadening of the methyl groups indicates the presence of oligomer populations. Concentration-dependent line broadening was observed by Jura and colleagues when the peptide concentration increased from 0.5 mM to 2 mM.[23] This was consistent with our finding with the CD experiments that there was no concentration dependence of α-helical secondary structure in JM-dimer-mimicking peptides of 50–200 µM.

2.3.4. The folding of JM-dimer-mimicking peptide is transient

^{1}H 1D NMR of KRAA_42 was performed to examine the homogeneity of the chemical environment in the peptide ensemble (**Figure 2.8**). The experiment was first performed with 100 µM KRAA_42 in acetate buffer containing SDS (50 mM acetate-d4, pH 5.1,[23] 8 mM SDS). The signal quality was weak (**Figure 2.8.A**). Thus, cosolvent dimethyl sulfoxide (DMSO) was introduced to the buffer as it was reported to perturb protein structure and partially stabilize folded conformations.[106] The signal improved upon introducing 5% DMSO in the acetate buffer (**Figure 2.8.B**). However, the bulk of the signal at the amide proton chemical shift region in acetate buffer exhibited a resolution close to 1.0 ppm, which is not a good sign for 2D NMR experiments (**Figure 2.8.B**). Poor resolution in 1D experiments and signal broadening were results of sample inhomogeneity. Sample inhomogeneity does not just yield 2D NMR spectra that are hard to perform peak assignment, but also implies that there exhibit populations of multiple conformations with nanoscopic differences, hindering high-resolution structural studies. Buffer conditions excluding SDS and adding 5% DMSO (**Figure 2.9.A**) or 5% Acetonitrile (MeCN, ACN) (**Figure 2.9.B**) were tested and the signals under these conditions were improved. However, the

improvement was not significant enough to resolve all 42 amide-protein signals (one for each residue in KRAA_42) for confident 2D NMR experiments and assignments. KRAA_42 precipitation was observed several hours after dissolved in the prepared sample buffer. Although the CD experiment demonstrated a stable α-helical secondary structure of KRAA_42 with acetate buffer containing SDS, nanoscopic level homogeneity and overall stability of the peptide are still required. **Table 2.2** listed solvent conditions tested for KRAA_42 stability with either acetate buffer or phosphate buffer; pH 5.5, 7.1, or 7.6; the presence of cosolvent DMSO, MeCN, or acetone. KRAA_42 was partially soluble in the conditions listed in **Table 2.2**. This suggests a drastically different solution condition from the reported pH 5.1 acetate buffer for Jura_35[23] is essential for the structural study of peptide KRAA_42.

To investigate the folding of JM-dimer-mimicking peptide, nuclear Overhauser effect spectroscopy (NOESY) combined with heteronuclear single quantum coherence (HSQC) NMR experiments were performed. NOESY methods reveal the spatial relationship between isotopically labeled nuclei.[107] HSQC transduces signals from ^{1}H to heteronuclear such as ^{13}C and ^{15}N in the backbone or the side-chain. I synthesized and purified Jura_35 (**Figure 2.10.B**) following the same labeling scheme as Jura and colleagues (L655 and L659 were labeled with ^{15}N. E663 was labeled with ^{15}N and ^{13}C.).[23] ^{15}N-^{1}H NOESY–HSQC experiments were done on 200 µM Jura_35 in 50 mM sodium acetate buffer of pH 5.1. The ^{15}N-labeled L655, L659, E663 were assigned by ^{15}N chemical shifts (**Figure 2.10.B**). The ^{15}N-^{1}H NOESY–HSQC spectra was compared with the results produced by Jura and colleagues (**Figure 2.10**). Jura and colleagues observed correlations between intra-segment through-space coupling within segment A and inter-segment through-space coupling between segment A and segment B (**Figure 2.2**). The intra-segment coupling includes interaction between L655 amide proton and L665 H_β, L655 amide proton and L655 H_γ, L655 amide proton and T654 H_γ, and L629 amide proton and L629 H_β. The inter-segment coupling includes interaction between segment A L659 amide proton and segment B L655 H_δ (**Figure 2.10.A**). These interactions were consistent with the model Jura and colleagues proposed of the EGF-type JM antiparallel coiled coil (**Figure 2.1.D**). However, the Inter-segment coupling interaction between segment A L659 amide proton and segment B L655 H_δ was not observed in my data, nor was the intra-segment coupling interaction between L655 amide proton and T654 H_γ (**Figure 2.10.B**). The absence of through-space coupling interaction gave rise to the question of whether peptides under the solvent condition fold into coiled coil conformation properly.

Jura and colleagues suggested that the JM-A peptide exhibit transient rather than stable adoption of helical structure in both segments A and B under the conditions of the NMR experiment.[23] Jura and colleagues determined the secondary structure of the 15-amino-acid JM-A peptide with sequential NOE connectivities. Residues involved in an α-helix typically show characteristic NOE cross-peaks including $H_N H_N$(i, i+1), $H_N H_N$(i, i+2), $H_\alpha H_N$(i, i+3), $H_\alpha H_N$(i, i+4), and $H_\alpha H_\beta$(i, i+3).[108–110] However, data presented by Jura and colleagues only demonstrated NOE $H_N H_N$(i, i+1) cross-peaks between nine residues L658-E666 in the 15-amino-acid JM-A, and only four NOE $H_\alpha H_N$(i, i+3) cross-peaks between Q660-E663. The NOE connectivities indicated that the helical structure in JM-A peptides is transient rather than stable. Jura and colleagues performed molecular dynamics of the JM-A helical dimer docking simulation with the KD to show that the intramolecular and intermolecular ion pairs were broken and reformed due to transient interactions with water and ions. Endres and colleagues also used a program based on empirical relationships between backbone chemical shifts and backbone dihedral angles to predict that the JM-A helix only has a

30% probability of helical formation.[48] Taken together, the results suggested that the formation of an antiparallel helical dimer for the isolated peptide is transient in solution but expected to be α–helical in the intact protein.[23,110]

2.4. Conclusion

The EGFR JM confirmation was studied with bipartite tetracysteine display[36,37,55] to show its allosteric relationship to ECD and TM in EGFR activation. However, the high-resolution JM conformation switching between the EGF-type and TGF-α-type coiled coil structures has yet to be reported. Combining previously reported designs of peptides mimic the JM domain dimer[23] and JM mutations that favor the formation of EGF-type and TGF-α-type coiled coil JM,[80] Jura_35, E661R_35, and KRAA_42 were prepared to bias the JM coiled coil to form either EGF-type or TGF-α-type coiled coil (**Table 2.1**). Circular dichroism experiments of Jura_35 and KRAA_42 showed that these JM-dimer-mimicking peptides exhibit stable α-helical structures with the addition of cosolvent or detergent. The presence of cosolvent trifluoroethanol (TFE) promoted the helical secondary structure of the Jura_35, while detergent sodium dodecyl sulfate (SDS) addition in solutions containing the KRAA_42 resulted in the stabilization of the α-helical secondary structure. The CD experiments revealed no concentration dependence of α-helical secondary structure in KRAA_42 of 50–200 µM, excluded the possibility of multimer formation in this concentration range. Although the CD experiments demonstrated a stable α-helical secondary structure of KRAA_42 with acetate buffer containing SDS, peptide precipitation was observed several hours after the dissolution in the sample buffer. The ^{1}H 1D NMR results of KRAA_42 under various buffer conditions were not able to fully resolve all the amide proton signals for a convincing 2D NMR analysis (**Figure 2.7** and **Figure 2.8**). The nanoscopic folding state of the isolated peptide was examined with NOE experiments. In our data, through-space coupling interaction between the replicated segment in the JM-dimer-mimicking peptide was absent. This was consistent with the previously proposed conclusion that the folding of the JM-dimer-mimicking peptide is transient.[23] The stabilization effect of SDS on KRAA_42 α-helical secondary structure suggested that KRAA_42 peptide was stabilized by an amphiphilic environment slightly resembling a plasma membrane containing phospholipids. Jura and colleagues concluded that proper antiparallel coiled coil folding of the peptide is expected when interactions with the kinase domain (KD) were observed. Arkhipov and colleagues used molecular dynamics simulations to suggest that the flexibility of JM-A may be due to the absence of negatively charged lipids or the KD. These observations suggested that structural studies of the JM domain require stabilization of the molecule ensemble with more interactions either with other EGFR subdomains or with the plasma membrane.

2.5. Methods and Materials

Materials. Dimethyl sulfoxide (DMSO) and acetone were the products of Sigma-Aldrich. Acetonitrile was the product of Fisher Scientific. Sodium dodecyl-d25 sulfate (SDS-d25) and acetic acetate-d4 were the products of Cambridge Isotope Laboratory.

Solid-phase peptide synthesis. The peptides of interest were prepared with solid-phase peptide synthesis with the Biotage® Initiator+ Alstra automated single-channel microwave peptide synthesizer. H-Rink amide ChemMatrix resin was used as the solid support. The synthesis scale

was 50 μmol. SPPS utilizes an orthogonal protection scheme. The base-labile fluorenylmethyloxycarbonyl (Fmoc) protecting group of the α-amine was removed during deprotection reaction mixing in 20% piperidine (Sigma-Aldrich) in N, N-Dimethylformamide (DMF, Fisher Scientific) at room temperature for 5 min. The Fmoc-protected amino acid were products of Novabiochem except for ^{15}N-Leu-Fmoc and ^{13}C, ^{15}N-Glu-Fmoc. ^{15}N-Leu-Fmoc and ^{13}C, ^{15}N-Glu-Fmoc were products of Cambridge Isotope Laboratory. The coupling reagents were Hydroxybenzotriazole (HOBt, Sigma-Aldrich), (2-(1*H*-benzotriazol-1-yl)-1,1,3,3-tetramethyluronium hexafluorophosphate (HBTU, Sigma-Aldrich), and N,N-Diisopropylethylamine (DIPEA, Spectrum Chemical). The coupling mixture wad consisted of Fmoc-protected amino acid, HOBt, HBTU, and DIPEA with the ratio 1:1:0.98:2. The coupling mixture reacted with the elongating peptide by mixing at 75 °C for 5 min. The coupling condition for Arg residues was twice at 75 °C for 5 min. His residues were coupled twice at 50 °C for 5 min to avoid racemization at high temperatures. ^{15}N-Leu and ^{13}C, ^{15}N-Glu were coupled at 50 °C for 15 min. The resulting resin-bound peptide was mixed with an acidic cleavage cocktail at room temperature for 4 hrs to cleave the acid-labile side chain protecting group and acid-labile resin linker. The cleavage cocktail was consisted of 92.5% trifluoroacetic acid (TFA, Sigma-Aldrich), 2.5% 1,2-ethanedithiol (EDT, Sigma-Aldrich), 2.5% triisopropylsilane (TIPS, Sigma-Aldrich), and 2.5% deionized water (Millipore Milli-Q lab water system). The cleaved peptide was then precipitated in ice-cold diethyl ether. The precipitated peptides were dissolved in 15% (v/v) acetonitrile and dried with a freeze-dryer (Labconco, FreeZone 4.5 plus).

High-performance liquid chromatography. Freeze-dried peptides were dissolved in 15% (v/v) acetonitrile and were purified with reverse-phase high-performance liquid chromatography (RP-HPLC, Agilent 1260 Infinity II LC System) using C8 reverse-phase HPLC column (Vydac 208TP C8, Avantor). The solvents used were Milli-Q deionized water with 0.1% TFA and acetonitrile with 0.1% TFA. The purification gradient was 30–40% B over 20 mins at a flow rate of 4 mL/min. The fraction was detected with a UV detector at 214 nm and 280 nm.

Ultra high performance liquid chromatography. The purity of HPLC purified fractions was analyzed with reverse-phase ultra high performance liquid chromatography (UPLC, UHPLC, Shimadzu, Prominence HPLC) using a C18 analytical column (Agilent Poroshell 120 SB-C18 2.7 um). The solvents used were Milli-Q deionized water with 0.1% TFA and acetonitrile with 0.1% TFA. The gradient was 20–60% B over 10 mins at a flow rate of 0.5 mL/min and pressured at ~2100 psi. The fraction was detected with a UV detector at 214 nm and 280 nm.

Liquid chromatography–mass spectrometry. The mass of HPLC purified fractions were analyzed using Waters ACQUITY LC-MS System with C18 Waters analytical column.

Circular dichroism. CD data were collected using a cell of 2-mm path length (Starna Spectrophotometer Cells). Each reported CD value was the mean of three measurements. Data was expressed in terms of molar ellipticity converted from miliDegrees (mDeg) to molar ellipticity (M.E.) by the following relationship:

$$\mathrm{M.\,E.\,(Deg \times cm^2 \times dmol^{-1})} = \frac{\mathrm{mDeg}}{10 \times l\,(\mathrm{cm}) \times \mathrm{M}(\frac{\mathrm{mol}}{\mathrm{L}})}$$

CD spectra were recorded at 20 °C using Applied Photophysics, Chirascan spectrometer. The scan rate was 1 nm/s from 190 to 220 nm.

Nuclear magnetic resonance experiments. *^{1}H 1D NMR experiments* were performed on Bruker 900 MHz spectrometer at 303 K (30 °C) with peptides in 50 mM deuterated acetate buffer pH 5.1

and 10% D_2O with additives specified in texts and figure captions. The ^1H frequency was set to the water resonance. A constant relaxation delay period of 1 s was used. NMR spectra were processed by the Bruker TopSpin software. *^{15}N-^1H NOESY–HSQC experiments* were performed on a Varian Inova 600 MHz spectrometer equipped with triple-resonance probes and a cryoprobe. Experiments were performed at 293 K (20 °C). The ^1H and ^{15}N frequencies were set to the water resonance and 124.5 ppm. A constant relaxation delay period of 1 s was used. The NOESY mixing time was set at 300 ms. 2044 x 32 x 16 numbers of points were in the direct ^1H, indirect ^1H, and indirect ^{15}N detected dimensions. The spectral widths were 12019.2 Hz, 10396.1 Hz, and 600 Hz for the direct ^1H, indirect ^1H, and indirect ^{15}N. NMR spectra were processed with NMRPipe and analyzed in SPARKY. The cross-peaks were assigned by the ^{15}N chemical shift assignment.

A parallel dimer Leu 655 at position *a* / parallel dimer Leu 655 at position *d*

B kinase-facing side / membrane-facing side

C

D antiparallel dimer (Leu 655 at '*d*') / antiparallel dimer (Leu 655 at '*a*') / parallel dimer

- ● atoms labeled with ^{15}N and/or ^{13}C for NMR
- ● alpha carbons
- ○○○ no close contact (consistent with NOESY)
- ●●● close contact (consistent with NOESY)
- ○○○ no close contact (inconsistent with NOESY)
- ●●● close contact (inconsistent with NOESY)

25

Figure 2.1. α-helical dimer in the JM-A segment (A) The modeled parallel JM-A dimers of two scenarios: L655 placed in *a* position or *d* position. The rotated views show ion pair interactions involving R662 with either E661 or E663. (B) The modeled antiparallel JM-A helical dimer, with L655 at the *d* position. The kinase-facing side shows the ion pair interaction between R656 and E663. (C) Effect of mutations of the residues involved in the ion pairs in the models of the parallel JM-A dimer (R662) and the antiparallel JM-A dimer (R656). The effect of EGFR activity was examined with Y1173 phosphorylation immunoblotting. (D) The models for JM-A helical dimer: antiparallel with L655 at the *d* position (left), antiparallel with L655 at the *a* positions(middle), and parallel with L655 at the *d* position (right). The dotted lines indicate inter-atomic contacts consistent or inconsistent with NOESY measurements for the JM-dimer-mimicking peptide. Figure adapted from Ref. [23]

K$_{652}$RTL$_{655}$RRLL$_{659}$QERELVE$_{666}$GSGSGK$_{652}$RTLRRLL$_{659}$QERELVE$_{666}$

Segment A	Segment B

Figure 2.2. The design of the JM-dimer-mimicking peptide Jura_35. 35-residue peptide consists of two copies of the JM-A segment sequence, designated segment A and segment B, attached by a 5-residue short flexible linker to favor the formation of an antiparallel coiled coil. A list of all the peptides of interest is listed in **Table 2.1**.
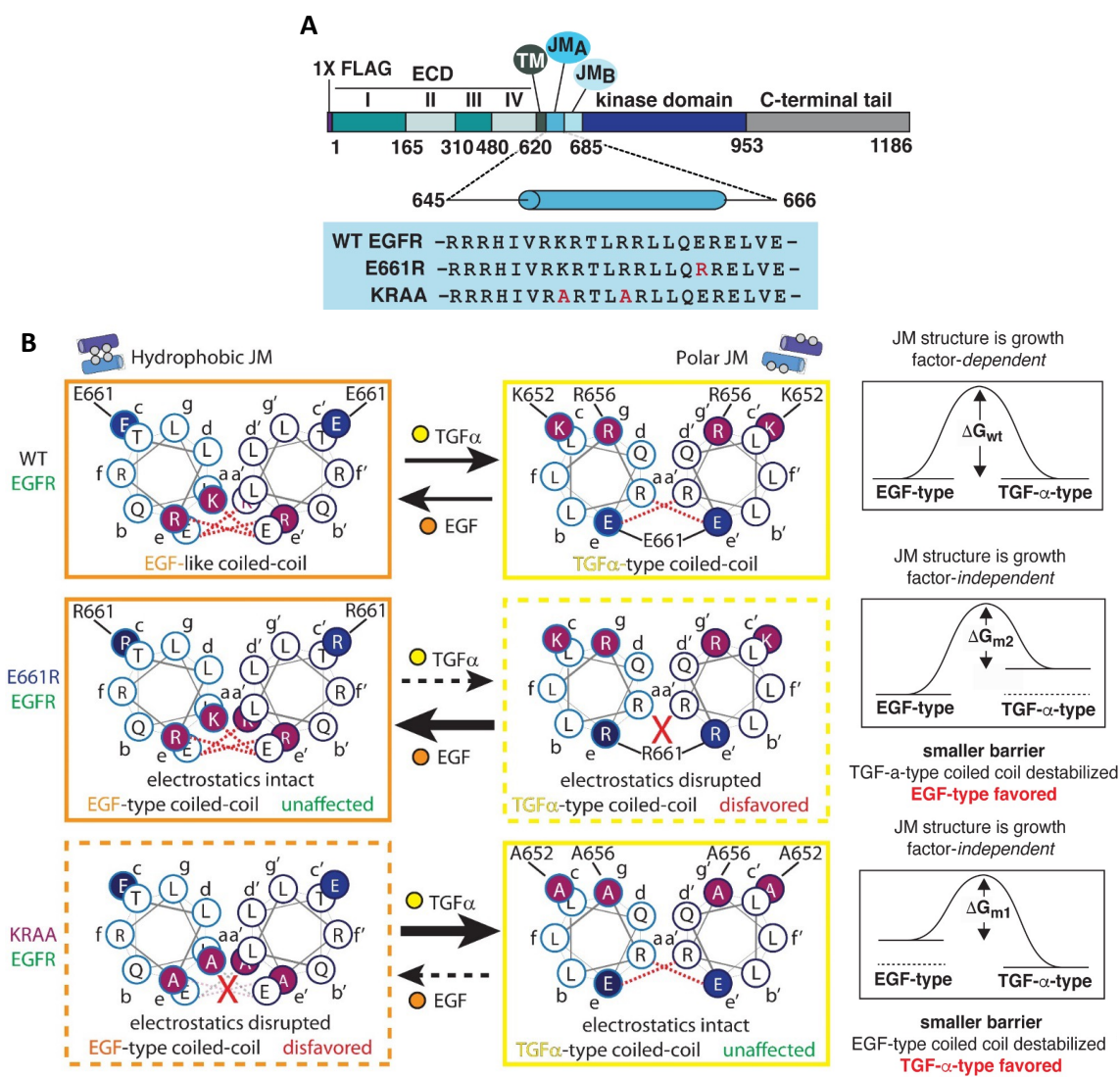
Figure 2.3. The design of EGFR decoupling JM-switching mutations. (A) Domain diagram of FLAG-tagged EGFR illustrating sequences of WT EGFR, E661R, and KRAA. (B) The hypothesis of the conformation-favoring effect of the JM mutants. In WT EGFR, both coiled coil conformations are energetically accessible, and the identity of the bound growth factor identity was coupled with the JM coiled coil conformation. In the E661R variant, the Glu to Arg mutation disrupts the salt bridge for the stabilizing effect in the TGF-α-type coiled coil, favoring the EGF-type coiled coil. In the KRAA variant, the four Ala mutation disrupts the salt bridge in the EGF-type coiled coil, destabilizing the EGF-type conformation state, and favoring the formation of the TGF-α-type coiled coil. Figure adapted from Ref. [78]
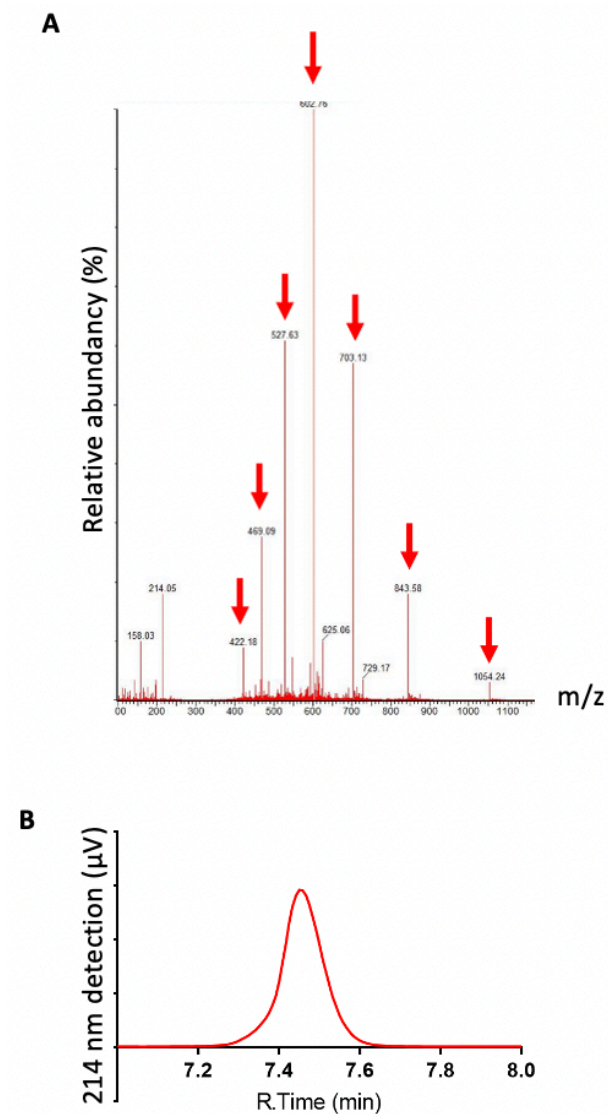
Figure 2.4. Characterization of HPLC purified Jura_35. (A) LC-MS analysis of Jura_35 in a positive ion mode. The arrows indicated MS intensities of multi-charged species $[M-nH]^{n+}$. The theoretic molecular weight of Jura_35 is 4212.872. The deconvoluted molecular weight from multi-charged species was 4212.8. (B) The UPLC analysis of Jura_35 showed a single species with 214 nm detection on a C18 reverse-phase column.
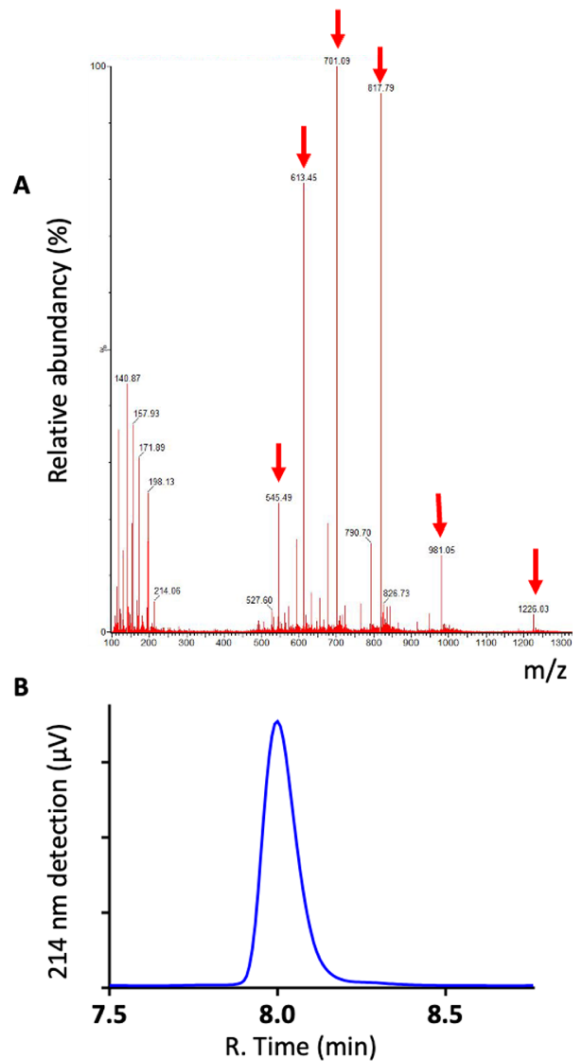
Figure 2.5. Characterization of HPLC purified KRAA_42. (A) LC-MS analysis of KRAA_42 in a positive ion mode. The arrows indicated MS intensities of multi-charged species $[M-nH]^{n+}$. The theoretic molecular weight of KRAA_42 is 4901.6343. The deconvoluted molecular weight from multi-charged species was 4900.3. (B) The UPLC analysis of KRAA_42 showed a single species with 214 nm detection on a C18 reverse-phase column.
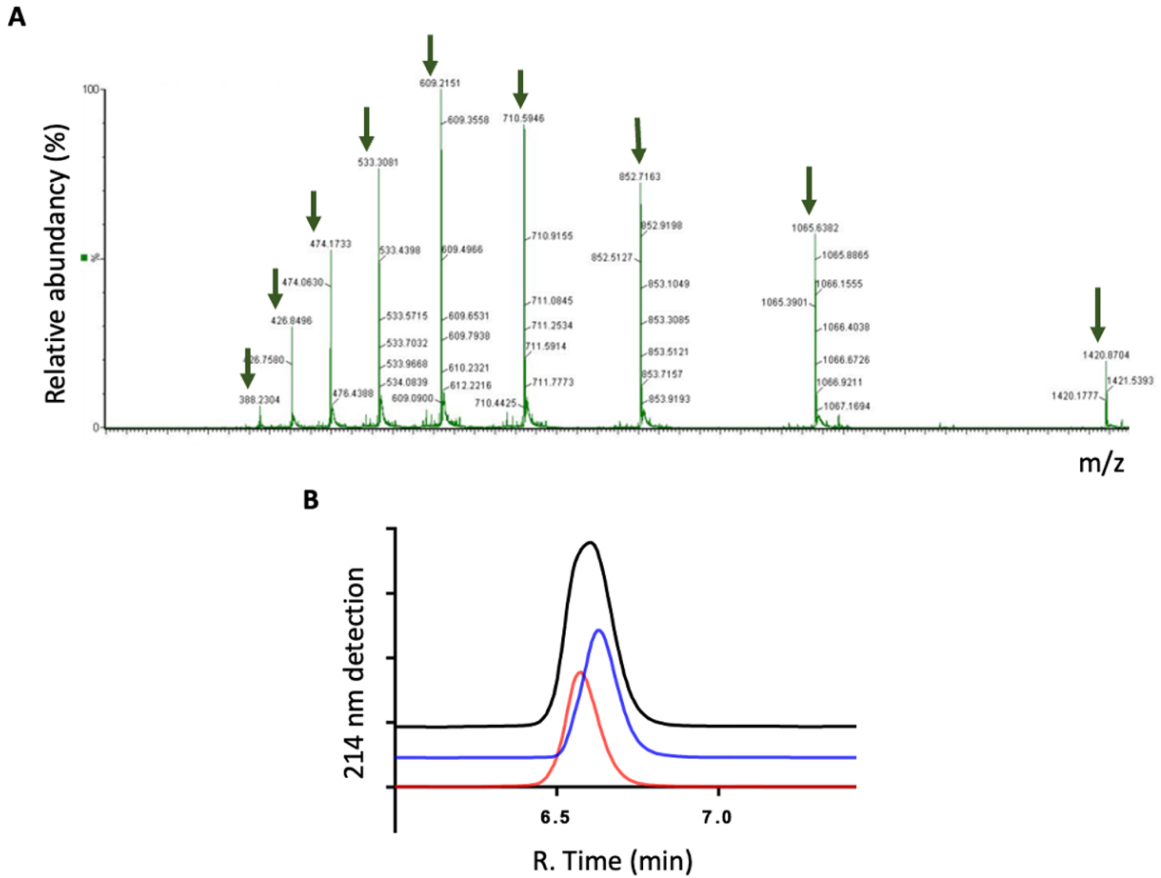
Figure 2.6. Characterization of HPLC purified E661R_35. (A) LC-MS analysis of E661R_35 in a positive ion mode. The arrows indicated MS intensities of multi-charged species $[M-nH]^{n+}$. The theoretic molecular weight of E661R_35 is 4259.016. The deconvoluted molecular weight from multi-charged species was 4258.5. (B) The UPLC analysis of E661R_35 shows a broad peak with a shoulder peak. Further purification revealed a modest difference in C18 reverse-phase column retention time. The top two UPLC elution profiles were offset for clarity.
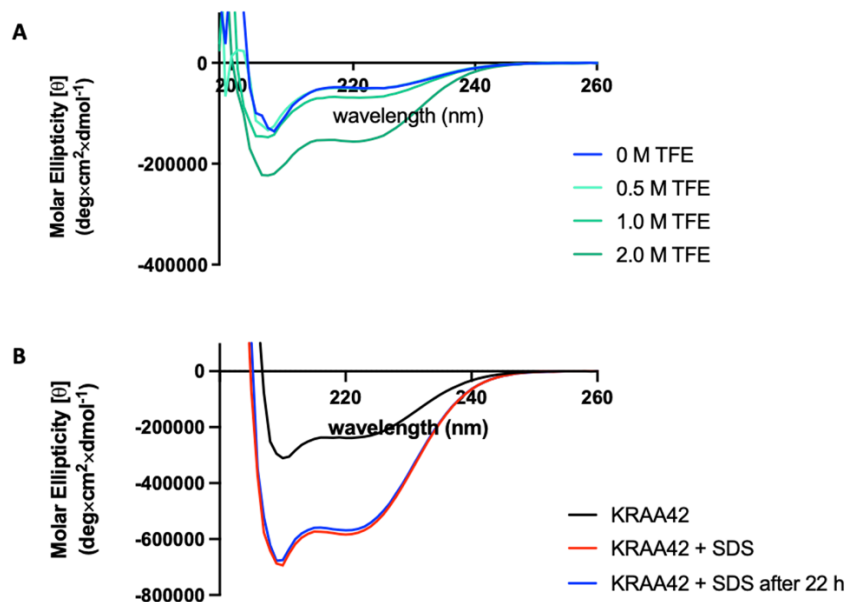
Figure 2.7. α-helical secondary structure of the JM-dimer-mimicking peptides is promoted with the addition of cosolvent or detergent. (A) CD spectra of Jura_35 peptide of 500 µM with 0.0, 0.5, 1.0, and 2.0 M of trifluoroethanol (TFE). The presence of TFE enhanced the intensity of the characteristic signal for α-helical secondary structure at 208 and 222 nm. (B) CD spectra of KRAA_42 peptide of 120 µM in the presence (3.0 mM) or absence of sodium dodecyl sulfate (SDS). The presence of SDS enhanced the intensity of the characteristic signal for α-helical secondary structure at 208 and 222 nm. The α-helical secondary structure enhancement with SDS was observed 22 hrs after addition. CD spectra were expressed in molar ellipticity.
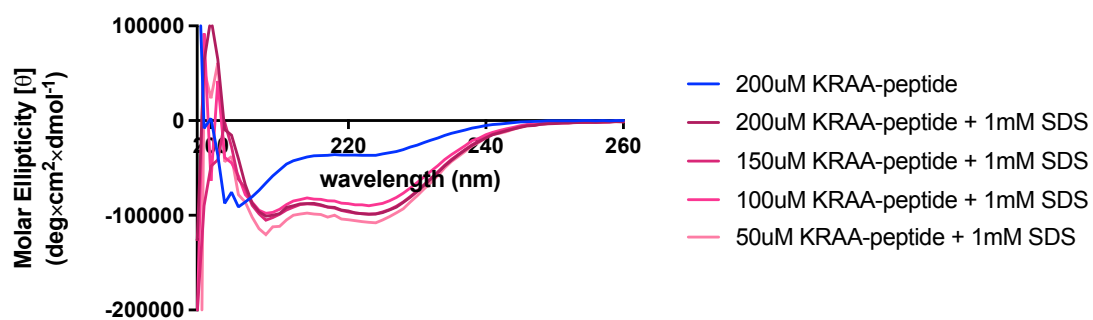
Figure 2.8. No concentration dependence of the KRAA_42 α-helical secondary structure was observed. No significant changes in intensity of the characteristic α-helical CD signal for KRAA_42 peptides at 50, 100, 150, and 200 μM in the presence of 1.0 mM SDS. CD spectra were expressed in molar ellipticity.
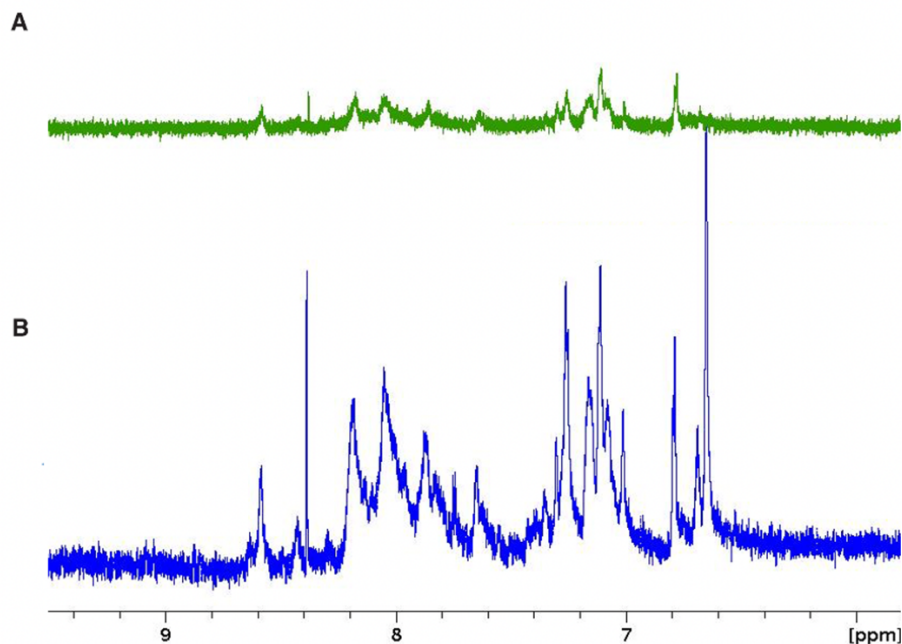
Figure 2.9. ^{1}H 1D NMR spectra of KRAA_42 showed line broadening, indicating sample inhomogeneity (A) ^{1}H 1D NMR of 100 μM KRAA_42 in pH 5.1 acetate buffer (50 mM deuterated acetate, 8 mM SDS, 10% D_2O) at 303 K. Number of scans of the direct excitation was 8 scans. (B) ^{1}H 1D NMR of 200 μM KRAA_42 in pH 5.1 acetate buffer (50 mM deuterated acetate, 10 mM SDS, 10% D_2O, 5% dimethyl sulfoxide) at 303 K. Number of scans of the direct excitation was 8 scans.
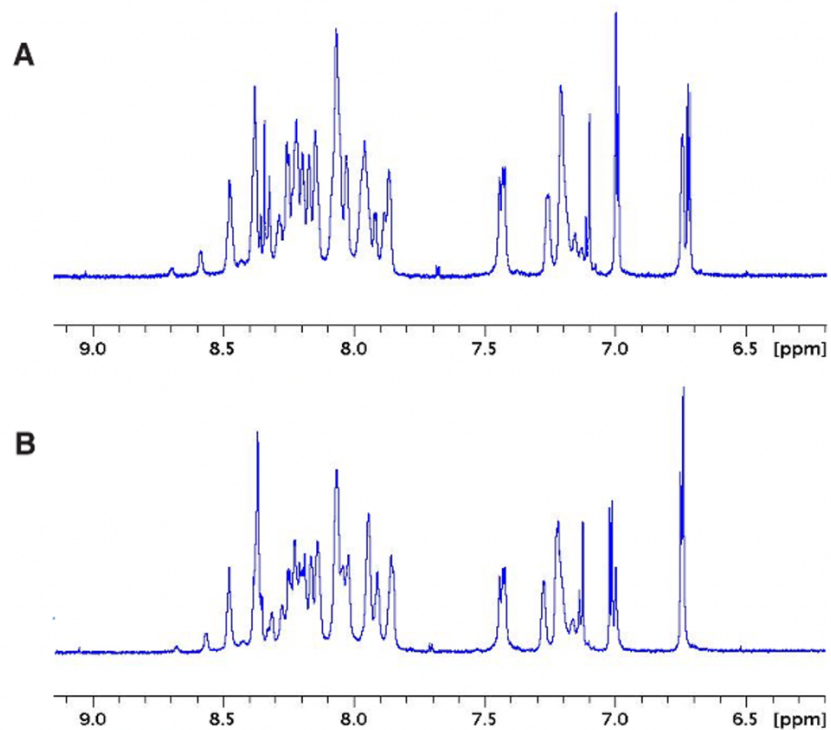
Figure 2.10. ^{1}H 1D NMR spectra of KRAA_42 in the presence of cosolvents and absent of SDS. (A) ^{1}H 1D NMR of 200 µM KRAA_42 in pH 5.1 acetate buffer (50 mM deuterated acetate, 10% D$_2$O) with 5% dimethyl sulfoxide at 303 K. Number of scans of the direct excitation was 8 scans. (B) ^{1}H 1D NMR of 200 µM KRAA_42 in pH 5.1 acetate buffer (50 mM deuterated acetate, 10% D$_2$O) with 5% acetonitrile at 303 K. Number of scans of the direct excitation was 8 scans.
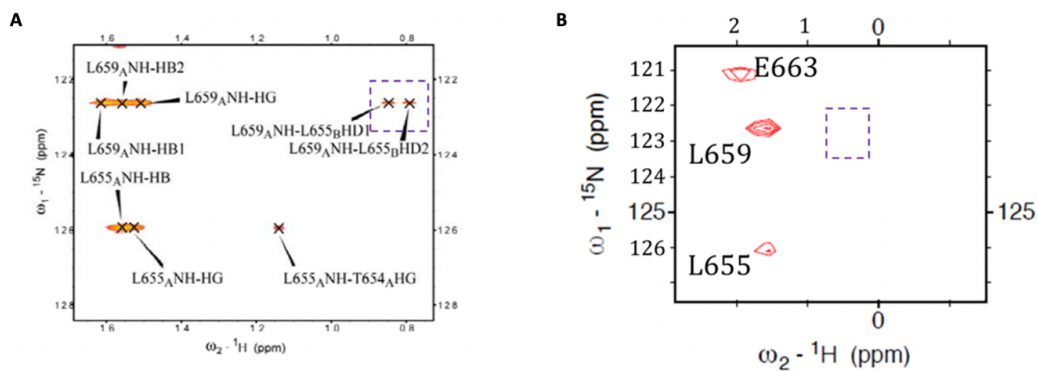
Figure 2.11. ^{15}N-^{1}H HSQC–NOESY spectra of the Jura_35 to probe the through-space connectivity between segments A and B in JM-dimer-mimicking peptide. (A) ^{15}N-^{1}H HSQC–NOESY spectrum reported by Jura and colleagues revealed both intra-segment and inter-segment through-space coupling interaction. (B) Replication of the reported ^{15}N-^{1}H HSQC–NOESY experiment. The inter-segment through-space coupling interactions (signal in the purple dashed box) were not observed under same experimental conditions. The experiments were performed at 293 K. The NOE mixing time was set to 300 ms.

Table 2.1. The JM-dimer-mimicking-peptides of interest

Peptide	Length	Sequence (N→C)	Expected structure	Charge
Jura_35	35	KRTLRRLLQERELVE-GSGSG-KRTLRRLLQERELVE	EGF-type	4+
E661R_35	35	KRTLRRLLQRRELVE-GSGSG-KRTLRRLLQRRELVE	EGF-type	8+
KRAA_35	35	ARTLARLLQERELVE-GSGSG-ARTLARLLQERELVE	TGF-α-type	Neutral
KRAA_41	41	RRHIVR-ARTLARLLQERELVE-GSGSG-ARTLARLLQERELVE	TGF-α-type	4+
KRAA_42	42	YRRHIVR-ARTLARLLQERELVE-GSGSG-ARTLARLLQERELVE	TGF-α-type	4+

Table 2.2. Buffer conditions tested for KRAA_42 solubility

Buffer	pH	SDS	Cosolvent	Solubility
50 mM acetate-d4	5.5	10 mM	15% DMSO	Partially soluble
50 mM acetate-d4	5.5	10 mM	10% DMSO	Partially soluble
50 mM acetate-d4	5.5	10 mM	5% DMSO	Partially soluble
50 mM acetate-d4	5.5	10 mM	15% MeCN	Partially soluble
50 mM acetate-d4	5.5	10 mM	5% MeCN	Partially soluble
50 mM acetate-d4	7.6	10 mM	5% DMSO	Partially soluble
10 mM phosphate buffer	7.1	10 mM	5% DMSO	Partially soluble
50 mM acetate-d4	5.5	0 mM	5% DMSO	Partially soluble
50 mM acetate-d4	5.5	0 mM	5% Acetone	Partially soluble
50 mM acetate-d4	5.5	0 mM	5% MeCN	Partially soluble

Chapter 3. Investigating the allosteric relationship between the transmembrane and the juxtamembrane domain

3.1. Abstract

Looking beyond the JM domain, the structural study described in this chapter used peptides that contain both the transmembrane domain (TM) and the JM domain segment to investigate the allosteric relationship within EGFR. Peptides that are expected to form the EGF-type coiled coil and TGF-α-type coiled coil JM conformation base on previously reported mutations[55] were synthesized and purified. Membrane mimics were explored to include lipid-peptide interactions and stabilize the hydrophobic transmembrane region. Bicelles and lipid nanodiscs (ND) were prepared as membrane mimics for peptide structural studies. The preparation and characterization of membrane-mimics/peptide samples particles were described. The sample homogeneity of membrane-mimic/peptide was examined with 1D ^{1}H NMR experiments. Dynamic light scattering (DLS) was used to probe the particle size of the membrane mimic particle and its stability. The preparation of the membrane scaffold protein (MSP) with protein expression was reported and characterized. MSP was used for ND assembly. The assembled NDs were analyzed with size exclusion chromatography (SEC) and DLS, establishing a membrane mimic strategy for studying the structure of the TM and JM of EGFR with amphiphilic peptides.

3.2. Introduction

The attempt to resolve the EGF-type and TGF-α-type JM coiled coil using the JM-dimer-mimicking peptide was described in chapter 2. Nonetheless, despite CD characterization confirmed α-helical secondary structure within the prepared peptides, 1D NMR results revealed a heterogeneous peptide sample in the reported buffer. Moreover, 2D NMR showed a lack of proper JM coiled coil folding of the dimer-mimicking peptide. The transient folding of the JM-dimer-mimicking peptide was also observed previously.[23] The results that the JM-mimicking peptide required stabilization by cosolvents and the knowledge that the JM domain exhibits interaction with the plasma membrane[29,56,57,111] implies a wider structural view with more stabilizing interaction is required for a relevant and stable system. NMR studies showed that the JM-A helix may be a transient structure[23,48] and dynamic relative to the TM helix.[48] The absence of negatively charged lipids to stabilize JM-A was also proposed to give rise to its flexibility.[111] Therefore, in this study, the peptide segment was expanded to include both the TM domain and the JM domain. In addition, I used membrane mimics for stability. The use of the peptide containing TM and JM segments in NMR structural studies were reported.[29,48,112,113] However, no reports have been made on the allosteric relationship between the TM cross-angle and JM coiled coil conformation. Thus, I made use of the JM-switching mutants Sinclair and colleagues[55] reported and aimed to resolve the TM and JM high-resolution structure. Membrane mimic bicelles and lipid nanodiscs were prepared to provide a membrane environment for the TM and TM peptides.

3.2.1. JM-switching single mutations at the TM GXXXG motif

Sinclair and colleagues reported single mutations at the TM domain of the EGFR that alters the structure of the JM coiled coil with bipartite tetracysteine display experiments.[55] When G628 of the traditional GXXXG motif[49–51] in the TM was mutated to Phe or Val, the relationship between the JM coiled coil conformation and the identity of the bound growth factor identity was

decoupled. When Gly was mutated to bulky and hydrophobic residue Phe (G628F), the JM conformation was the EGF-type JM coiled coil. When Gly was mutated to Val (G628V),[54] the JM conformation was the TGF-α-type JM coiled coil. Finally, when Gly was mutated to another small, non-polar residue Ala (G628A), the mutation was conservative and is assumed to exhibit no significant changes in structure. The effect on JM thus is expected to be consistent with the wild type. In the same paper, Sinclair and colleagues reported that *in silico* the formation of TGF-α-type JM coiled coil was more probable when TM cross-angles at G625 were large,[55] and thus fewer cross-location. The TM helix dimer angle among the *in-silico* structures containing a TGF-α-type JM coiled coil was −36 ± 5°, and the corresponding TM-helices angle among structures containing an EGF-type JM coiled coil was −27 ± 6°. The studies in this chapter aimed to verify these structures experimentally with peptides containing TM and JM domains and high-resolution NMR methods.

3.2.2. Phospholipid bilayer membrane mimics to facilitate high-resolution structure determination of membrane proteins

To study the protein and peptide sample containing hydrophobic transmembrane regions, membrane mimics were developed and used to stabilize the macromolecule and provide a native-like membrane environment to ensure the structural integrity of the determined structure. Detergent micelles,[111,112,114,115] lipid/detergent bicelles,[48,113,115,116] lipid nanodiscs (ND),[114,117–124] amphipols,[125–128] and liposomes[129–132] are some of the developed membrane mimics (**Figure 3.1**). They vary in popularity among scientists with preferred experimental tools and depending on the goal of the studies.[133] For high-resolution NMR studies, homogeneity and tumbling are important criteria to meet. Micelles and bicelles are simple systems and small in size thus making them popular among NMR studies.[133] However, structural studies with peptides containing EGFR TM and JM domain using micelles and bicelles resulted in different structures.[134] Micelles are made by detergents to form aggregates with the hydrophilic head regions in contact with surrounding aqueous solvent and sequestered hydrophobic tail regions in the micelle center (**Figure 3.1**). Micelles mostly exhibit spherical shapes but can take on ellipsoids, cylinders, and bilayer forms at certain conditions. Bicelles are formed by mixing either two lipid species with different carbon chain lengths or with a lipid species and a detergent species. Bicelles are discoidal shaped with the long chain lipid species forming the bilayer and the short lipid species or the detergent forming the disk rim (**Figure 3.1**). In lipid nanodiscs (NDs), lipid molecules assemble into a disc of lipid-bilayer with the hydrophobic chains band together by the amphipathic membrane scaffold protein (MSP). NDs have gained popularity for the structural and functional study of membrane proteins in the past two decades (**Figure 3.1–3.3**).[118] Amphipols are short amphipathic polymers that substitute for the detergents in the disc-shape micelle (**Figure 3.1**). Amphipols have been shown to prevent membrane protein oligomerization by selectively adsorbing to hydrophobic transmembrane surfaces.[127,135] Liposomes is a good candidate for artificial cells for its high dynamic mobility and size comparable to cells (Small unilamellar vesicles: 20–100 nm; large unilamellar vesicles: 100–1000 nm; giant unilamellar vesicles: 1–200 mm; Animal cells: 10–30 mm; Plant cells: 10–100 mm).[131] On the other hand, liposome is not a good choice for high-resolution NMR studies due to their size being large and highly polydisperse. The abovementioned membrane mimics have been used for membrane protein structural studies. In this chapter, the studies focus on two of the membrane mimics—bicelles and ND.

Bicelles containing TM and JM segments (coined the TM-JM) have been reported to resolve the high-resolution TM-JM structure with NMR experiments by Endres and colleagues.[48] Uniformly labeled ^{15}N^{13}C TM-JM segments were prepared in DMPC/DHPC bicelles. TM-JM segment formed a helical structure as indicated by ^{13}C$_\alpha$ secondary chemical shifts and backbone dihedral angle predictions from backbone ^{13}C, ^{15}N, and ^{1}H chemical shifts. The structural model for the TM-JM dimer was generated using intramolecular NOEs as distance restraints of the backbone, predicted side chain angles restraints, and predicted backbone dihedral angle restraints.

Membrane scaffold protein (MSP) nanodiscs (ND) were first developed by the Sligar lab based on human apolipoproteinA-I (ApoA-I).[136,137] MSP proteins fold into amphipathic α-helical structures and wrap around the lipid hydrophobic chain to form a discoidal phospholipid bilayer. Two copies of MSP are in an ND in an antiparallel orientation. Since the introduction of MSP ND at about two decades ago, it has been increasing in popularity for membrane protein studies (**Figure 3.2**). The diameter of MSP ND can be decided by the length of the MSP construct used (**Figure 3.3**). The most used MSP is MSP1D1. Removal of the N-terminal globular domain (the first 43 residues) of ApoA-I makes the MSP1 construct.[138] A further removal of the next 20 N-terminal amino acids makes the MSP1D1 construct. The size of MSP1D1 ND is ~10 nm and a molecular mass of ~150 kDa.[118] There are also options for preparing smaller ND particles with truncated MSP variants. Deletions of helices 4 and 5 (MSP1D1 ΔH4–5) or having only H4 or H5 alone (MSP1D1ΔH4 and MSP1D1ΔH5) resulted in stable nanodiscs with diameters of about 7.1 and 8.4 nm (66 and 95 kDa), respectively.[118,119] MSP1D1 has been used for single-pass membrane protein studies like EGFR[85] and human CD4,[139] and granted the freedom to modify lipid type and composition. In summary, MSP ND is an established membrane mimetic system for membrane proteins and provides a native-like environment for more realistic conformational changes.

3.3. Results

3.3.1. Protein synthesis, purification, and characterization

The TM-JM segment of interest was an updated version of the TM-JM reported by Endres and colleagues which the structure was resolved with NMR experiments.[48] Endres and colleagues prepared the uniformly labeled ^{15}N^{13}C TM-JM protein with E. coli BL21(DE3) protein expression. The purification strategy was to express TM-JM in the inclusion body, thus the construct included insoluble fusion tags TrpΔDLE leader peptide at the N-terminal and ΔEpsilon at the C-terminal. To cleave the insoluble fusion tags with cyanogen bromide (CNBr) cleavage reaction, Endres and colleagues mutated two Met in the TM-JM sequence into Leu and Ile. In this work, the TM-JM segment was a 50-residue synthesis product. The stepwise coupling of solid-phase peptide synthesis provides a high level of freedom to prepare proteins with site-specific mutation (TM mutations G628F, G628V, and G628A that controls JM coiled coil) and isotopic labeling of selected residues (TM cross-location residues: G625, A629, V636 to measure nuclear distances and deduce cross-angle; JM coiled coil residue: L655 and R657. Two L655 residues in the JM antiparallel coiled coil come in close contact in the EGF-type coiled coil. Two L655 residues in the JM antiparallel coiled coil come in close contact in TGF-α-type coiled coil.) (**Figure 3.4**). The TM-JM protein variant of interest is listed in **Table 3.1**. The TM-JM protein consists of 34 amino acids from the TM sequence and 15 amino acids from the JM-A sequence. An additional Tyr residue was designed at the N-terminal concentration determination with UV absorbance at 280 nm. The

peptides of interest were synthesized using a semi-automatic solid-phase peptide synthesis (SPPS) instrument, cleaved from the solid-support resin, lyophilized, and purified with reversed-phase high-performance liquid chromatography (RP-HPLC). The purified fractions were characterized by liquid chromatography-mass spectrometry (LC-MS) and analytical ultra high performance liquid chromatography (UPLC) (**Figure 3.5**).

3.3.2. Characterization of TM-JM protein in bicelle membrane mimic

The bicelle samples were prepared using DMPC (1,2-dimyristoyl-sn-glycero-3-phosphocholine) and DHPC lipids (1,2-dihexanoyl-sn-glycero-3-phosphocholine) following previously reported methods.[48] The q value (also called q factor), defined as the ratio between the long-chain and the short-chain phospholipid, DMPC/DHPC, was 0.25 (**Figure 3.6.A and B**).[48,140] The bicelle samples were prepared in 10 mM potassium phosphate buffer (pH 6.2, 1 mM EDTA, 1 mM DTT) The TM-JM protein concentration was 0.3 mM. The lipid concentration was 45 mM (for a protein-to-lipid ratio of 1:150).[48] Dynamic light scattering (DLS) measured the sizes of bicelles prepared without (empty bicelles) and with the TM-JM protein as 4.43 ± 1.04 nm (**Figure 3.6.C**) and 5.4 ± 0.9 nm (**Figure 3.6.D**) in diameter, comparable to the reported value.[48] The NMR sample was prepared in the same method but with deuterated lipids DMPC-d54 and DHPC-d22 and included 7% D_2O in the phosphate buffer. ^{1}H 1D NMR of bicelle-TM-JM was performed to examine the homogeneity of TM-JM protein in the bicelle membrane mimic environment (**Figure 3.7**). The signal in the amide proton chemical shift region for the TM-JM protein had resolutions of ~0.5 ppm. Typically, the number of signals at the amide proton chemical shift region corresponds to the number of residues in the protein. Each amide proton gives rise to a unique chemical shift. Thus, the expected number of peaks for the TM-JM protein is ~50 peaks. Nonetheless, the observed number of peaks was ~14 peaks at 298 K (**Figure 3.7.B**). The TM-JM protein construct consists of 34 amino acids from the TM sequence and 15 amino acids from the JM-A sequence. Thus, the resolved 14 peaks could be from the 15 residues in the flexible JM region while the motions of the TM residues were restricted in the bicelle phospholipid bilayer. Increasing the experimental temperature from 298 K (**Figure 3.7.B**) to 311 K (**Figure 3.7.A**) resolved more peaks to ~19 peaks. Raising in temperature to improve resolution can be explained by the 'tumbling problem', during which large molecules like proteins tumble relatively slowly in solution producing greatly broadened spectral lines as a result of fast transverse relaxation.[141] Higher temperature increased the tumbling of the bicelle-TM-JM and resolved additional peaks. The stability of the bicelle-TM-JM through time was examined with DLS experiments (**Figure 3.8**). The diameter of the bicelle-TM-JM particles was 5.4 ± 0.9 nm on the same day of bicelle-TMJM preparation. However, aggregation of bicelle-TM-JM in the solution was evidenced by DLS measurement of a 56 ± 22 nm diameter after a day, even though no visible precipitation was observed with the naked eye. Appropriate bicelle optimization is required for the bicelle-TM-JM sample system. Parameters for optimization include the selection of lipids and detergents,[113] q value,[48,140] and final lipid concentration.[140,142]

3.3.3. Characterization of membrane scaffold protein (MSP) and nanodisc (ND)

An alternative membrane mimetic system is the MSP ND. The most common membrane scaffold protein MSP1D1 (**Figure 3.3**) was chosen for the nanodisc preparation. The reported size of

MSPD1 ND is ~9.7 nm in diameter[85,118,143] and has been used for EGFR structural study.[85] The plasmid for MSP1D1 expression was purchased from Addgene with an N-terminal His-tag, a TEV cleavage site, and the MSP1D1 in its construct. His$_7$-MSP1D1 was expressed in *E. coli* BL21(DE3) (**Figure 3.9**) and purified by affinity chromatography with Ni-NTA agarose resin (**Figure 3.9.A**). The purified His$_7$-MSP1D1 was subjected to TEV protease to cleave the fusion protein. The His-tag was removed by another purification step with Ni-NTA agarose resin, with MSP1D1 in the flow-through and wash fraction, but the cleaved His-tag and the his-tagged TEV protease was eluted by the imidazole-containing elution buffer (**Figure 3.9.B**). The purified MSP1D1 was visualized with SDS-PAGE (sodium dodecyl sulfate–polyacrylamide gel electrophoresis) (**Figure 3.9.B**) and characterized with LC-MS (**Figure 3.9.C**).

The method for lipid nanodisc assembly was adopted from previously reported methods.[85,139] The assembly process started by mixing and dissolving MSP1D1, membrane protein, and selected phospholipids in an aqueous solution with detergent. The following steps were gradual removal of the detergents using hydrophobic adsorbent media, such as Bio-beads SM-2 and Amberlite XAD-2, or by dialysis.[136,144,145] During the detergent removal step, MSP ND self-assembles into the discoidal structure with a phospholipid bilayer at the center, wrapped around by the amphipathic α-helices of MSP (**Figure 3.1.C**). The phospholipids chosen for ND assembly were POPC (16:0-18:1 PC, 1-palmitoyl-2-oleoyl-glycero-3-phosphocholine) and POPS (16:0-18:1 PS, 1-palmitoyl-2-oleoyl-sn-glycero-3-phospho-L-serine) with the composition of 85% POPC and 15% POPS. There were several justifications for this selection: (a) Phosphatidylcholine (PC) is the main component in the mammalian cell plasma membrane (with ~5–10% PS)[146]; (b) POPC and POPS have reasonable liquid-crystalline phase-transition temperatures (–2 °C for POPC and 14 °C for POPS)[118]; most importantly (c) 85% POPC and 15% POPS stabilize the TM conformation consistent with the reported structure.[48,55,111] To characterize the MSP1D1 lipid ND, empty ND was assembled (ND without the TM-JM protein) and fractionated by size exclusion chromatography (SEC). The size of MSP1D1 ND is ~10 nm and a molecular mass of ~150 kDa.[118] The SEC column was a HiLoad 16/600 Superdex 200pg column with a fractionation range of 10–600 kDa, ensuring monodispersing the species in SEC fractions. SEC trace showed three species from the nanodisc assembly mixture (**Figure 3.10.A**). Liquid chromatography (LC) of the three species was compared to MSP1D1 and POPC/POPS-lipid-mixture standards (**Figure 3.10.B**). LC retention time resolved the MSP1D1 protein and POPC/POPS-lipid-mixture from the nanodisc assembly mixture. Semi-quantitative characterization with LC showed that the peak 1 of the SEC fraction was mostly consisted of POPC/POPS lipid. Considering the structure and arrangement of MSP and phospholipid in the nanodisc, the higher the lipid-to-MSP ratio, the larger the planar region of the discoidal nanodisc and thus the larger the nanodisc size. The peak 2 was presumably larger in size than the peak 3 for the larger lipid-to-MSP ratio. This interpretation was collaborated by DLS measurements. The DLS determined the size of the three species to be 31.6 ± 9.8 nm, 10.9 ± 3.1 nm, and 7.9 ± 1.9 nm.

3.4. Conclusion

High-resolution structural studies of the JM conformation with protein segments require a system that contains the TM and the phospholipid membrane to imitate the JM-membrane interaction.[29,56,57,111] The aim of this study was also to reveal the allosteric relationship between the TM cross-angle and JM coiled coil conformation[55] at high structural resolution. The selected

phospholipid bilayer membrane mimics to facilitate high-resolution structure determination of the TM-JM proteins were bicelles and nanodiscs. Bicelles are discoidal-shaped structures that are relatively simple to prepare. However, the bicelle-TM-JM sample experienced the 'tumbling problem' as shown by ^{1}H 1D NMR. Bicelle-TM-JM aggregated after a day from bicelle preparation, forming particles that about 10-fold in larger than the initial size. The stability and molecular tumbling of bicelle samples requires improvement via appropriate bicelle optimization, including the choice of lipid species,[113]optimizing q value,[48,140] and optimizing final lipid concentration.[140,142]

The other membrane mimic prepared and characterized was the lipid nanodiscs (ND). The most used membrane scaffold protein variant MSP1D1 was prepared with *E.coli* expression and purified by affinity chromatography. Lipid nanodisc self-assembled as the detergent was slowly removed from the assembly mixture.[85,139] The POPC/POPS nanodisc was assembled and fractionated by SEC. The SEC resolved three species from the nanodisc assembly mixture with varying lipid-to-MSP ratios and sizes. Building on these data, the work that follows is assembling nanodiscs that contain the TM-JM protein. Characterization of nanodisc-TM-JM is described in chapter 4 as one of the future directions.

3.5. Methods and Materials

Materials. DMPC (1,2-dimyristoyl-sn-glycero-3-phosphocholine) and DHPC lipids (1,2-dihexanoyl-sn-glycero-3-phosphocholine) for the assembly of bicelles were the products of Avanti Polar Lipids. DMPC-d54 (1,2-dimyristoyl-d54-sn-glycero-3-phosphocholine) and DHPC-d22 lipids (1,2-dihexanoyl-d22-sn-glycero-3-phosphocholine) were the products of MilliporeSigma. POPC (16:0-18:1 PC, 1-palmitoyl-2-oleoyl-glycero-3-phosphocholine) and POPS (16:0-18:1 PS, 1-palmitoyl-2-oleoyl-sn-glycero-3-phospho-L-serine) for the assembly of nanodisc were the products of Avanti Polar Lipids. 2,2,2-Trifluoroethanol-d3 (TFE-d3) was the product of Sigma-Aldrich. The plasmid pMSP1D1 was purchased from Addgene. The *E.coli* BL21 (DE3) competent cells was a product of New England Biolabs. Miller's Luria Broth (LB Broth) powder was the product of Thomas Scientific. Isopropyl-β-D-thiogalactopyranoside (IPTG) was a product of Fisher Scientific. Dulbecco's phosphate buffered saline (DPBS) was a product of ThermoFisher Scientific. cOmplete™ EDTA-free protease inhibitor cocktail tablets were products of Roche Life Science. Triton X-100 was a product of Research Products International. The Ni-NTA nickel-charged agarose resin was a product of Qiagen. The TEV protease was obtained from Berkeley QB3 MacroLab. The Mini-PROTEAN TGX precast gels and the Precision Plus Dual Color Standards were products of Bio-Rad Laboratories.

Solid-phase peptide synthesis. The peptides of interest were prepared with solid-phase peptide synthesis with the Biotage® Initiator+ Alstra automated single-channel microwave peptide synthesizer. H-Rink amide ChemMatrix resin was used as the solid support. The synthesis scale was 50 µmol. SPPS utilizes an orthogonal protection scheme. The base-labile fluorenylmethyloxycarbonyl (Fmoc) protecting group of the α-amine was removed during deprotection reaction mixing in 20% piperidine (Sigma-Aldrich) in N, N-Dimethylformamide (DMF, Fisher Scientific) at room temperature for 5 min. The Fmoc-protected amino acid were products of Novabiochem except for ^{15}N-Leu-Fmoc and ^{13}C, ^{15}N-Glu-Fmoc. ^{15}N-Leu-Fmoc and ^{13}C, ^{15}N-Glu-Fmoc were products of Cambridge Isotope Laboratory. The coupling reagents were Hydroxybenzotriazole (HOBt, Sigma-Aldrich), (2-(1*H*-benzotriazol-1-yl)-1,1,3,3-

tetramethyluronium hexafluorophosphate (HBTU, Sigma-Aldrich), and N,N-Diisopropylethylamine (DIPEA, Spectrum Chemical). The coupling mixture consisted of Fmoc-protected amino acid, HOBt, HBTU, and DIPEA with the ratio 1:1:0.98:2. The coupling mixture reacted with the elongating peptide by mixing at 75 °C for 5 min. The coupling condition for Arg residues was twice at 75 °C for 5 min. His residues were coupled twice at 50 °C for 5 min to avoid racemization at high temperatures. The resulting resin-bound peptide was mixed with an acidic cleavage cocktail at room temperature for 4 hrs to cleave the acid-labile side chain protecting group and acid-labile resin linker. The cleavage cocktail consisted of 92.5% trifluoroacetic acid (TFA, Sigma-Aldrich), 2.5% 1,2-ethanedithiol (EDT, Sigma-Aldrich), 2.5% triisopropylsilane (TIPS, Sigma-Aldrich), and 2.5% deionized water (Millipore Milli-Q lab water system). The cleaved peptide was then precipitated in ice-cold diethyl ether. The precipitated peptides were dissolved in 15% (v/v) acetonitrile and dried with a freeze-dryer (Labconco, FreeZone 4.5 plus).

High-performance liquid chromatography. Freeze-dried peptides were dissolved in 15% (v/v) acetonitrile and were purified with reverse-phase high-performance liquid chromatography (RP-HPLC, Agilent 1260 Infinity II LC System) using C8 reverse-phase HPLC column (Vydac 208TP C8, Avantor). The solvents used were Milli-Q deionized water with 0.1% TFA and acetonitrile with 0.1% TFA. The purification gradient was 30–40% B over 20 mins at a flow rate of 4 mL/min. The fraction was detected with a UV detector at 214 nm and 280 nm.

Ultra high performance liquid chromatography. The purity of HPLC purified fractions was analyzed with reverse-phase ultra high performance liquid chromatography (UPLC, UHPLC, Shimadzu, Prominence HPLC) using a C18 analytical column (Agilent Poroshell 120 SB-C18 2.7 um). The solvents used were Milli-Q deionized water with 0.1% TFA and acetonitrile with 0.1% TFA. The gradient was 20–60% B over 10 mins at a flow rate of 0.5 mL/min and pressured at ~2100 psi. The fraction was detected with a UV detector at 214 nm and 280 nm.

Liquid chromatography–mass spectrometry. The mass of HPLC purified fractions were analyzed using Waters ACQUITY LC-MS System with C18 Waters analytical column.

Bicelle sample preparation. The bicelle sample was prepared following previously reported methods.[48] The bicelle sample was prepared by dissolving freeze-dried purified TM-JM protein in TFE (to a final TM-JM protein concentration of 0.3 mM), mixed with DMPC and DHPC at a protein to lipid ratio of 1:150, and q factor of 0.25.[140] The mixture was dried to a film with N_2 gas overnight. The dried film was resuspended in sample buffer (10 mM potassium phosphate, pH 6.2, 1 mM EDTA, 1 mM DTT) by vortexing vigorously for several minutes followed by incubation on ice for 15 min and at 37°C for 15 min. Bicelle-TM-JM samples were subjected to at least 3 freeze-thaw cycles until a clear solution was obtained.

Dynamic light scattering. Dynamic light scattering measurements were performed with a Malvern Zetasizer Nano ZS instrument equipped with a 532 nm laser. For Bicelle size measurements, the refractive index was set to 1.45, absorption was set to 0.001. The dispersant parameters for the phosphate buffer were viscosity = 0.8869 cP and refractive index = 1.33. For nanodisc size measurements, the refractive index was set to 1.45, absorption was set to 0.001. The dispersant parameters were viscosity = 0.9133 cP and refractive index = 1.3 for the 10 mM sodium phosphate buffer containing 150 mM NaCl. Each size data was an average of triplicate measurements.

Nuclear Magnetic Resonance Experiments. ^{1}H 1D NMR experiments were performed on Bruker 900 MHz spectrometer at 298 K and 311 K. The ^{1}H frequency was set to the water resonance. A

constant relaxation delay period of 1 s was used. NMR spectra were processed by the Bruker TopSpin software.

MSP1D1 expression and purification. The plasmid pMSP1D1 was purchased from Addgene. pMSP1D1 construct encodes an N-terminal His-tag and TEV cleavage site between the His-tag and MSP1D1 (His$_7$-TEVsite-MSP1D1). The plasmid was introduced to the *E.coli* BL21(DE3) competent cells with the transformation protocol that came with the New England Biolabs competent cell product via a heat shock method. Cells were grown in LB media at 37 °C and 225 rpm for ~2.5 hrs until reaching optimal cell density of OD 0.6–0.8 before isopropyl-β-D-thiogalactopyranoside (IPTG) was added to reach a final concentration of 1 mM to induce the production of the target protein. After 4.5 hrs of induction at 37 °C and 225 rpm, cells were harvested by centrifugation at 4300 g and 4 °C for 20 min. Cell pellets were resuspended in Dulbecco's phosphate-buffered saline (DPBS) supplemented with cOmplete™ EDTA-free protease inhibitor cocktail tablets and 1% Triton X-100. 2.5 mL of buffer was used per gram of cell pellets. The cell suspension was stored at –80 °C. Cells were lysed with EmulsiFlex-C3 high-pressure homogenizer and the lysate was cleared with centrifugation at 11419 g and 4 °C for 30 mins. The protein expression and cell lysis were confirmed with SDS-PAGE. The cleared lysate was added to Ni-NTA nickel-charged agarose resin and rotated at room temperature for 2.5 hrs and loaded to an empty column 1.5 cm in diameter. The flow-through was collected for SDS-PAGE characterization. The column was washed with four bed volumes of each of the following: (1) 40 mM Tris/HCl, 0.3 M NaCl, 1% Triton, pH 8.0; (2) 40 mM Tris/HCl, 0.3 M NaCl, pH 8.0; (3) 40 mM Tris/HCl, 0.3 M NaCl, 50 mM imidazole. The purified His$_7$-TEVsite-MSP1D1 fractions were combined and dialyzed against TEV protease cleavage buffer (50 mM Tris-HCl pH 8.0, 0.5 mM EDTA, 1 mM DTT) using slide-a-lyzer 3,500 MWCO cassettes G2 at 4 °C overnight. His$_7$-TEVsite-MSP1D1 was cleaved at RT for ~2 hrs with using 1 mg TEV protease per 20 mg substrate. After cleavage, the reaction mixture was dialyzed against 20 mM Tris, pH 8.0, 150 mM NaCl using slide-a-lyzer 3,500 MWCO cassettes G2 (ThermoFisher Scientific) at 4 °C overnight. The dialyzed mixture was added to Ni-NTA nickel-charged agarose resin and rotated at room temperature for 2.5 hrs and loaded to an empty column 1.5 cm in diameter. The flow-through was collected for SDS-PAGE characterization. The column was washed with 3 bed volumes of each of 20 mM Tris, pH 8.0, 150 mM NaCl, and eluted with 20 mM Tris, pH 8.0, 150 mM NaCl, 200 mM imidazole. The cleavage reaction and final purification were confirmed with SDS-PAGE using Mini-PROTEAN TGX precast gels and Precision Plus Dual Color Standards. The MSP1D1 was in flow-through and the washes, while the TEV protease and the His-tag were eluted by imidazole-containing elution buffer. The fractions containing purified MSP1D1 were combined, and the yield was determined using a microvolume UV-Vis spectrophotometer (NanoDrop 2000 Spectrophotometer, Thermo Scientific). The yield of purified MSP1D1 was ~31 mg (~1.4 μmol) per liter of LB expression media. The purified MSP1D1 was dialyzed against nanodisc assembly buffer (20 mM Tris-HCl, pH 7.4, 100 mM NaCl, 0.5 mM EDTA) at 4 °C overnight, and concentrated to ~2 mg/mL using Amicon Ultra-15 Centrifugal Filter Unit 10 kDa MWCO (Sigma-Aldrich). The MSP1D1 solution was aliquoted, freeze-dried, and stored at –80 °C until further use.

Preparation of empty MSP1D1 nanodisc. The procedure for the reconstitution of lipid nanodiscs was modified from previously described methods.[85,136,139] Lipid mixture of 85% POPC and 15% POPS was prepared to 50 mM in lipid buffer (20 mM Tris-HCl pH 7.4, 100 mM sodium cholate). The resulting lipid/detergent stock solution was clear after 10 mins of gentle agitation at 37 °C.

The freeze-dried MSP1D1 was redissolved with the original amount of DI water. Appropriate volumes of MSP1D1 solution and lipid/detergent stock solutions were combined to obtain a mixture of MSP:POPC:sodium cholate with a molar ratio of 1:40:80. The assembly mixture was incubated on ice for 30 mins. Bio-beads SM-2 (Bio-Rad) were added to the assembly mixture to remove the detergent sodium cholate and initiate self-assembly of MSP1D1 lipid nanodiscs. Bofore use, Bio-Beads were washed with 3 volumes of methanol, 10 volumes of water, and 10 volumes of assembly buffer. About 0.6 g of wetted Bio-Beads SM-2 were added per milliliter of assembly mixture. The first batch of Bio-beads SM-2 and the mixture were rotated at 4 °C continuously for 1 hr. The first batch of Bio-beads SM-2 was removed and a second batch was added to the mixture, and the sample was incubated overnight at 4 °C. A third and final batch of Bio-beads SM-2 was added to replace the second batch and rotated continuously at 4 °C for 2 hrs. Bio-beads SM-2 was cleared through centrifugation two times at 14,000 rpm for 10 mins. The mixture was fractionated by size-exclusion chromatography (SEC) using HiLoad 16/600 Superdex 200pg column (product of Cytiva, fractionation range: 10 to 600 kDa) operated on an ÄKTA Pure Protein Purification System (Global Life Sciences Solutions USA LLC). The SEC buffer was 10 mM sodium phosphate. pH 7.4, 150 mM NaCl, and the flow rate was 0.5 mL/min for fractionation.

Liquid Chromatography–Mass Spectrometry. The mass of the TM-JM protein and the MSP1D1 protein was analyzed with Agilent 6540 QTOF LC-MS System on an Agilent Poroshell C8 column. The deconvolution analysis was done with Agilent MassHunter Qualitative Analysis Navigator and Protein Deconvolution Software.
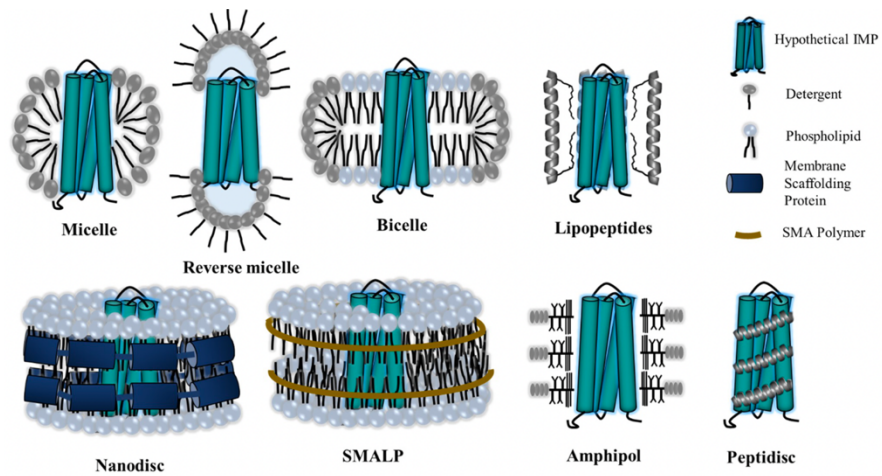
Figure 3.1. Common membrane mimetic systems for protein with transmembrane regions. The figure listed some of the membrane mimetic systems: micelle, reverse micelle, lipid/detergent bicelle, lipid nanodiscs, styrene-maleic acid lipid particles (SMALP), amphipols, lipopeptides, and peptidase. The membrane mimics utilize detergents, amphiphilic proteins, or amphiphilic polymers to stabilize phospholipid bilayers in the solution. Figure adapted from Ref. [133]
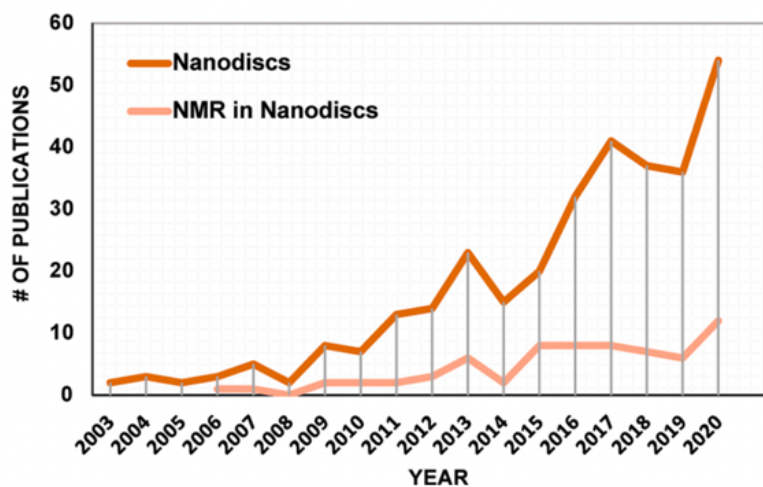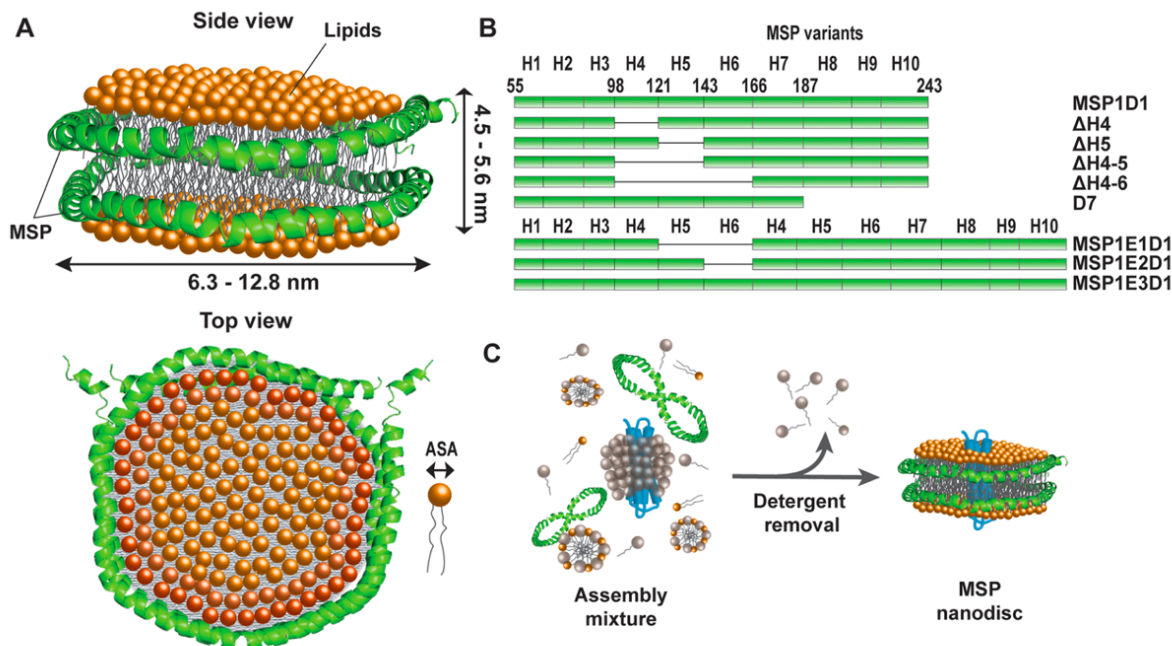
Figure 3.2. The number of publications including the search terms "membrane protein" and "nanodiscs" with or without "NMR" from the year 2003 to 2020. Nanosdiscs has gain popularity since its invention in 2002 for the structural and functional study of membrane proteins both in studies with NMR and without. Figure adapted from Ref. [118]

Figure 3.3. Structure, variants, and the assembly scheme of lipid nanodiscs. (A) The structure of membrane scaffold protein (MSP) lipid nanodiscs. MSP nanodiscs are made up of two copies of the MSP (green) forming amphiphilic helices and surrounding a patch of a phospholipid bilayer (orange). The size of a lipid nanodisc is typically 6.3–12.8 nm. (B) Available MSP variants with varying numbers of amphiphilic helices have been used for solution-NMR studies. The most common is the MSP1D1. There are truncated versions for smaller nanodiscs (MSP1D1ΔH4, MSP1D1ΔH5,[118,119] MSP1D1ΔH4-5, MSP1D1ΔH4-6, MSP1D7) that are attractive for NMR due to their smaller size. There are also extended versions (MSP1E1D1, MSP1E2D1, MSP1E3D1) for larger nanodiscs. (C) The assembly scheme of the nanodisc assembly process. Detergent (gray), lipids, MSP, and membrane protein of interest (blue) are dissolved in the assembly mixture in the appropriate ratio. The detergent is removed to initiate the nanodisc self-assembly process. The stoichiometry between the MSP and the lipids is defined by the size of the final nanodisc and the accessible surface area (ASA) of the used lipids and can be reliably estimated using geometric considerations.[143,147] Figure adapted from Ref. [118]
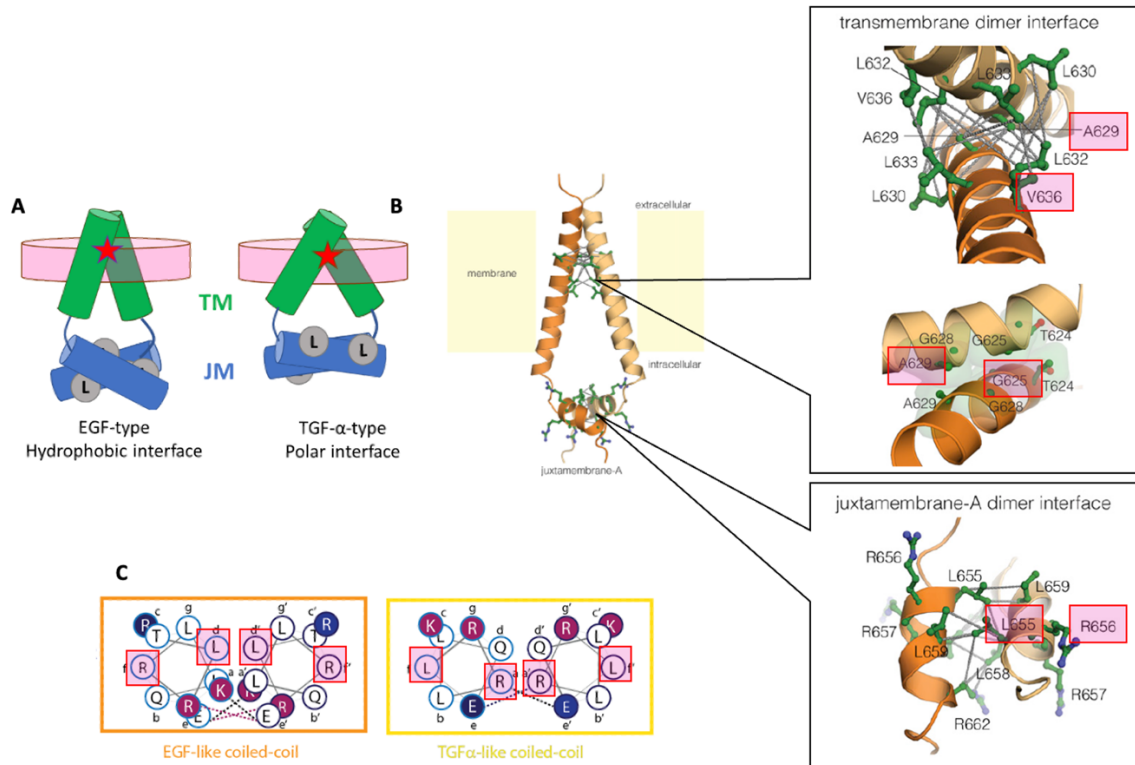
Figure 3.4. Structural allosteric relationship between the TM domain and the JM domain. (A) Illustration of TM-JM segments in a membrane system. The two models illustrate a single mutation at the GXXXG motif at the TM domain of the EGFR that alters the structure of the JM coiled coil. The smaller TM cross-angle corresponds to the EGF-type JM coiled coil and the larger TM cross-angles correspond to the TGF-α-type JM coiled coil.[55] (B) The structure of the TM and JM segment in DMPC/DHPC bicelle modeled from distance and angle restraints obtained from NMR experiments. The zoom-in inserts highlight the residue interactions at the cross-location of TM and the coiled coil interface of JM. The pink boxes indicate favorable residue options for isotopic labeling to probe TM cross-angle (G625, A629, and V636) and JM conformation (L655 and R656). Figure adapted from Ref. [48] (C) Helical wheel projection of the JM coiled coil. The projection shows the contact between residues L655 in the EGF-type JM coiled coil and residues R656 in the TGF-α-type JM coiled coil. Thus, L655 and R656 are favorable isotopic label sites for probing either the EGF-type or the TGF-α-type coiled coil. In each case, only a set of NOE signals will arise from the NMR measurements.
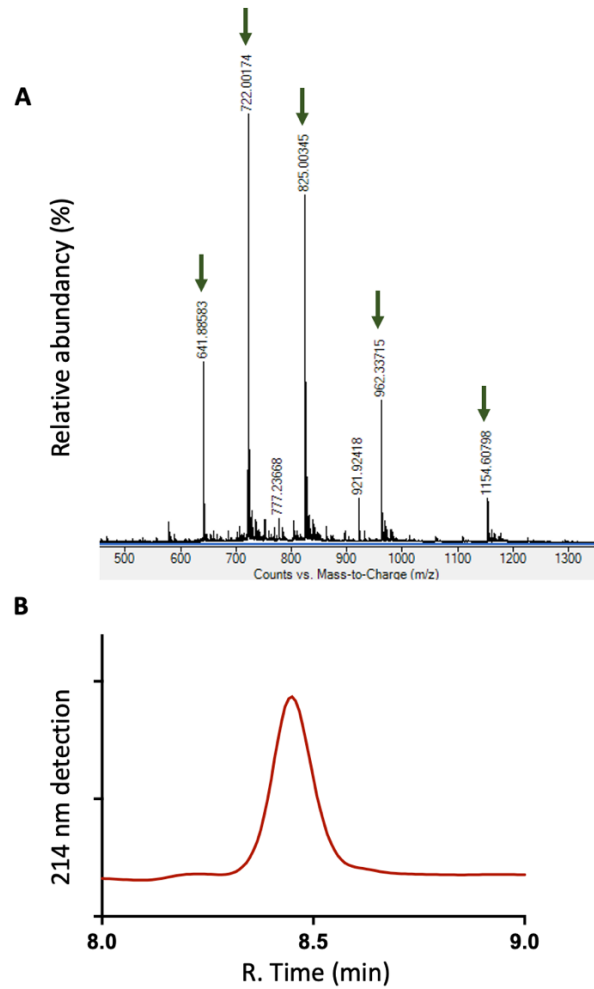
Figure 3.5. Characterization of HPLC purified WT-TM-JM protein. (A) LC-MS analysis of WT-TM-JM protein in a positive ion mode. The arrows indicated MS intensities of multi-charged species [M-nH]$^{n+}$. The theoretic molecular weight of WT-TM-JM is 5769.119. The deconvoluted molecular weight from multi-charged species was 5768.0 (B) The UPLC analysis of WT-TM-JM protein showed a single species with 214 nm detection on a C18 reverse-phase column.

A

(a) DHPC
short-chain lipid

(c) C$_8$E$_5$

40 Å

(b) DMPC
long-chain lipid

B

q = 2.5

q = 1

q = 0.5

q ~ 0

Detergent   Long chain lipid

C

Size Distribution by Number

Number (Percent)

Size (d.nm)

D

Size Distribution by Number

Number (Percent)

Size (d.nm)
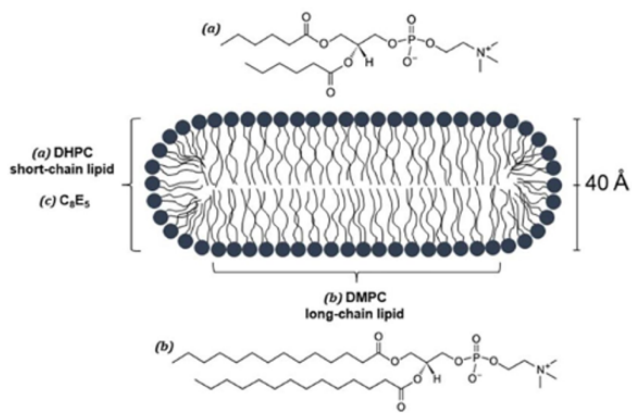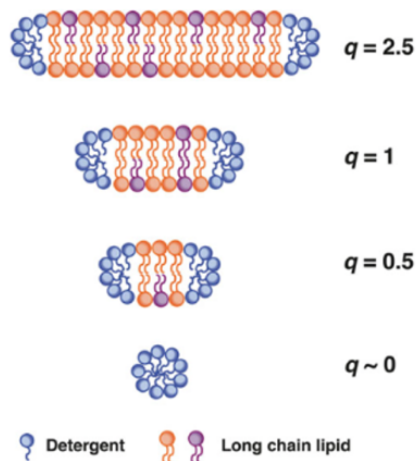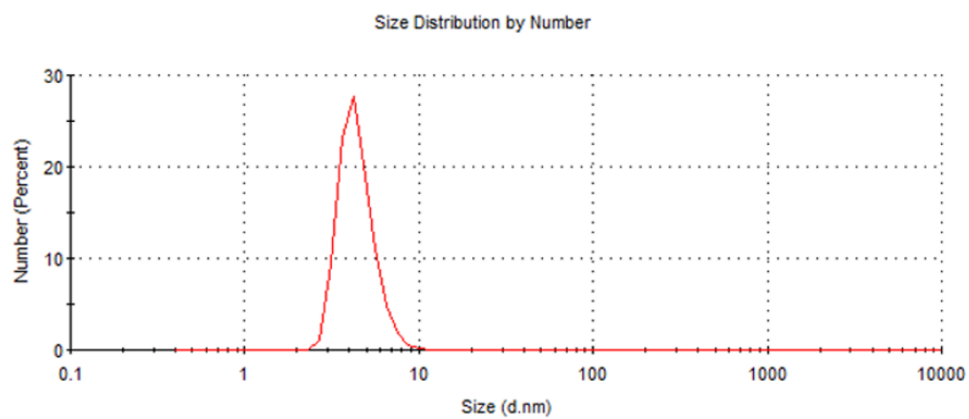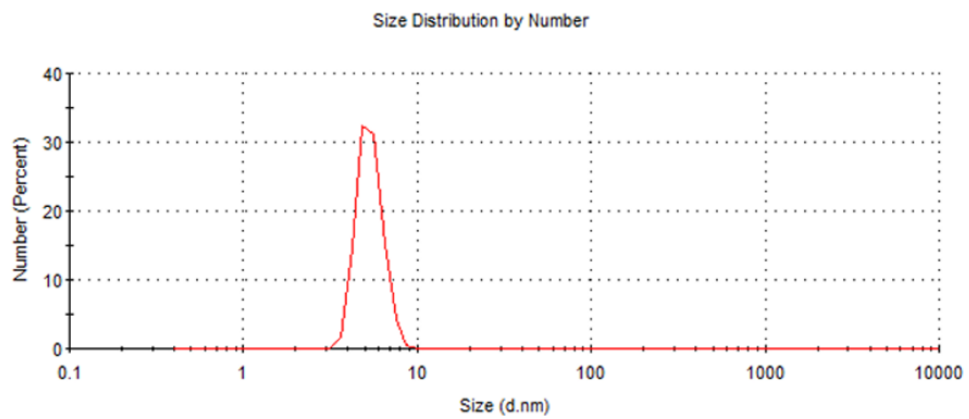
Figure 3.6. Parameter and characterization of bicelles. (A) The structure of a DMPC/DHPC bicelle. The long carbon chain DMPC forms the planar area of the discoidal bicelle and the short carbon chain DHPC forms the rim of the bicelle. Figure adapted from Ref. [148] (B) Illustration of the bicelle formed with different q values (or q factor). In detergent/lipid bicelles, q is defined as the ratio of lipid-to-detergent. In bicelles make up of long-chain and short-chain lipids, q is defined as the ratio between the long-chain and the short-chain phospholipid. The larger the q is, the larger the planar portion of the formed bicelle. Figure adapted from Ref. [149] (C) Dynamic light scattering (DLS) measurements of empty bicelles determined the size of 4.43 ± 1.04 nm in diameter (D) DLS measurements of bicelle-TM-JM determined the size of 5.4 ± 0.9 nm in diameter.
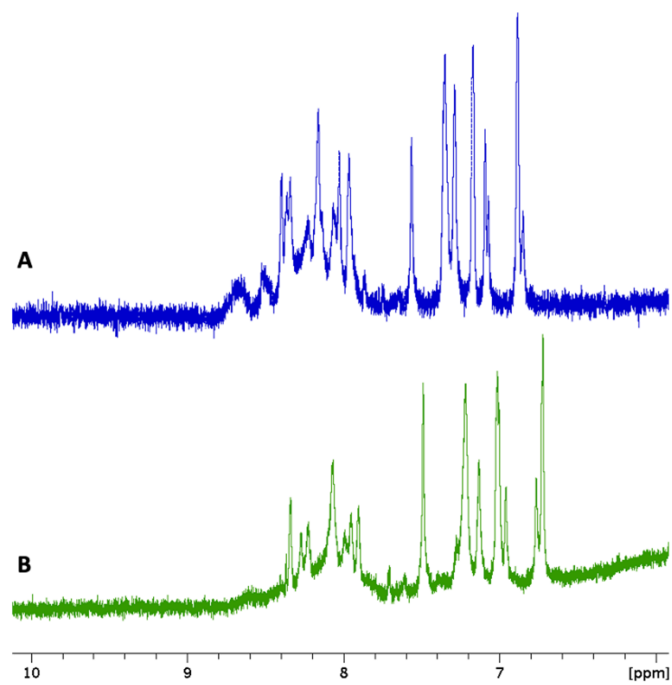
Figure 3.7. ^{1}H 1D NMR spectra of bicelle-TM-JM. Amide region of the ^{1}H NMR of bicelle-TM-JM at (A) 311K and (B) 298 K.
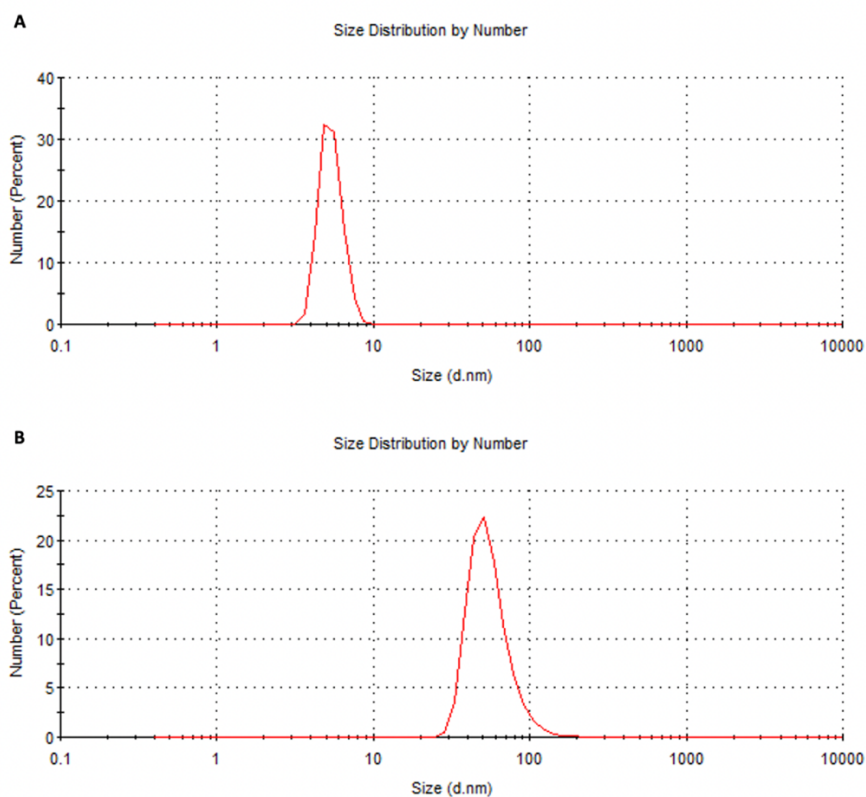
Figure 3.8. DLS experiments of bicelle-TM-JM. DLS measurements of bicelle-TM-JM were performed (A) on the day of bicelle-TM-TM preparation and (B) a day after bicelle-TM-JM preparation. The size of the prepared bicelle-TM-JM aggregated from 5.4 ± 0.9 nm to 56 ± 22 nm in diameter after a day in ambient condition.
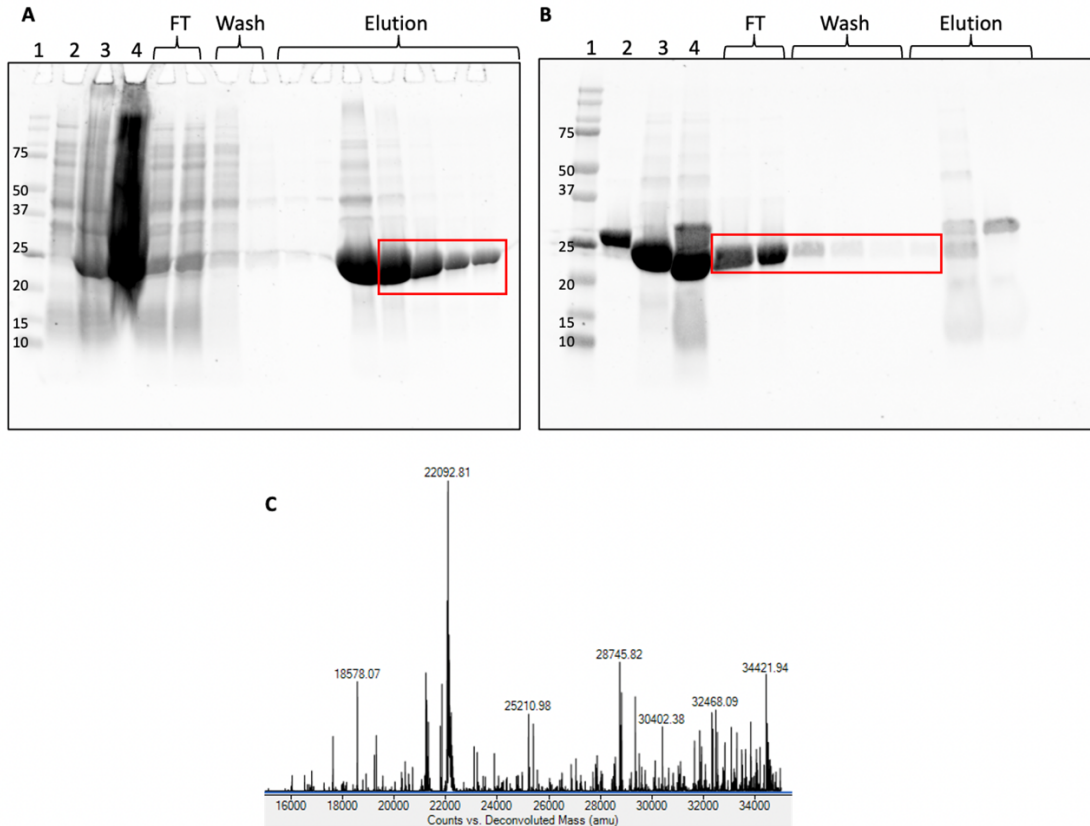
Figure 3.9. Protein expression and purification of MSP1D1. (A) SDS-PAGE image tracked MSP1D1 expression and purification using His-tag affinity to Ni-NTA agarose resin. Lanes 1–4 represent 1) Protein mass standards, 2) Pre-IPTG-induction, 3) Post-IPTG-induction, and 4) Cleared lysate before Ni-NTA purification. The red box indicates the separated His_7-MSP1D1 of 24.8 kDa. (B) SDS-PAGE image tracked His_7-MSP1D1 cleavage reaction and MSP1D1 purification using Ni-NTA agarose resin to remove the His-tag and TEV protease from the cleavage mixture. Lanes 1–4 represent 1) Protein mass standards, 2) TEV protease, 3) Pre-TEV-protease-cleavage, and 4) Post-TEV-protease-cleavage. The red box indicates the separated MSP1D1 of 22.0 kDa. The MW of TEV protease is 27.0 kDa (C) The purified MSP1D1 was characterized with QTOF LC-MS System. The deconvolution analysis was done to show the purified MSP1D1 with a mass of 22.1 kDa.
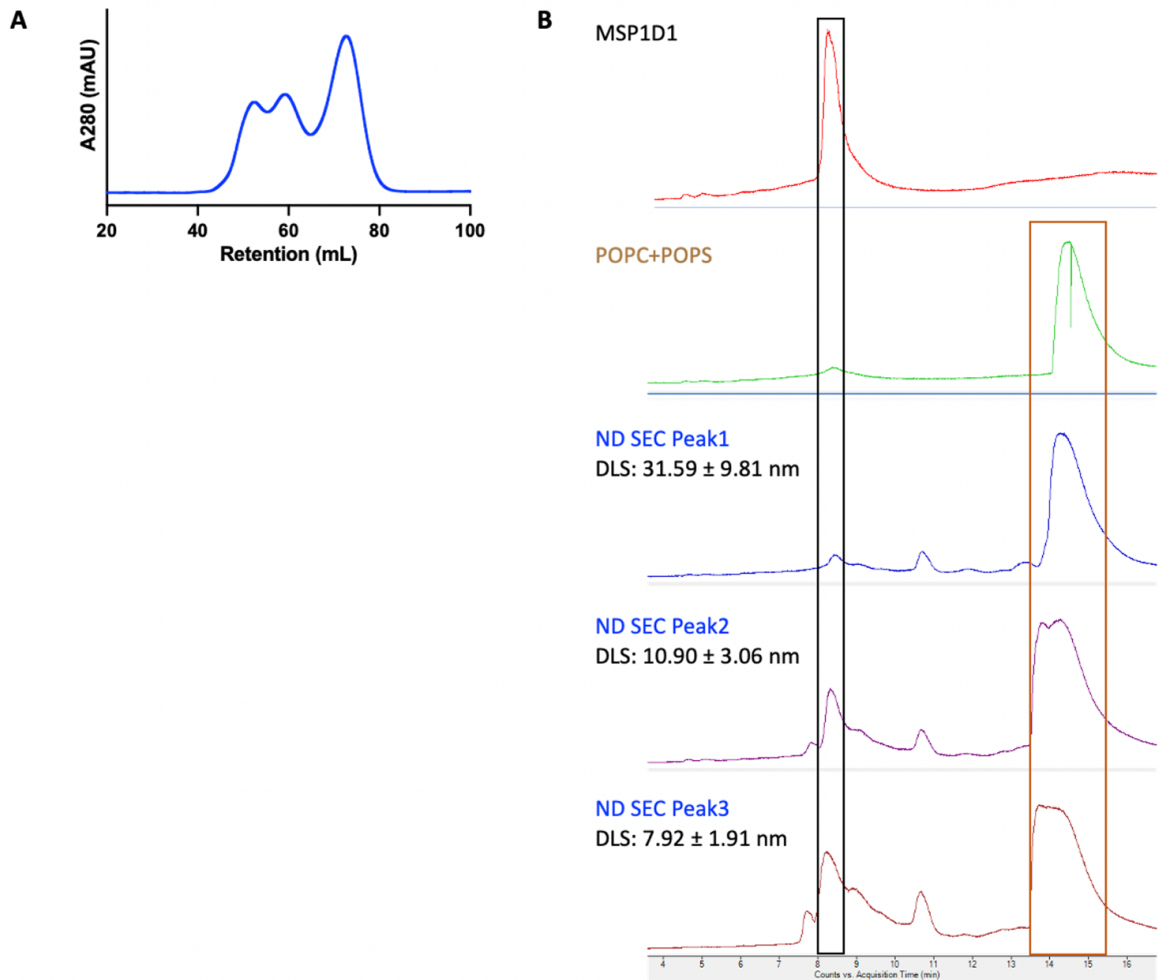
Figure 3.10. Size exclusion chromatography and liquid chromatography–mass spectrometry analysis of MSP1D1 nanodisc assembly. (A) SEC trace resolved three species from the nanodisc assembly mixture. (B) Liquid chromatography of the three species was compared to MSP1D1 and POPC/POPS-lipid-mixture standards. The mass of all five samples was confirmed with QTOF mass spectrometry. The LC signal in the black box corresponded to the MSP1D1 mass and the signal in the brown box corresponded to the POPC/POPS mass. The inserted values are DLS measurement results of the monodispersed species. The sizes of the three species were 31.6 ± 9.8 nm, 10.9 ± 3.1 nm, and 7.9 ± 1.9 nm.

Table 3.1. The TM-JM protein of interest

Protein	Sequence (N → C) TM-JM	Expected structure
WT	Y-KIPSIATGMV**G**$_{648}$ALLLLLVVALGIGLFMRRRHIVR-KRTLRRLLQERELVE	TM: smaller cross-angle JM: EGF-type
G628F	Y-KIPSIATGMV**F**ALLLLLVVALGIGLFMRRRHIVR-KRTLRRLLQERELVE	TM: smaller cross-angle JM: EGF-type
G628V	Y-KIPSIATGMV**V**ALLLLLVVALGIGLFMRRRHIVR-KRTLRRLLQERELVE	TM: larger cross-angle JM: TGF-α-type
G628A	Y-KIPSIATGMV**A**ALLLLLVVALGIGLFMRRRHIVR-KRTLRRLLQERELVE	TM: smaller cross-angle JM: EGF-type

Chapter 4. Summary and analysis of participated projects, partially completed projects, and future directions

Disclosure and authorship

This chapter contains material adapted from a manuscript submitted to the peer-reviewed journal *eLife* for review:

"Coiled coil control of growth factor and inhibitor-dependent EGFR trafficking and degradation", Mozumdar, D., Chang, S. H.-H., Quach, K., Doerner, A., Zhang, X., Schepartz, A.

This chapter describes experiment initiated by Dr. Deepto Mozumdar on investigating the effect of JM coiled coil conformation on EGFR trafficking. I had significant contributions in the project and led to its submission to the peer-reviewed journal eLife currently under review. The aim of the second ongoing project is to investigate the effect of JM coiled coil on the interactome of EGFR proximity labeling and mass spectrometry. This work was performed with Dr. Deepto Mozumdar.

Chapter 4. Summary and analysis of participated projects, partially completed projects, and future directions

4.1 The effect of the JM-A coiled coil structure on EGFR trafficking and degradation
Previous reports have described the coupling between JM structure and the ECD growth factor identity and coupled the coiled coil conformation to the EGF-type and TGF-α-type downstream effect.[11,13–15] Nonetheless, a detailed understanding of the effects the JM coiled coil has on EGFR biology is desired. Using JM-switching mutation to control the JM coiled coil, this section describes the effect of the JM structure on the EGFR signaling pathway in terms of receptor trafficking and receptor degradation.

JM coiled coil controls the pathway of receptor trafficking: Previously described JM-switching JM mutations (E661R & KRAA) and the JM-switching TM mutations (G628F & G628V) were used to control the JM coiled coil in CHO-K1 cells transfected with defined EGFR. Confocal microscopy was used to observe the trafficking of FLAG-tagged EGFR stained with fluorophore-conjugated antibodies. The pathway of EGFR traffics to is defined as follows: The degradative pathway was defined as EGFR trafficking into the late endosome labeled by Rab7 biomarker and subsequently degraded in the lysosome. The recycling pathway was defined as EGFR trafficking into the recycling endosome marked by Rab11[15] and eventually recycled back to the plasma membrane (**Figure 4.1**). Results showed that the JM coiled coil structure was both necessary and sufficient to direct the pathway of EGFR trafficking. At 40 mins time point after EGF- or TGF-α-induced endocytosis, the WT and G628A EGFR co-localization was growth factor-dependent while the JM-switching JM mutations (E661R & KRAA) (**Figure 4.2**) and the JM-switching TM mutations (G628F & G628V) (**Figure 4.3**) were not. When stimulated with EGF, WT and G628A EGFR co-localized preferentially with Rab7 and not Rab11, when stimulated with TGF-α, WT and G628A EGFR co-localized preferentially with Rab11 and not Rab7. In contrast, E661R EGFR and G628F EGFR that forms the EGF-type coiled coil co-localized preferentially with Rab7 whether stimulated with EGF or TGF-α and not with Rab11. On the other hand, KRAA EGFR and G628V EGFR that forms TGF-α-type coiled coil co-localized preferentially with Rab11 whether stimulated with EGF or TGF-α and not with Rab7. To sum up, when JM coiled coil conformation was controlled by mutations, the trafficking pattern was directed by the JM coiled coil status: when JM exhibited the EGF-type coiled coil conformation, EGFR trafficked along the degradative pathway regardless of growth factor identity of either EGF or TGF-α, whereas when JM exhibited the TGF-α-type coiled coil conformation, EGFR trafficked along the recycling pathway regardless of growth factor identity of either EGF or TGF-α.

Coiled coil control of EGFR degradation: The effect on endocytic trafficking with the JM-structure-controlling mutants was presumed to also affect in the lifetime of EGFR. Immunoblotting experiments examining EGFR abundancy at 90 mins after EGF or TGF-α stimulation was performed to examine EGFR lifetime and degradation (**Figure 4.4**). In the case of WT EGFR and conservative mutation G628A, the lifetime of EGFR depends on growth factor identity in the expected manner.[11,15] Following EGF stimulation, WT and G628A EGFR levels decrease rapidly, and the fraction of intact EGFR detected after 90 mins was low (41-46%), whereas the fraction of intact EGFR detected after 90 mins was high when cells were stimulated

with TGF-α (92%). By contrast, the JM-switching TM mutants affect EGFR degradation in a growth-factor-independent manner. G628F EGFR degraded rapidly regardless of whether the receptor was activated with EGF or TGF-α 90 min following EGF or TGF-α treatment. G628V EGFR degraded slowly following treatment with EGF or TGF-α. Immunoblotting experiments of EGFR abundance at 90 mins pre-incubated with the lysosomal inhibitor chloroquine[150] or the proteasomal inhibitor lactacystin[151] confirmed that the EGFR degradation occurred through the lysosomal degradation pathway since the lysosomal inhibitor chloroquine prevented EGFR degradation (**Figure 4.4**).

In summary, single-point TM mutations and the long-range effects on JM conformation was necessary and sufficient to dictate the pathway of intracellular trafficking and degradation of EGFR.

4.2 Efforts toward understanding the effect of JM structure on the EGFR interactome using proximity labeling and mass spectrometry proteomics

In chapter 1, studies were reviewed to demonstrate the JM domain as a hotspot for cytosolic interactions from cytosolic proteins[29,58–75] to the inner leaflet of the plasma membrane.[29,56,57] We hypothesized that differences in EGFR biology may result from altered interactome recruited by alternative JM coiled coil structure (**Figure 4.5**). To probe the differences in the interactome, mass spectrometric methods have been previously used to characterize the interacting partners of EGFR following activation with growth factors EGF and TGF-α.[15,152,153] Alice Ting's group has developed a proximity labeling method engineering ascorbate peroxidase APEX2 to proteins of interest that biotinylates interacting protein partners *in cellulo.*[154–157] Here we propose APEX2-based proximity labeling experiments to identify the interacting partners of WT, G628F, and G628V EGFR that control the JM-A coiled coil into the EGF-type or TGF-α-type structure respectively.

Preliminary results: Peroxidase APEX2 was engineered at the C-terminal of the EGFR of variants (**Figure 4.5.A**): WT, G628A, G628F, G628V, kinase-inactive K721M,[27,158,159] TKI-resistant L834R/T766M EGFR (or the double-mutant, DM EGFR),[160] and the peroxidase-inactive EGFR-D208N-APEX2.[161] The cloned constructs were transfected into CHO-K1 cells, and the expressions were evaluated with immunoblotting experiments (**Figure 4.6.B**). We observed that all FLAG-tagged variants were expressed in CHO-K1 cells. The EGFR kinase activity was examined with immunoblotting experiments by comparing the C-tail tyrosine residue (Y1045 and Y1068) phosphorylation upon growth factor treatment. The immunoblotting analysis compared the WT EGFR, the kinase-dead K721M EGFR, and the engineered EGFR-APEX2. The K721M was the negative control (**Figure 4.6.C–F**). WT EGFR was robustly phosphorylated at both Y1045 and Y1068 following the treatment with either EGF or TGF-α, and not phosphorylated in the absence of growth factor. EGFR-APEX2 was phosphorylated at both Y1045 and Y1068 following growth factor treatment at levels comparable to WT EGFR. No auto-phosphorylation activity was observed at either tyrosine residues in the K721M EGFR in the absence and presence of EGF or TGF-α.

Secondly, we evaluated the peroxidase activity of EGFR-APEX2 using a fluorescence-based assay using Amplex red. The activity of the peroxidase catalyzes the non-fluorescent Amplex red into fluorescent Resorufin in the presence of H_2O_2 (**Figure 4.6.G**).[154] The temporal changes in

fluorescence provides a robust and instantaneous readout of the peroxidase activity of APEX2 to evaluate the APEX2 activity in the cloned constructs (**Figure 4.6.H**). Both APEX2 and EGFR-APEX2 peroxidases were active, even though the activity of EGFR-APEX2 was slightly weaker and slower compared to APEX2. No detectable peroxidase activity was observed with the negative control D208N APEX2. Even though slightly reduced, the enzymatic activity of APEX2 in the fusion construct was still significantly retained. The APEX2 enzymatic activity is critical for the subsequent proximity labeling experiments. Thus, it may be worthwhile to investigate and optimize peroxidase activity of the engineered EGFR APEX2. One direction is studying the effect of the construct on APEX2 activity by varying the linker length between EGFR and APEX2 or changing the APEX2 position in the construct.

Next, the cellular localization of EGFR variants was evaluated with immunofluorescence imaging to emsure that the EGFR-APEX2 constructs correctly localizes at the plasma membrane. Confocal microscopy was used to observe the FLAG-tagged EGFR stained with fluorophore-conjugated antibody (**Figure 4.7**). The immunofluorescence images showed that the engineered constructs were expressed and localized correctly on the plasma membrane of the CHO-K1 cells.

Finally, *in cellulo* biotinylation reactions were examined with immunoblotting experiments before submitting for mass spectrometry analysis. The method for characterizing the *in cellulo* biotinylation of the APEX2 fusion construct and the streptavidin pull-down experiments were described previously.[155] Cells expressing the EGFR-APEX2 constructs were treated with biotin phenol prior to stimulating with growth factors EGF or TGF-α. Cells were treated with H_2O_2 to initiate the biotinylation reaction at specific time points after growth factor stimulation (0–8 mins: to identify early interactors; 40–90 mins: to identify later interactors). Cells were lysed and the cleared lysate was analyzed with Western blotting using streptavidin-HRP antibody visualized using Clarity Western ECL reagents (**Figure 4.8.A**). In the negative control (D208N-APEX and APEX2 lacking either BP or H_2O_2), only the endogenous biotinylated proteins (130, 75, and 72 kDa) were observed. For APEX2 and EGFR-APEX2 (with and without growth factor treatment), strips of biotinylated proteins were separated and visualized with Western blotting. The EGFR-APEX2 resulted in biotinylation profiles different from that of APEX2 (**Figure 4.8.A**). Biotinylated proteins in cell lysates were enriched using streptavidin beads. Bands of biotinylated proteins were resolved for EGFR-APEX2 catalyzed *in cellulo* biotinylation reaction samples (**Figure 4.8.B**). These were promising results to lay out the groundworks leading up to mass spectrometry proteomics studies to map the interactome of EGFR at short and long time points after growth factor stimulation and explore the effect of JM coiled coil using JM-switching mutants.

4.3. Future directions for the JM coiled coil structural studies

In chapter 3, the work to prepare JM coiled coil structural studies using TM-JM protein and membrane mimics has faced challenges in sample stability and protein homogeneity. Although these are not trivial challenges, some future directions can be outlined.

For DMPC/DHPC bicelle-TM-JM samples, optimization of the preparation process could be explored via optimizing parameters such as the q value [48,140] and the lipid concentration.[140,142] On the other hand, DMPC and DHPC have relatively high phase transition temperatures (24 °C[118] and 49 °C[162], respectively), raising the question of whether there was efficient mixing during the bicelle preparation procedure to form properly aligned DMPC/DHPC bicelles. Thus, the steps and

conditions in the bicelle preparation protocol are potentially optimizable. One can also explore other lipid options seeking out lipid with lower phase transition temperatures.[113] However, the optimal q value and the lipid concentration will be altered with different lipid systems. DMPC/DHPC bicelles remain the best understood and used bicelle system. One study found that doping cholesterol sulfate in DMPC/DHPC bicelles widen the temperature range for optimal alignment (from 32–36 °C for DMPC/DHPC-only bicelles to 25–50 °C for cholesterol-sulfate-doped bicelles),[163] demonstrating another direction to optimize bicelles. Additionally, the correct insertion geometry of the TM-JM protein into the bicelle can be examined with oriented circular dichroism (OCD) to distinguish the state of the membrane-bound α-helical peptide between membrane-surface-bound, obliquely tilted, and fully inserted transmembrane orientation using characteristic OCD line shape around 208 nm.[164]

In chapter 3, I established the first ever usage of nanodisc in our research group. The characterizations of empty MSP1D1 nanodisc laid the groundwork for succeeding nanodisc-TM-JM preparation and characterization. The analysis for nanodisc-TM-JM with SEC and LC-MS characterization will be aided by existing characterizations of empty MSP1D1 nanodisc. The shape, size, and dynamics of the nanodiscs can be characterized by small-angle X-ray scattering (SAXS).[120,165] The insertion of TM-JM protein in the nanodisc can be characterized using hydrogen-deuterium exchange mass spectrometry (HDX-MS) discerning the solvent-exposed residues from the transmembrane residues by the rate of deuterium exchange in a deuterated buffer.[122]

4.4. Materials and Methods

Materials. Antibodies. Goat polyclonal anti-rabbit, horseradish peroxidase (HRP)-conjugated (#7074), goat polyclonal anti-mouse, HRP-conjugated (#7076), rabbit monoclonal anti-vinculin (#13901), rabbit monoclonal anti-Rab7 (D95F2) XP (#9367), Rab11 (D4F5) XP Rabbit mAb (#5589), anti-mouse IgG (H+L) and F(ab')2 fragment Alexa Fluor 555-conjugate (#4409) were products of Cell Signaling Technologies (CST). Mouse monoclonal (M2) anti-FLAG (#F1804) was a product of Sigma-Aldrich. Goat anti-mouse IgG (H+L) Alexa Fluor 488 (#A11008) was a product of ThermoFisher Scientific. Streptavidin-HRP (#3999) was a product of Cell Signaling Technology.

Chemicals and recombinant proteins. F-12K medium (#10-025-CV), Dulbecco's phosphate buffered saline (DPBS) (#14190), fetal bovine serum (FBS)–heat inactivated (#11082147), penicillin/streptomycin (#1514012), non-enzymatic cell dissociation solution (#13151014), Hoechst 33342, iBlot PVDF membranes (#IB401031) were products of ThermoFisher Scientific. FugeneHD transfection reagent (E2311) was a product of Promega. TransIT-CHO transfection kit was a product of Mirus Bio. Fetal bovine serum (FBS)–heat inactivated (#F4135), bovine serum albumin (#9048-46-8), and fibronectin (#F1141) were products of Sigma-Aldrich. cOmplete, mini protease inhibitor tablets (#11836170001), and PhosSTOP phosphatase inhibitor cocktail tablets (#04906837001) were products of Roche Life Science. Recombinant human EGF protein (#236-EG) and recombinant human TGF-a protein (#293-A) were products of R&D Systems. Mini-PROTEAN® TGXTM Precast Gels (10% polyacrylamide) (#456-1036), and Western ECL reagents (#1705060) were products of Bio-Rad Laboratories. Lactacystin, proteasome inhibitor (#ab141411), and chloroquine diphosphate, apoptosis and autophagy inhibitor (#ab142116), were products of AbCam. Biotin phenol was a product of Fisher Scientific. Pierce™ 660nm protein

assay reagent was a product of ThermoFisher Scientific. Amplex red assay kit was a product of Life Technologies.

Cell culture. CHO-K1 cells (ATCC) were cultured in F12K Medium supplemented with 10% FBS and Pen-Strep (100 I.U./mL penicillin and 100 mg/mL streptomycin) at 37 °C in a CO_2/air (5%/95%) incubator (NuAire). Cells were transfected using the TransIT-CHO Transfection Kit or FugeneHD, following instructions and protocols provided by the manufacturers. Cell densities for all mammalian cell lines were determined with a Cellometer Auto T4 automated counter.

Cloning and mutagenesis. All EGFR DNA variants were cloned from a pcDNA3.1 plasmid, generously donated by the Kuriyan Group (University of California, Berkeley), containing the sequence of the full-length EGFR with an N-terminal FLAG tag. Mutations were introduced into the EGFR sequences using Quikchange Lightning site-directed mutagenesis kit (Agilent Technologies) following the manufacturer's instructions, with primers purchased from Integrated DNA Technologies. All DNA variants were amplified with XL-10 Gold Ultracompetent cells (Agilent Technologies).

Immunofluorescent labeling, confocal microscopy, and image analysis. Immunofluorescent labeling and confocal microscopy to assess the localization of EGFR variants expressed in CHO-K1 cells were carried out as described previously[15] with slight modifications. CHO-K1 cells expressing FLAG-tagged EGFR variants were serum starved overnight (~12 hrs) and subsequently incubated without or with 100 ng/mL of EGF (16.7 nM) or TGF-α (16.7 nM) for 1 hr at 4 °C for growth factor binding. Cells were then washed with DPBS and incubated with serum-free media at 37 °C for 40 mins to allow endocytosis. Cells were then fixed using fixing buffer (4% paraformaldehyde in DPBS) for 15 mins at room temperature. Cells were washed with DPBS and incubated with blocking buffer (5% normal goat serum (CST), 0.3% Triton X-100 in DPBS) for 1 hr at 37 °C. Cells were then labeled with indicated primary antibodies overnight (~12 hrs) at 4 °C (mouse M2 anti-FLAG, rabbit anti-Rab7, or rabbit anti-Rab11 with 1:1000 dilution in antibody dilution buffer (1% BSA, 0.3 % Triton X-100 in DPBS)). Cells were then washed three times with DPBS and subsequently incubated with secondary antibodies (Goat anti-rabbit Alexa Fluor 488 or goat anti-mouse Alexa Fluor 555 with 1:500 dilution in antibody dilution buffer) for ~2 hrs at room temperature. Cells were then washed twice with DPBS and nuclear stained with Hoescht 33342 (1.62 mM in DPBS) for 2 mins at room temperature. Cells were then washed twice with DPBS and stored in DPBS at 4 °C, prior to imaging. Laser-scanning confocal microscopy experiments of labeled immunofluorescent samples were performed at room temperature on an inverted Zeiss LSM 880 laser-scanning confocal microscope equipped with a Plan-Apochromat ×63/1.4 numerical aperture oil immersion lens and a diode 405 nm laser, an Argon 458, 488, 514 nm laser, a diode-pumped solid-state 561 nm laser and a 633 nm HeNe laser with standard settings. DAPI, Alexa Fluor 488, and Alexa Fluor 555 dyes were excited with 405-, 488-, and 546-nm laser lines. The pinhole size was set to 1 airy unit. Images were acquired at a nuclear section with fixed thresholds. Image acquisition was performed with ZEN software (Carl Zeiss). Raw images were exported as .lsm files. Images were analyzed using ImageJ software.[166] Colocalization of EGFR with endocytic biomarker (Rab7 or Rab11) was evaluated as Manders' Colocalization Coefficient (MCC)[167] which represents the sum of intensities of green pixels (due to Rab7 or Rab11) that also contain red (due to FLAG-tagged EGFR) divided by the total sum of green intensities. Colocalization was evaluated using JACoP (Just Another Colocalization Plugin)[168] in ImageJ. MCC values for each condition obtained from multiple cells collected over at least 2 biological

replicates were pooled and represented as Mean with S.E.M using GraphPad Prism 8.4.3. For EGFR-APEX2 construct localization experiments, the procedure was similar to that described above except that Triton X-100 was omitted in the blocking buffer and antibody dilution buffer to avoid solubilizing the plasma membrane. The staining process only included primary antibody mouse M2 anti-FLAG with secondary antibody Alexa Fluor 555-conjugated goat anti-mouse and the nuclear-stain Hoescht 33342. Laser-scanning confocal microscopy experiments were performed at room temperature on an inverted Leica STELLARIS 8 microscope (Leica Microsystems) equipped with a Leica DMi8 CS scanhead, a HC Plan-Apo 63x/1.4NA water immersion objective Confocal imaging was carried out using either HyD S or HyD X detectors in analog or digital mode.

Western blot analysis of EGFR expression and autophosphorylation. Western blot analysis of EGFR expression in transfected CHO-K1 cells was described previously[37,55] with slight modifications. CHO-K1 cells expressing FLAG-tagged EGFR variants were serum starved overnight (~12 hrs) and subsequently incubated without or with 100 ng/mL of EGF (16.7 nM) or TGF-α (16.7 nM) for 1 hr at 4 °C for growth factor binding. Cells were then washed with DPBS and incubated with serum-free media at 37 °C for 0–90 mins and lysed in 100 mL of lysis buffer (50 mM Tris, 150 mM NaCl, 1 mM EDTA, 1 mM NaF, 1% Triton X-100, pH 7.5, 1x cOmplete protease inhibitor cocktail, 1x PhosStop). Clarified cell lysates were subjected to reducing SDS-PAGE electrophoresis and transferred to immuno-blot PVDF membranes. Membranes were blocked with 5% milk in TBST buffer (50 mM Tris, 150 mM NaCl, 0.1% Tween 20, pH 7.4) for 1 hr followed by overnight incubation at 4 °C of indicated primary (rabbit or mouse) antibodies. Blots were washed with TBST buffer and incubated with either anti-rabbit or anti-mouse goat horseradish peroxidase conjugate secondary antibodies for 1 hr at room temperature, then washed with TBST buffer. Blots were then visualized using Clarity Western ECL reagents on a ChemiDoc instrument (Bio-Rad), and intensities of immuno-stained bands were measured with ImageJ. FLAG signals (total EGFR) were normalized to the vinculin loading control and normalized signal for the condition without any growth factor treatment. For all experiments with proteasomal or lysosomal inhibitors, the experiments were carried out with CHO-K1 cells as described above with the additional pretreatment with 10 μM Lactacystin or 100 μM Chloroquine for 1 hr at 37°C prior to growth factor treatment. The quantification of Western blot data sourced from at least 2 biological replicates and represented as Mean with S.E.M using GraphPad Prism version 8.4.3

Amplex red assay to detect peroxidase activity. Cellular lysates from CHO-K1 cells expressing FLAG-tagged variants were prepared as described for western blot analyses. The total protein concentrations in the clarified cell lysates were quantified using Pierce™ 660nm protein assay reagent. According to the Amplex red assay kit instructions, 20 μg of protein in the sample was diluted in 100 μL of DPBS pH 7.4 and was set up in 96-Well 360-μL clear flat bottom assay microplate, non-treated black polystyrene (Corning). A 2x reaction mixture was prepared by mixing 25 μL of 10 mM Amplex UltraRed stock (to a final concentration of 50 μM), 11.4 uL of 3% H_2O_2 (to a final concentration of 1 mM), and 2.5 mL of DPBS pH 7.4. Using a multichannel pipette, 100 μL of the reaction mixture was added to a 100 μL cell lysate solution and the fluorescence at 530/590 nm ex/em was recorded at regular intervals of 5 mins for 1 hr on a Synergy HTX microplate plate reader (BioTek Instruments). The clarified cell lysates from CHO-K1 cells were expressing APEX2, EGFR-APEX2 (with and without growth factor treatment stimulation), and negative controls D208N-APEX2 and DPBS.
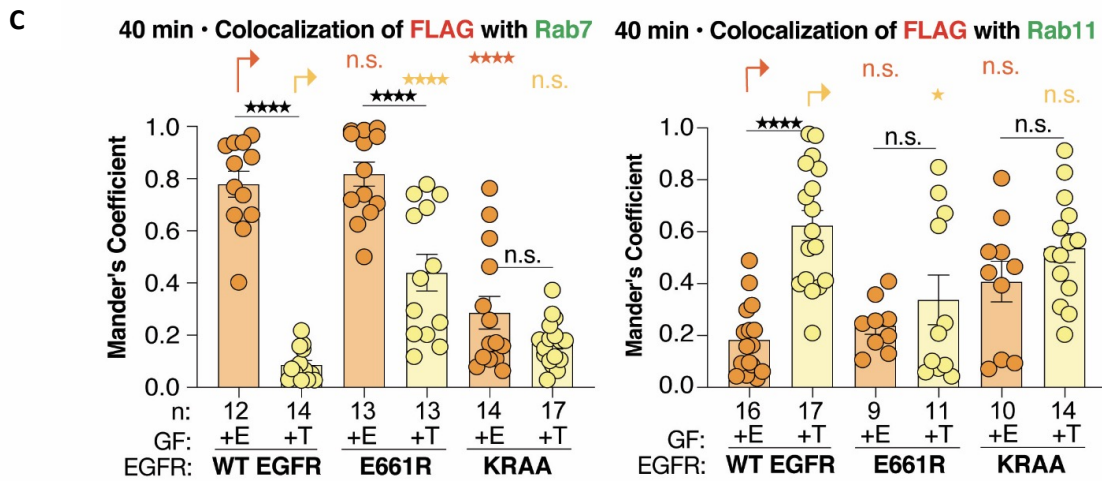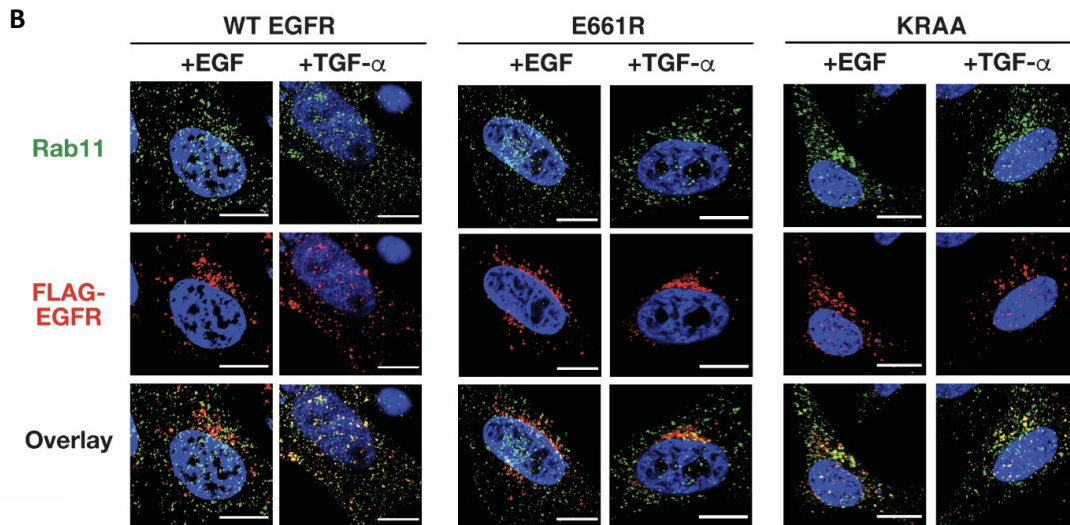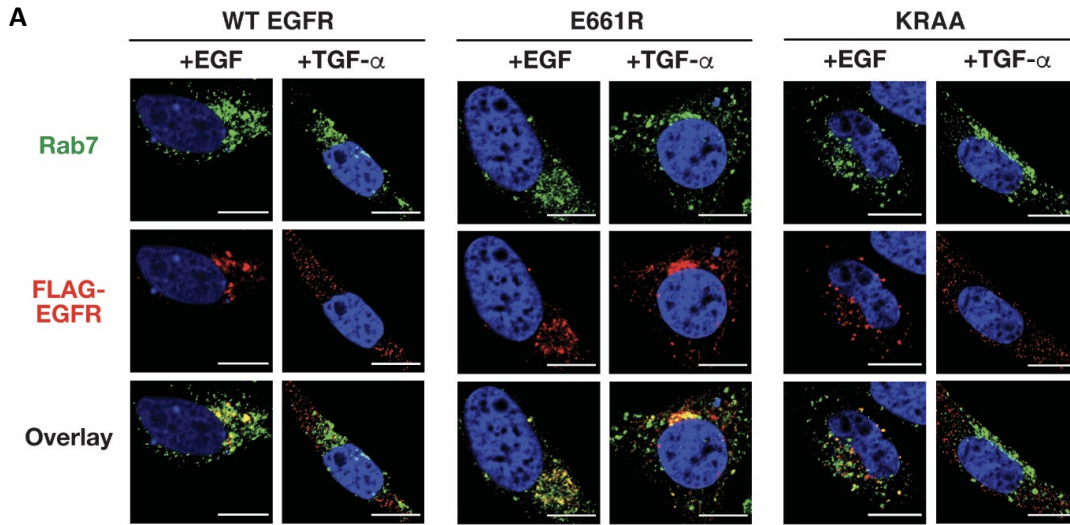
Characterization of *in cellulo* biotinylation reaction and streptavidin pull-down enrichment. The described method was slightly modified from a reported protocol.[155] Cells were plated into six-well plates, each well for a condition. Cells were transfected with APEX2, D208N-APEX2, or EGFR-APEX2 constructs using the TransIT-CHO Transfection Kit. Cells were incubated in 500 μM biotin phenol (BP) in a serum-free medium for 30 mins at 37 °C, then were treated with serum-free media containing BP and with and without growth factors on ice for 15 mins. After growth factor stimulation, media were aspirated, cells were rinsed with ice-cold DPBS, and cells were incubated in a pre-warmed serum-free medium containing 500 μM biotin phenol (BP) for 1 min and 40 mins at 37 °C. Fresh 2x stock of labeling solution 2 mM H_2O_2 was made in DPBS and added in a 1:1 amount directly to the BP solution to achieve a final concentration of 1 mM. Cells were incubated at room temperature for 1 min and then quickly aspirated. Cells were washed three times with quencher solution (10 mM sodium ascorbate, 5 mM Trolox and 10 mM sodium azide solution in DPBS. Quencher solution was made on the same day immediately before use.). Cells were lysed by gentle pipetting in RIPA lysis buffer (50 mM Tris, 150 mM NaCl, 0.1% (wt/vol) SDS, 0.5% (wt/vol) sodium deoxycholate and 1% (vol/vol) Triton X-100, pH 7.5) supplemented with cOmplete™ EDTA-free protease inhibitor cocktail, 1 mM PMSF and quenchers (10 mM sodium azide, 10 mM sodium ascorbate and 5 mM Trolox). Suspended cell samples were left on ice for ~2 mins and clarified by centrifuging at 14,100 g for 15 mins at 4 °C. Clarified cell lysates were subjected to Western blot analysis using reducing SDS-PAGE electrophoresis and transferred to immuno-blot PVDF membranes. Membranes were blocked with 3% (wt/vol) BSA in TBST buffer overnight at 4 °C. The membrane was treated with 10 ml of 0.3 μg/ml streptavidin-HRP in 3% BSA in TBST at room temperature for 1 hr and washed with TBST four times for 5 mins each time. Blots were then visualized using Clarity Western ECL reagents on a ChemiDoc instrument (Bio-Rad). Streptavidin pull-down of biotinylated proteins was done by preparing fresh biotinylated cell lysate samples as described above. The amount of protein in each clarified lysate was quantified by using the Pierce™ 660nm protein assay reagent. 360 μg (~90 μL) of each cell lysate sample was incubated with 30 μL of streptavidin magnetic beads for 1 hr at room temperature on a rotator. Additional RIPA buffer was added to facilitate rotation (< 500 μL). The beads were pelleted using a magnetic rack. The supernatant was collected and labeled 'flow-through'. The beads were washed: twice with RIPA lysis buffer, once with 1 M KCl, once with 0.1 M Na_2CO_3, once with 2 M urea in 10 mM Tris-HCl, pH 8.0, and twice with RIPA lysis buffer. Biotinylated proteins were eluted from the beads by boiling each sample in 30 μL of 3x protein loading buffer supplemented with 2 mM biotin and 20 mM DTT for 10 mins. The flow-throughs and elutes were subjected to the Western blot analysis described above.
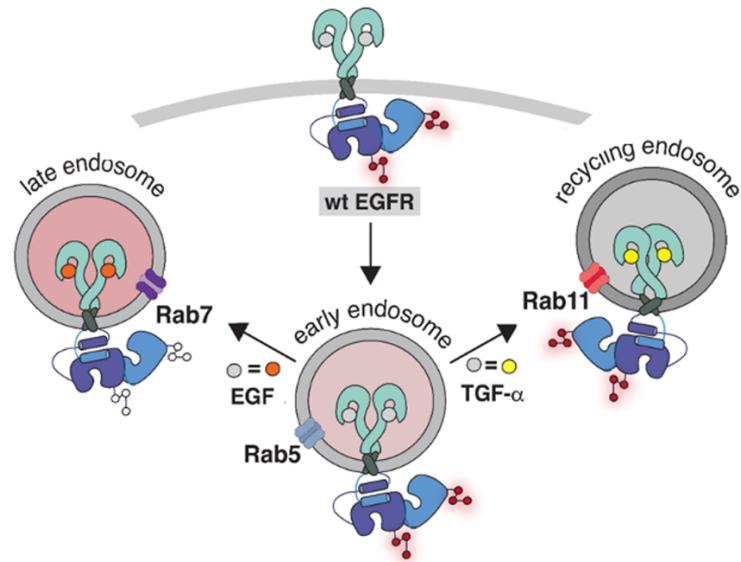
Figure 4.1. The trafficking pathway of EGFR following growth factor stimulation. For WT EGFR, when EGFR is stimulated with EGF, the receptor traffics the late endosome following endocytosis, subsequently degraded in the lysosome. When stimulated with TGF-α, the receptor traffics the recycling endosome following endocytosis, subsequently recycled to the plasma membrane. The late endosome is labeled with Rab7 as its biomarker and the recycling endosome is labeled with Rab11 as its biomarker.[15]

A

	WT EGFR		E661R		KRAA	
	+EGF	+TGF-α	+EGF	+TGF-α	+EGF	+TGF-α

Rab7

FLAG-EGFR

Overlay

B

	WT EGFR		E661R		KRAA	
	+EGF	+TGF-α	+EGF	+TGF-α	+EGF	+TGF-α

Rab11

FLAG-EGFR

Overlay

C

40 min · Colocalization of FLAG with Rab7

40 min · Colocalization of FLAG with Rab11

Figure 4.2. The EGFR trafficking in CHO-K1 cells was influenced by JM coiled coil conformation controlled by JM mutations E661R and KRAA. Confocal microscopy images of CHO-K1 cells expressing FLAG-tagged WT, E661R, or KRAA EGFR (false-colored red), immuno-labeled with (A) Rab7 (false-colored green) as a biomarker for degradative endosomes or (B) Rab11 (false-colored green) as a marker for recycling endosomes, 40 mins after stimulation with EGF (E) or TGF-α (T). Scale bars = 10 μm. (C) Bar plots illustrating the Manders' colocalization coefficient (MCC) of FLAG-tagged WT EGFR, E661R, and KRAA EGFR with either Rab7 or Rab11 40 mins after stimulation with EGF or TGF-α. n = # of cells. Error bars = S.E.M. ****$p<0.0001$, ***$p<0.001$, **$p<0.01$, *$p<0.1$, n.s. not significant, from one-way ANOVA with Tukey's multiple comparison test. Figure adapted from Ref. [169]

A

	WT EGFR	G628A	G628F	G628V
	+EGF / +TGF-α	+EGF / +TGF-α	+EGF / +TGF-α	+EGF / +TGF-α

Rab7

FLAG-EGFR

Overlay

B

	WT EGFR	G628A	G628F	G628V
	+EGF / +TGF-α	+EGF / +TGF-α	+EGF / +TGF-α	+EGF / +TGF-α

Rab11

FLAG-EGFR

Overlay

C

40 min • Colocalization of FLAG with Rab7

n.s. n.s. ****
n.s. n.s. **** n.s.

Mander's Coefficient

**** **** n.s. ★

n:	50	62	24	17	16	18	26	14
GF:	+E	+T	+E	+T	+E	+T	+E	+T
EGFR:	WT EGFR		G628A		G628F		G628V	

40 min • Colocalization of FLAG with Rab11

n.s. n.s. ****
n.s. **** n.s.

Mander's Coefficient

**** **** n.s. n.s.

| n:	16	21	14	12	16	12	18	17
GF:	+E	+T	+E	+T	+E	+T	+E	+T
EGFR:	WT EGFR		G628A		G628F		G628V	

70
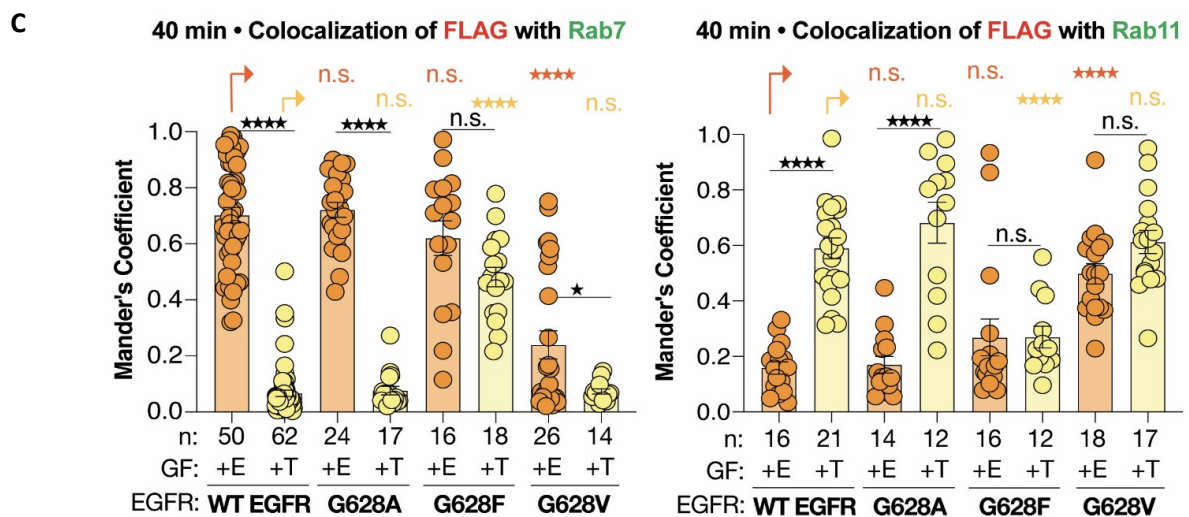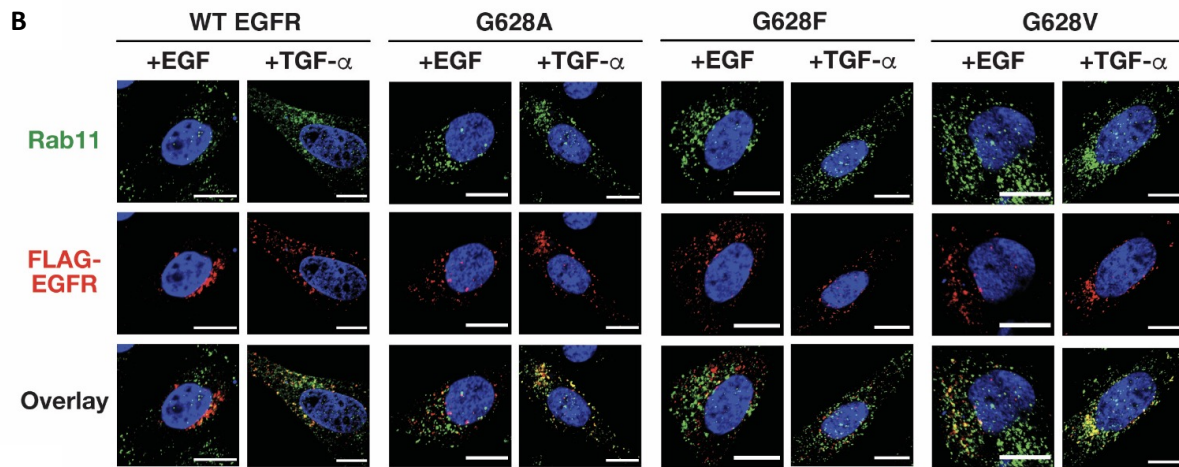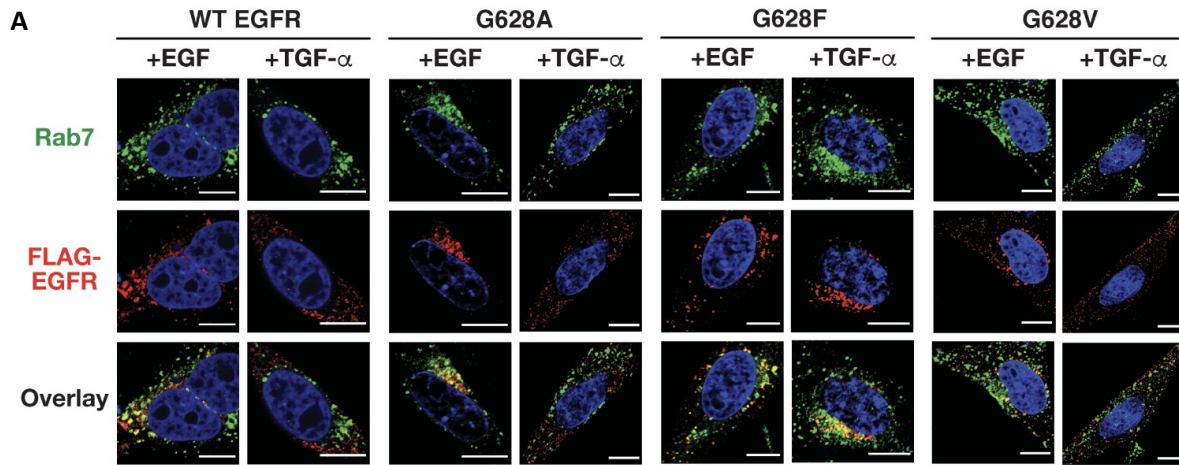
Figure 4.3. The EGFR trafficking in CHO-K1 cells was influenced by JM coiled coil conformation controlled by TM mutations G628F and G628V. Confocal microscopy images of CHO-K1 cells expressing FLAG-tagged G628A, G628F, and G628V EGFR (false-colored red) and immuno-labeled with (A) Rab7 (false-colored green) as a marker for degradative endosomes or (B) Rab11 (false-colored green) as a marker for recycling endosomes, 40 mins after stimulation with EGF (E) or TGF-α (T). Scale bars = 10 µm. (C) Bar Plots illustrating Manders' colocalization coefficient (MCC) of FLAG-tagged G628A, G628F, and G628V EGFR with either Rab7 or Rab11-GFP 40 mins after stimulation with EGF or TGF-α (16.7 nM). n = # of cells. Error bars = S.E.M. ****$p<0.0001$, ***$p<0.001$, **$p<0.01$, *$p<0.1$, n.s. not significant from one-way ANOVA with Tukey's multiple comparison test. Figure adapted from Ref. [169]
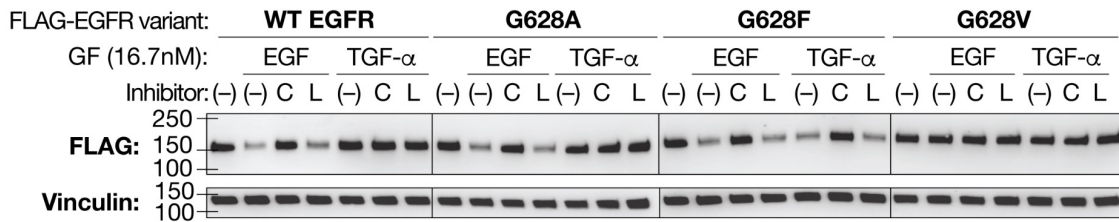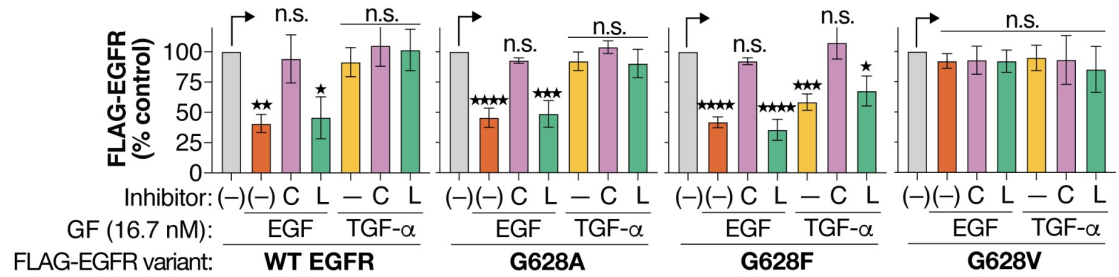
Figure 4.4. Coiled coil control of EGFR degradation. (A) Western blots illustrating the level of FLAG-tagged WT, G628A, G628F, and G628V EGFR detected in CHO-K1 cells 90 mins after stimulation with or without EGF or TGF-α (16.7 nM) and without or with pre-incubation with the lysosomal inhibitor chloroquine, C (100 μM) or the proteasomal inhibitor lactacystin, L (10 μM) for 1 hr at 37 °C. (B) Plot illustrating the normalized percent of intact FLAG-tagged WT, G628A, G628F, and G628V EGFR. Vinculin was used as the loading control. Error bars = S.E.M.. ****$p<0.0001$, ***$p<0.001$, **$p<0.01$, *$p<0.1$, n.s. not significant from one-way ANOVA with Dunnett's multiple comparison test. Figure adapted from Ref. [169]
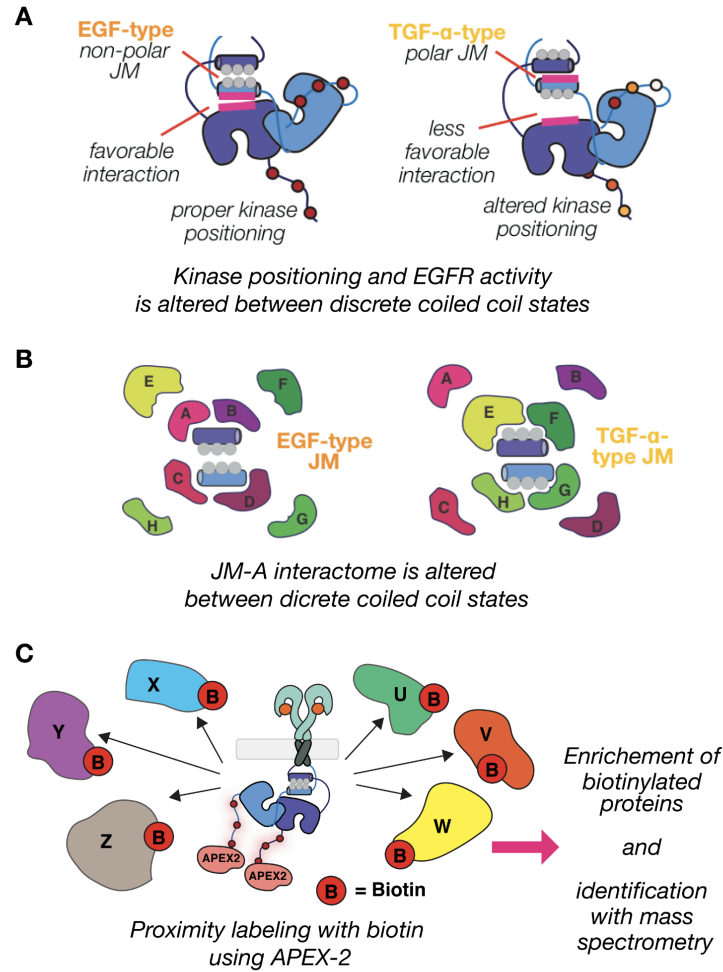
Figure 4.5. Mechanism of JM coiled coil control of EGFR biology. The alternate JM-A coiled coil structures can regulate EGFR biology by two possible mechanisms. (A) The two JM-A structures can alter the JM-A surface that interacts with the EGFR kinase thereby altering kinase positioning and activity thereby affecting the recruitment of diverse intracellular adaptors and down regulatory proteins. (B) Alternately, the different JM-A coiled coil surfaces exposed alter the interactome of EGFR. (C) The coiled coil dependent interactome of EGFR investigated using proximity labeling methodology followed by mass spectrometry proteomics analysis. Figure adapted from Ref. [78]
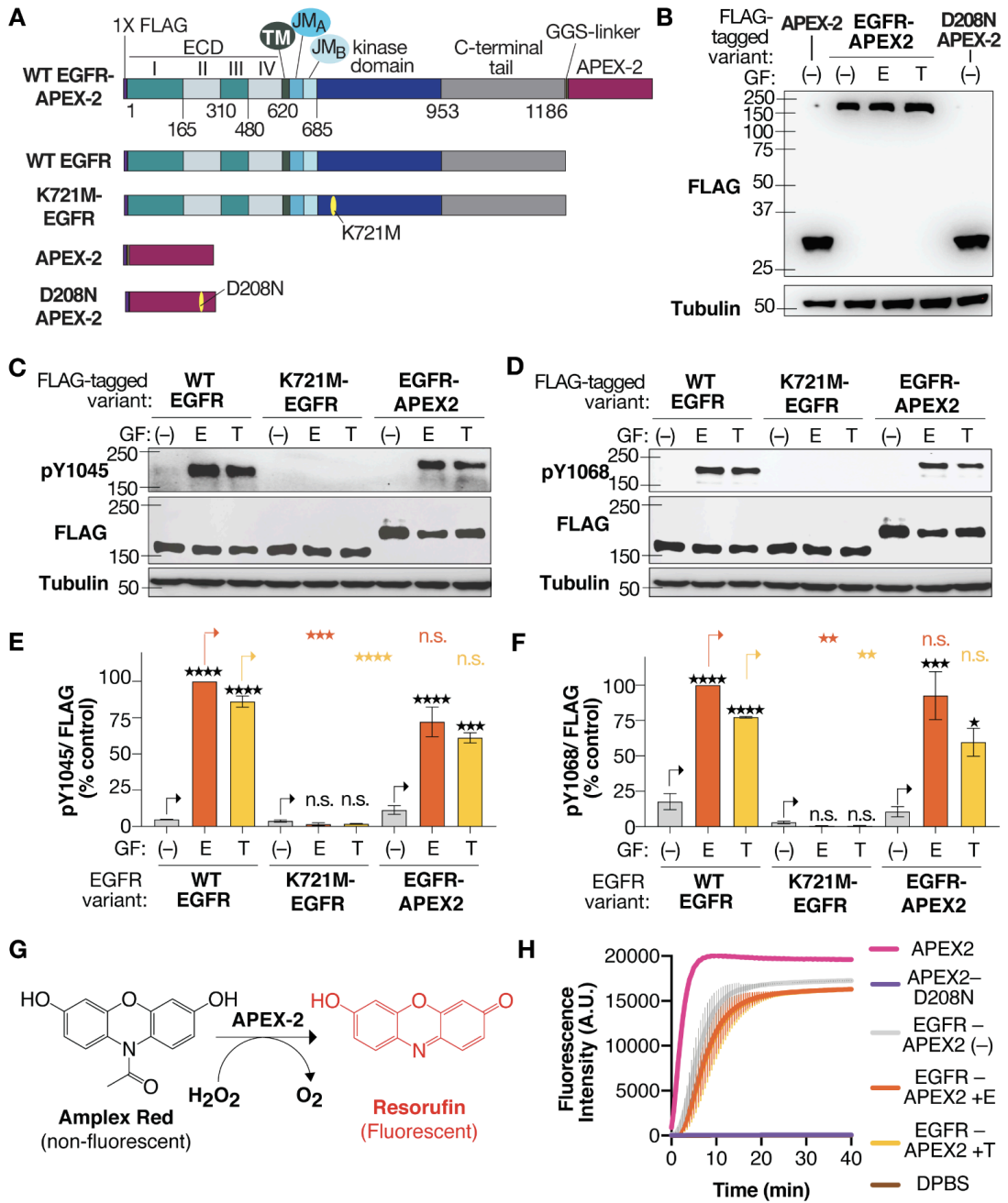
Figure 4.6. EGFR-APEX2 fusion retains both EGFR kinase activity and APEX2 peroxidase activity. (A) Domain diagram of constructs regarding the APEX2-based proximity labeling study: EGFR-APEX2, WT EGFR, K721M-EGFR (kinase-inactive), APEX2, and D208N-APEX2 (peroxidase-inactive). EGFR was fused to APEX2 with a short flexible GGS linker. (B) Western blot illustrating the expression of FLAG-tagged APEX2, EGFR-APEX2, and D208N-APEX2 as detected with an anti-FLAG antibody. Tubulin was used as the loading control. (C) Western blot illustrating the expression (FLAG) and autophosphorylation activity of WT EGFR, EGFR-APEX2, and K721M-EGFR (negative control) at C-tail tyrosine residue Y1045 8 mins after stimulation with EGF (E) or TGF-α (T). (D) Western blot illustrating the expression (FLAG) and autophosphorylation activity of WT EGFR, EGFR-APEX2, and K721M-EGFR at C-tail tyrosine residue Y1068 8 mins after stimulation with EGF (E) or TGF-α (T). Tubulin was used as the loading control. (E) Bar plots illustrating the normalized percent of pY1045/FLAG for western blots shown in C. (F) Bar plots illustrating the normalized percent of pY1068/FLAG for western blots shown in D. Each pY-EGFR/FLAG signal was normalized to the signal for WT EGFR treated with EGF. Error bars represent S.E.M. ****$p<0.0001$, ***$p<0.001$, n.s., not significant from one-way ANOVA with Dunnett's test. (G) Reaction schematic illustrating the peroxidase (APEX2) mediated conversion of Amplex Red (non-fluorescent) to Resorufin (fluorescent) in the presence of H_2O_2. (H) Results of Amplex red assay illustrating the enzymatic kinetics of the protein constructs CHO-K1 cells: APEX2 (pink), EGFR-APEX2 (without or with 16.7 nM EGF or TGF-α treatment; represented by grey, orange, and yellow lines respectively), D208N-APEX2 (purple; negative control). Figure adapted from Ref. [78]
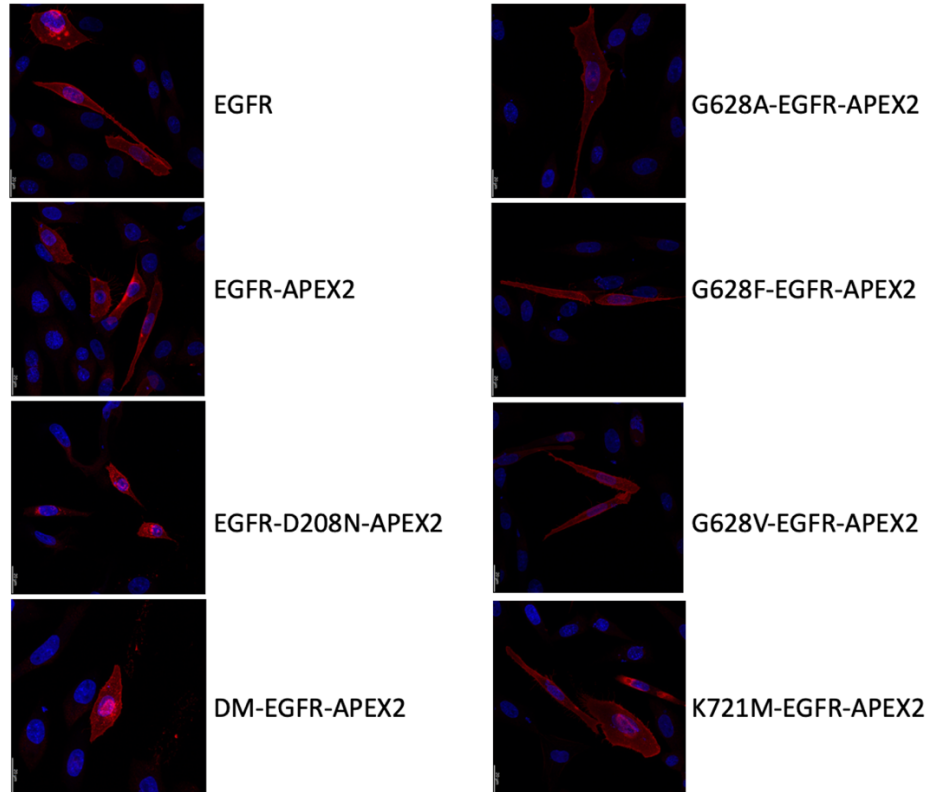
Figure 4.7. The constructs for the APEX2-base proximity labeling study were expressed and correctly localized at the plasma membrane. Confocal microscopy images of CHO-K1 cells expressing EGFR, EGFR-APEX2, EGFR-D208N-APEX2, DM-EGFR-APEX2 (TKI-resistant L834R/T766M double-mutant), G628A-EGFR-APEX2, G628F-EGFR-APEX2, G628V-EGFR-APEX2, and K721M-EGFR-APEX2 (kinase-inactive EGFR). In all constructs, FLAG-tag was at the N-terminus of EGFR and stained with Alexa Fluor 555-conjugated antibody (false-colored red) and the nuclear stain (false-colored blue).
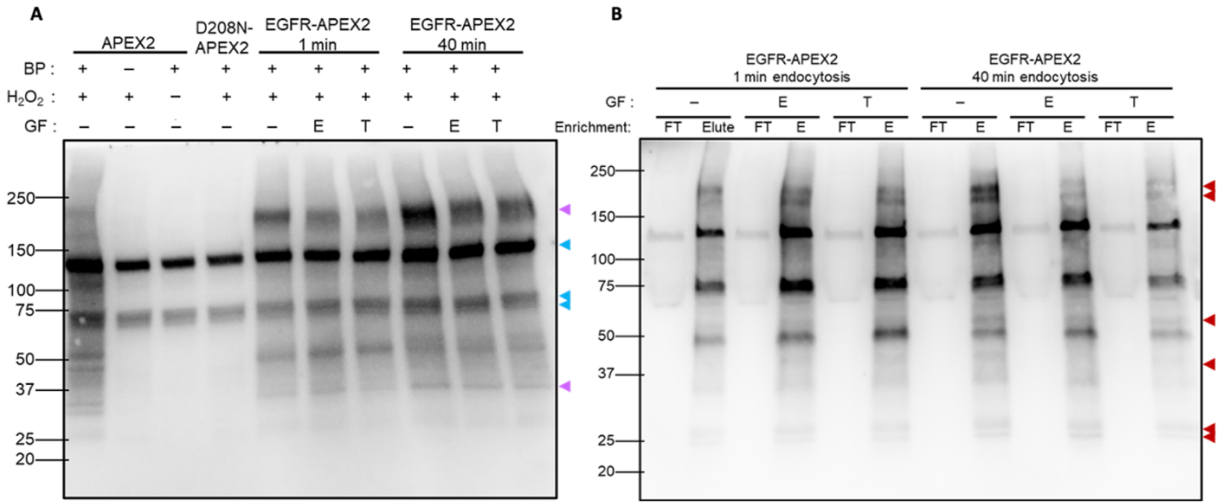
Figure 4.8. *in cellulo* biotinylation reactions of the APEX2 fusion constructs. (A) Western blot illustrating biotinylated proteins labeled in *cellulo* by APEX2, D208N-APEX2 (peroxidase-inactive APEX2, negative control), and EGFR-APEX2 (without or with 16.7 nM EGF or TGF-α stimulation for 1 min and 40 mins). The blue arrows indicate endogenous biotinylated protein at 130, 75, and 72 kDa. In the negative control lanes (D208N-APEX and APEX2 lacking either BP or H_2O_2), only the endogenous biotinylated proteins were visible. The pink arrows indicate additional biotinylated protein labeled by EGFR-APEX2. (B) Western blot illustrating biotinylated proteins after streptavidin pull-down enrichment experiments. The red arrows indicate biotinylated proteins resolved after the streptavidin pull-down enrichment treatment.

References

 (1) Cohen, S.; Elliott, G. A. The Stimulation of Epidermal Keratinization by a Protein Isolated from the Submaxillary Gland of the Mouse. *J. Invest. Dermatol.* **1963**, *40* (1), 1–5. https://doi.org/10.1038/jid.1963.1.

 (2) Arteaga, C. L.; Engelman, J. A. ERBB Receptors: From Oncogene Discovery to Basic Science to Mechanism-Based Cancer Therapeutics. *Cancer Cell* **2014**, *25* (3), 282–303. https://doi.org/10.1016/j.ccr.2014.02.025.

 (3) Blume-Jensen, P.; Hunter, T. Oncogenic Kinase Signalling. *Nature* **2001**, *411*, 355–365. https://doi.org/10.1038/35077225.

 (4) Ullrich, A.; Schlessinger, J. Signal Transduction by Receptors with Tyrosine Kinase Activity. *Cell* **1990**, *61* (2), 203–212. https://doi.org/10.1016/0092-8674(90)90801-K.

 (5) Libermann, T. A.; Nusbaum, H. R.; Razon, N.; Kris, R.; Lax, I.; Soreq, H.; Whittle, N.; Waterfield, M. D.; Ullrich, A.; Schlessinger, J. Amplification, Enhanced Expression and Possible Rearrangement of EGF Receptor Gene in Primary Human Brain Tumours of Glial Origin. *Nature* **1985**, *313* (5998), 144–147. https://doi.org/10.1038/313144a0.

 (6) Slamon, D. J. Proto-Oncogenes and Human Cancers. *N. Engl. J. Med.* **1987**, *317* (15), 955–957. https://doi.org/10.1056/NEJM198710083171509.

 (7) Yarden, Y.; Sliwkowski, M. X. Untangling the ErbB Signalling Network. *Nat. Rev. Mol. Cell Biol.* **2001**, *2* (2), 127–137. https://doi.org/10.1038/35052073.

 (8) Harris, R. C.; Chung, E.; Coffey, R. J. EGF Receptor Ligands. *Exp. Cell Res.* **2003**, *284* (1), 2–13. https://doi.org/10.1016/S0014-4827(02)00105-2.

 (9) Ebner, R.; Derynck, R. Epidermal Growth Factor and Transforming Growth Factor-Alpha: Differential Intracellular Routing and Processing of Ligand-Receptor Complexes. *Cell Regul.* **1991**, *2* (8), 599–612. https://doi.org/10.1091/mbc.2.8.599.

(10) French, A. R.; Tadaki, D. K.; Niyogi, S. K.; Lauffenburger, D. A. Intracellular Trafficking of Epidermal Growth Factor Family Ligands Is Directly Influenced by the PH Sensitivity of the Receptor/Ligand Interaction. *J. Biol. Chem.* **1995**, *270* (9), 4334–4340. https://doi.org/10.1074/jbc.270.9.4334.

(11) Roepstorff, K.; Grandal, M. V.; Henriksen, L.; Knudsen, S. L. J.; Lerdrup, M.; Grøvdal, L.; Willumsen, B. M.; van Deurs, B. Differential Effects of EGFR Ligands on Endocytic Sorting of the Receptor. *Traffic* **2009**, *10* (8), 1115–1127. https://doi.org/10.1111/j.1600-0854.2009.00943.x.

(12) Ronan, T.; Macdonald-Obermann, J. L.; Huelsmann, L.; Bessman, N. J.; Naegle, K. M.; Pike, L. J. Different Epidermal Growth Factor Receptor (EGFR) Agonists Produce Unique Signatures for the Recruitment of Downstream Signaling Proteins. *J. Biol. Chem.* **2016**, *291* (11), 5528–5540. https://doi.org/10.1074/jbc.M115.710087.

(13) Freed, D. M.; Bessman, N. J.; Kiyatkin, A.; Salazar-Cavazos, E.; Byrne, P. O.; Moore, J. O.; Valley, C. C.; Ferguson, K. M.; Leahy, D. J.; Lidke, D. S.; Lemmon, M. A. EGFR Ligands Differentially Stabilize Receptor Dimers to Specify Signaling Kinetics. *Cell* **2017**, *171* (3), 683-695.e18. https://doi.org/10.1016/j.cell.2017.09.017.

(14) Macdonald-Obermann, J. L.; Pike, L. J. Different Epidermal Growth Factor (EGF) Receptor Ligands Show Distinct Kinetics and Biased or Partial Agonism for Homodimer and Heterodimer Formation. *J. Biol. Chem.* **2014**, *289* (38), 26178–26188. https://doi.org/10.1074/jbc.M114.586826.

(15) Francavilla, C.; Papetti, M.; Rigbolt, K. T. G.; Pedersen, A.-K.; Sigurdsson, J. O.; Cazzamali, G.; Karemore, G.; Blagoev, B.; Olsen, J. V. Multilayered Proteomics Reveals Molecular Switches Dictating Ligand-Dependent EGFR Trafficking. *Nat. Struct. Mol. Biol.* **2016**, *23* (6), 608–618. https://doi.org/10.1038/nsmb.3218.

(16) Kovacs, E.; Zorn, J. A.; Huang, Y.; Barros, T.; Kuriyan, J. A Structural Perspective on the Regulation of the Epidermal Growth Factor Receptor. *Annu. Rev. Biochem.* **2015**, *84* (1), 739–764. https://doi.org/10.1146/annurev-biochem-060614-034402.

(17) Zhang, X.; Gureasko, J.; Shen, K.; Cole, P. A.; Kuriyan, J. An Allosteric Mechanism for Activation of the Kinase Domain of Epidermal Growth Factor Receptor. *Cell* **2006**, *125* (6), 1137–1149. https://doi.org/10.1016/j.cell.2006.05.013.

(18) Lemmon, M. A.; Schlessinger, J. Cell Signaling by Receptor Tyrosine Kinases. *Cell* **2010**, *141* (7), 1117–1134. https://doi.org/10.1016/j.cell.2010.06.011.

(19) Ogiso, H.; Ishitani, R.; Nureki, O.; Fukai, S.; Yamanaka, M.; Kim, J.-H.; Saito, K.; Sakamoto, A.; Inoue, M.; Shirouzu, M.; Yokoyama, S. Crystal Structure of the Complex of Human Epidermal Growth Factor and Receptor Extracellular Domains. *Cell* **2002**, *110* (6), 775–787. https://doi.org/10.1016/s0092-8674(02)00963-7.

(20) Huang, Y.; Ognjenović, J.; Karandur, D.; Merk, A.; Subramaniam, S.; Kuriyan, J. A Structural Mechanism for the Generation of Biased Agonism in the Epidermal Growth Factor Receptor. bioRxiv December 9, 2020, p 2020.12.08.417006. https://doi.org/10.1101/2020.12.08.417006.

(21) Garrett, T. P. J.; McKern, N. M.; Lou, M.; Elleman, T. C.; Adams, T. E.; Lovrecz, G. O.; Zhu, H.-J.; Walker, F.; Frenkel, M. J.; Hoyne, P. A.; Jorissen, R. N.; Nice, E. C.; Burgess, A. W.; Ward, C. W. Crystal Structure of a Truncated Epidermal Growth Factor Receptor Extracellular Domain Bound to Transforming Growth Factor Alpha. *Cell* **2002**, *110* (6), 763–773. https://doi.org/10.1016/s0092-8674(02)00940-6.

(22) He, L.; Hristova, K. Consequences of Replacing EGFR Juxtamembrane Domain with an Unstructured Sequence. *Sci. Rep.* **2012**, *2* (1), 854. https://doi.org/10.1038/srep00854.

(23) Jura, N.; Endres, N. F.; Engel, K.; Deindl, S.; Das, R.; Lamers, M. H.; Wemmer, D. E.; Zhang, X.; Kuriyan, J. Mechanism for Activation of the EGF Receptor Catalytic Domain by the Juxtamembrane Segment. *Cell* **2009**, *137* (7), 1293–1307. https://doi.org/10.1016/j.cell.2009.04.025.

(24) Red Brewer, M.; Choi, S. H.; Alvarado, D.; Moravcevic, K.; Pozzi, A.; Lemmon, M. A.; Carpenter, G. The Juxtamembrane Region of the EGF Receptor Functions as an Activation Domain. *Mol. Cell* **2009**, *34* (6), 641–651. https://doi.org/10.1016/j.molcel.2009.04.034.

(25) Thiel, K. W.; Carpenter, G. Epidermal Growth Factor Receptor Juxtamembrane Region Regulates Allosteric Tyrosine Kinase Activation. *Proc. Natl. Acad. Sci.* **2007**, *104* (49), 19238–19243. https://doi.org/10.1073/pnas.0703854104.

(26) Hubbard, S. R. The Juxtamembrane Region of EGFR Takes Center Stage. *Cell* **2009**, *137* (7), 1181–1183. https://doi.org/10.1016/j.cell.2009.06.008.

(27) Red Brewer, M.; Choi, S. H.; Alvarado, D.; Moravcevic, K.; Pozzi, A.; Lemmon, M. A.; Carpenter, G. The Juxtamembrane Region of the EGF Receptor Functions as an Activation Domain. *Mol. Cell* **2009**, *34* (6), 641–651. https://doi.org/10.1016/j.molcel.2009.04.034.

(28) Xue, F.; An, C.; Chen, L.; Liu, G.; Ren, F.; Guo, X.; Sun, H.; Mei, L.; Sun, X.; Li, J.; Tang, Y.; An, X.; Zheng, P. 4.1B Suppresses Cancer Cell Proliferation by Binding to EGFR P13 Region of

Intracellular Juxtamembrane Segment. *Cell Commun. Signal.* **2019**, *17* (1), 115. https://doi.org/10.1186/s12964-019-0431-6.

(29) Sato, T.; Pallavi, P.; Golebiewska, U.; McLaughlin, S.; Smith, S. O. Structure of the Membrane Reconstituted Transmembrane–Juxtamembrane Peptide EGFR(622–660) and Its Interaction with Ca2+/Calmodulin. *Biochemistry* **2006**, *45* (42), 12704–12714. https://doi.org/10.1021/bi061264m.

(30) Wood, E. R.; Shewchuk, L. M.; Ellis, B.; Brignola, P.; Brashear, R. L.; Caferro, T. R.; Dickerson, S. H.; Dickson, H. D.; Donaldson, K. H.; Gaul, M.; Griffin, R. J.; Hassell, A. M.; Keith, B.; Mullin, R.; Petrov, K. G.; Reno, M. J.; Rusnak, D. W.; Tadepalli, S. M.; Ulrich, J. C.; Wagner, C. D.; Vanderwall, D. E.; Waterson, A. G.; Williams, J. D.; White, W. L.; Uehling, D. E. 6-Ethynylthieno[3,2-d]- and 6-Ethynylthieno[2,3-d]Pyrimidin-4-Anilines as Tunable Covalent Modifiers of ErbB Kinases. *Proc. Natl. Acad. Sci. U. S. A.* **2008**, *105* (8), 2773–2778. https://doi.org/10.1073/pnas.0708281105.

(31) Luedtke, N. W.; Dexter, R. J.; Fried, D. B.; Schepartz, A. Surveying Polypeptide and Protein Domain Conformation and Association with FlAsH and ReAsH. *Nat. Chem. Biol.* **2007**, *3* (12), 779–784. https://doi.org/10.1038/nchembio.2007.49.

(32) Scheck, R. A.; Schepartz, A. Surveying Protein Structure and Function Using Bis-Arsenical Small Molecules. *Acc. Chem. Res.* **2011**, *44* (9), 654–665. https://doi.org/10.1021/ar2001028.

(33) Adams, S. R.; Campbell, R. E.; Gross, L. A.; Martin, B. R.; Walkup, G. K.; Yao, Y.; Llopis, J.; Tsien, R. Y. New Biarsenical Ligands and Tetracysteine Motifs for Protein Labeling in Vitro and in Vivo: Synthesis and Biological Applications. *J. Am. Chem. Soc.* **2002**, *124* (21), 6063–6076. https://doi.org/10.1021/ja017687n.

(34) Griffin, B. A.; Adams, S. R.; Tsien, R. Y. Specific Covalent Labeling of Recombinant Protein Molecules Inside Live Cells. *Science* **1998**, *281* (5374), 269–272. https://doi.org/10.1126/science.281.5374.269.

(35) Walker, A. S.; Rablen, P. R.; Schepartz, A. Rotamer-Restricted Fluorogenicity of the Bis-Arsenical ReAsH. *J. Am. Chem. Soc.* **2016**, *138* (22), 7143–7150. https://doi.org/10.1021/jacs.6b03422.

(36) Scheck, R. A.; Lowder, M. A.; Appelbaum, J. S.; Schepartz, A. Bipartite Tetracysteine Display Reveals Allosteric Control of Ligand-Specific EGFR Activation. *ACS Chem. Biol.* **2012**, *7* (8), 1367–1376. https://doi.org/10.1021/cb300216f.

(37) Doerner, A.; Scheck, R.; Schepartz, A. Growth Factor Identity Is Encoded by Discrete Coiled-Coil Rotamers in the EGFR Juxtamembrane Region. *Chem. Biol.* **2015**, *22* (6), 776–784. https://doi.org/10.1016/j.chembiol.2015.05.008.

(38) Cc, R.; A, W.; Da, L. Comparative Mitogenic Potencies of EGF and TGF Alpha and Their Dependence on Receptor-Limitation versus Ligand-Limitation. *Med. Biol. Eng. Comput.* **1998**, *36* (4). https://doi.org/10.1007/BF02523222.

(39) Baldys, A.; Göoz, M.; Morinelli, T. A.; Lee, M.-H.; Raymond, J. R. Jr.; Luttrell, L. M.; Raymond, J. R. Sr. Essential Role of C-Cbl in Amphiregulin-Induced Recycling and Signaling of the Endogenous Epidermal Growth Factor Receptor. *Biochemistry* **2009**, *48* (7), 1462–1473. https://doi.org/10.1021/bi801771g.

(40) Thoresen, G. H.; Guren, T. K.; Sandnes, D.; Peak, M.; Agius, L.; Christoffersen, T. Response to Transforming Growth Factor α (TGFα) and Epidermal Growth Factor (EGF) in Hepatocytes:

Lower EGF Receptor Affinity of TGFα Is Associated with More Sustained Activation of P42/P44 Mitogen-Activated Protein Kinase and Greater Efficacy in Stimulation of DNA Synthesis. *J. Cell. Physiol.* **1998**, *175* (1), 10–18. https://doi.org/10.1002/(SICI)1097-4652(199804)175:1<10::AID-JCP2>3.0.CO;2-F.

(41) Seth, D.; Shaw, K.; Jazayeri, J.; Leedman, P. J. Complex Post-Transcriptional Regulation of EGF-Receptor Expression by EGF and TGF-α in Human Prostate Cancer Cells. *Br. J. Cancer* **1999**, *80* (5–6), 657. https://doi.org/10.1038/sj.bjc.6690407.

(42) Wilson, K. J.; Mill, C.; Lambert, S.; Buchman, J.; Wilson, T. R.; Hernandez-Gordillo, V.; Gallo, R. M.; Ades, L. M. C.; Settleman, J.; Riese, D. J. EGFR Ligands Exhibit Functional Differences in Models of Paracrine and Autocrine Signaling. *Growth Factors* **2012**, *30* (2), 107–116. https://doi.org/10.3109/08977194.2011.649918.

(43) Lu, C.; Mi, L.-Z.; Grey, M. J.; Zhu, J.; Graef, E.; Yokoyama, S.; Springer, T. A. Structural Evidence for Loose Linkage between Ligand Binding and Kinase Activation in the Epidermal Growth Factor Receptor. *Mol. Cell. Biol.* **2010**, *30* (22), 5432–5443. https://doi.org/10.1128/MCB.00742-10.

(44) Gray, J. J.; Moughon, S.; Wang, C.; Schueler-Furman, O.; Kuhlman, B.; Rohl, C. A.; Baker, D. Protein-Protein Docking with Simultaneous Optimization of Rigid-Body Displacement and Side-Chain Conformations. *J. Mol. Biol.* **2003**, *331* (1), 281–299. https://doi.org/10.1016/s0022-2836(03)00670-3.

(45) Barth, P.; Schonbrun, J.; Baker, D. Toward High-Resolution Prediction and Design of Transmembrane Helical Protein Structures. *Proc. Natl. Acad. Sci.* **2007**, *104* (40), 15682–15687. https://doi.org/10.1073/pnas.0702515104.

(46) Alford, R. F.; Leman, J. K.; Weitzner, B. D.; Duran, A. M.; Tilley, D. C.; Elazar, A.; Gray, J. J. An Integrated Framework Advancing Membrane Protein Modeling and Design. *PLOS Comput. Biol.* **2015**, *11* (9), e1004398. https://doi.org/10.1371/journal.pcbi.1004398.

(47) Yarov-Yarovoy, V.; Schonbrun, J.; Baker, D. Multipass Membrane Protein Structure Prediction Using Rosetta. *Proteins* **2006**, *62* (4), 1010–1025. https://doi.org/10.1002/prot.20817.

(48) Endres, N. F.; Das, R.; Smith, A. W.; Arkhipov, A.; Kovacs, E.; Huang, Y.; Pelton, J. G.; Shan, Y.; Shaw, D. E.; Wemmer, D. E.; Groves, J. T.; Kuriyan, J. Conformational Coupling across the Plasma Membrane in Activation of the EGF Receptor. *Cell* **2013**, *152* (3), 543–556. https://doi.org/10.1016/j.cell.2012.12.032.

(49) Lemmon, M. A.; Treutlein, H. R.; Adams, P. D.; Brünger, A. T.; Engelman, D. M. A Dimerization Motif for Transmembrane Alpha-Helices. *Nat. Struct. Biol.* **1994**, *1* (3), 157–163. https://doi.org/10.1038/nsb0394-157.

(50) Russ, W. P.; Engelman, D. M. The GxxxG Motif: A Framework for Transmembrane Helix-Helix Association11Edited by G. von Heijne. *J. Mol. Biol.* **2000**, *296* (3), 911–919. https://doi.org/10.1006/jmbi.1999.3489.

(51) Senes, A.; Engel, D. E.; DeGrado, W. F. Folding of Helical Membrane Proteins: The Role of Polar, GxxxG-like and Proline Motifs. *Curr. Opin. Struct. Biol.* **2004**, *14* (4), 465–479. https://doi.org/10.1016/j.sbi.2004.07.007.

(52) Escher, C.; Cymer, F.; Schneider, D. Two GxxxG-Like Motifs Facilitate Promiscuous Interactions of the Human ErbB Transmembrane Domains. *J. Mol. Biol.* **2009**, *389* (1), 10–16. https://doi.org/10.1016/j.jmb.2009.04.002.

(53) Mendrola, J. M.; Berger, M. B.; King, M. C.; Lemmon, M. A. The Single Transmembrane Domains of ErbB Receptors Self-Associate in Cell Membranes*. *J. Biol. Chem.* **2002**, *277* (7), 4704–4712. https://doi.org/10.1074/jbc.M108681200.

(54) Heukers, R.; Vermeulen, J. F.; Fereidouni, F.; Bader, A. N.; Voortman, J.; Roovers, R. C.; Gerritsen, H. C.; van Bergen en Henegouwen, P. M. P. Endocytosis of EGFR Requires Its Kinase Activity and N-Terminal Transmembrane Dimerization Motif. *J. Cell Sci.* **2013**, *126* (21), 4900–4912. https://doi.org/10.1242/jcs.128611.

(55) Sinclair, J. K. L.; Walker, A. S.; Doerner, A. E.; Schepartz, A. Mechanism of Allosteric Coupling into and through the Plasma Membrane by EGFR. *Cell Chem. Biol.* **2018**, *25* (7), 857-870.e7. https://doi.org/10.1016/j.chembiol.2018.04.005.

(56) Hedger, G.; Sansom, M. S. P.; Koldsø, H. The Juxtamembrane Regions of Human Receptor Tyrosine Kinases Exhibit Conserved Interaction Sites with Anionic Lipids. *Sci. Rep.* **2015**, *5* (1), 9198. https://doi.org/10.1038/srep09198.

(57) Abd Halim, K. B.; Koldsø, H.; Sansom, M. S. P. Interactions of the EGFR Juxtamembrane Domain with PIP2-Containing Lipid Bilayers: Insights from Multiscale Molecular Dynamics Simulations. *Biochim. Biophys. Acta BBA - Gen. Subj.* **2015**, *1850* (5), 1017–1025. https://doi.org/10.1016/j.bbagen.2014.09.006.

(58) Aifa, S.; Johansen, K.; Nilsson, U. K.; Liedberg, B.; Lundström, I.; Svensson, S. P. S. Interactions between the Juxtamembrane Domain of the EGFR and Calmodulin Measured by Surface Plasmon Resonance. *Cell. Signal.* **2002**, *14* (12), 1005–1013. https://doi.org/10.1016/S0898-6568(02)00034-7.

(59) Martín-Nieto, J.; Villalobo, A. The Human Epidermal Growth Factor Receptor Contains a Juxtamembrane Calmodulin-Binding Site. *Biochemistry* **1998**, *37* (1), 227–236. https://doi.org/10.1021/bi971765v.

(60) Sengupta, P.; Bosis, E.; Nachliel, E.; Gutman, M.; Smith, S. O.; Mihályné, G.; Zaitseva, I.; McLaughlin, S. EGFR Juxtamembrane Domain, Membranes, and Calmodulin: Kinetics of Their Interaction. *Biophys. J.* **2009**, *96* (12), 4887–4895. https://doi.org/10.1016/j.bpj.2009.03.027.

(61) Li, H.; Panina, S.; Kaur, A.; Ruano, M. J.; Sánchez-González, P.; la Cour, J. M.; Stephan, A.; Olesen, U. H.; Berchtold, M. W.; Villalobo, A. Regulation of the Ligand-Dependent Activation of the Epidermal Growth Factor Receptor by Calmodulin. *J. Biol. Chem.* **2012**, *287* (5), 3273–3281. https://doi.org/10.1074/jbc.M111.317529.

(62) McLaughlin, S.; Smith, S. O.; Hayman, M. J.; Murray, D. An Electrostatic Engine Model for Autoinhibition and Activation of the Epidermal Growth Factor Receptor (EGFR/ErbB) Family. *J. Gen. Physiol.* **2005**, *126* (1), 41–53. https://doi.org/10.1085/jgp.200509274.

(63) Hake, M. J.; Choowongkomon, K.; Kostenko, O.; Carlin, C. R.; Sönnichsen, F. D. Specificity Determinants of a Novel Nck Interaction with the Juxtamembrane Domain of the Epidermal Growth Factor Receptor. *Biochemistry* **2008**, *47* (10), 3096–3108. https://doi.org/10.1021/bi701549a.

(64) Poppleton, H. M.; Sun, H.; Mullenix, J. B.; Wiepz, G. J.; Bertics, P. J.; Patel, T. B. The Juxtamembrane Region of the Epidermal Growth Factor Receptor Is Required for Phosphorylation of GαS. *Arch. Biochem. Biophys.* **2000**, *383* (2), 309–317. https://doi.org/10.1006/abbi.2000.2095.

(65) Cochet, C.; Filhol, O.; Payrastre, B.; Hunter, T.; Gill, G. N. Interaction between the Epidermal Growth Factor Receptor and Phosphoinoside Kinases. *J. Biol. Chem.* **1991**, *266* (1), 637–644.

(66) Cochet, C.; Gill, G. N.; Meisenhelder, J.; Cooper, J. A.; Hunter, T. C-Kinase Phosphorylates the Epidermal Growth Factor Receptor and Reduces Its Epidermal Growth Factor-Stimulated Tyrosine Protein Kinase Activity. *J. Biol. Chem.* **1984**, *259* (4), 2553–2558.

(67) Davis, R. J.; Czech, M. P. Tumor-Promoting Phorbol Diesters Cause the Phosphorylation of Epidermal Growth Factor Receptors in Normal Human Fibroblasts at Threonine-654. *Proc. Natl. Acad. Sci.* **1985**, *82* (7), 1974–1978. https://doi.org/10.1073/pnas.82.7.1974.

(68) Hunter, T.; Ling, N.; Cooper, J. A. Protein Kinase C Phosphorylation of the EGF Receptor at a Threonine Residue Close to the Cytoplasmic Face of the Plasma Membrane. *Nature* **1984**, *311* (5985), 480–483. https://doi.org/10.1038/311480a0.

(69) Morrison, P.; Takishima, K.; Rosner, M. R. Role of Threonine Residues in Regulation of the Epidermal Growth Factor Receptor by Protein Kinase C and Mitogen-Activated Protein Kinase. *J. Biol. Chem.* **1993**, *268* (21), 15536–15543. https://doi.org/10.1016/S0021-9258(18)82290-6.

(70) Takishima, K.; Friedman, B.; Fujiki, H.; Rosner, M. R. Thapsigargin, a Novel Promoter, Phosphorylates the Epidermal Growth Factor Receptor at Threonine 669. *Biochem. Biophys. Res. Commun.* **1988**, *157* (2), 740–746. https://doi.org/10.1016/s0006-291x(88)80312-7.

(71) Winograd-Katz, S. E.; Levitzki, A. Cisplatin Induces PKB/Akt Activation and P38MAPK Phosphorylation of the EGF Receptor. *Oncogene* **2006**, *25* (56), 7381–7390. https://doi.org/10.1038/sj.onc.1209737.

(72) Kil, S. J.; Hobert, M.; Carlin, C. A Leucine-Based Determinant in the Epidermal Growth Factor Receptor Juxtamembrane Domain Is Required for the Efficient Transport of Ligand-Receptor Complexes to Lysosomes. *J. Biol. Chem.* **1999**, *274* (5), 3141–3150. https://doi.org/10.1074/jbc.274.5.3141.

(73) Kil, S. J.; Carlin, C. EGF Receptor Residues Leu(679), Leu(680) Mediate Selective Sorting of Ligand-Receptor Complexes in Early Endosomal Compartments. *J. Cell. Physiol.* **2000**, *185* (1), 47–60. https://doi.org/10.1002/1097-4652(200010)185:1<47::AID-JCP4>3.0.CO;2-O.

(74) Cai, G.; Zhu, L.; Chen, X.; Sun, K.; Liu, C.; Sen, G. C.; Stark, G. R.; Qin, J.; Li, X. TRAF4 Binds to the Juxtamembrane Region of EGFR Directly and Promotes Kinase Activation. *Proc. Natl. Acad. Sci. U. S. A.* **2018**, *115* (45), 11531–11536. https://doi.org/10.1073/pnas.1809599115.

(75) Viegas, A.; Yin, D. M.; Borggräfe, J.; Viennet, T.; Falke, M.; Schmitz, A.; Famulok, M.; Etzkorn, M. Molecular Architecture of a Network of Potential Intracellular EGFR Modulators: ARNO, CaM, Phospholipids, and the Juxtamembrane Segment. *Structure* **2020**, *28* (1), 54-62.e5. https://doi.org/10.1016/j.str.2019.11.001.

(76) Cotton, C. U.; Hobert, M. E.; Ryan, S.; Carlin, C. R. Basolateral EGF Receptor Sorting Regulated by Functionally Distinct Mechanisms in Renal Epithelial Cells. *Traffic Cph. Den.* **2013**, *14* (3), 337–354. https://doi.org/10.1111/tra.12032.

(77) Lin, S. Y.; Makino, K.; Xia, W.; Matin, A.; Wen, Y.; Kwong, K. Y.; Bourguignon, L.; Hung, M. C. Nuclear Localization of EGF Receptor and Its Potential New Role as a Transcription Factor. *Nat. Cell Biol.* **2001**, *3* (9), 802–808. https://doi.org/10.1038/ncb0901-802.

(78) Mozumdar, D. Investigating the Effect of Allostery on Downstream Biology of the Epidermal Growth Factor Receptor. *Yale Grad. Sch. Arts Sci. Diss.* **2021**.

(79) Kovacs, E.; Zorn, J. A.; Huang, Y.; Barros, T.; Kuriyan, J. A Structural Perspective on the Regulation of the Epidermal Growth Factor Receptor. *Annu. Rev. Biochem.* **2015**, *84* (1), 739–764. https://doi.org/10.1146/annurev-biochem-060614-034402.

(80) Mozumdar, D.; Chang, H.-H.; Quach, K.; Doerner, A.; Zhang, X.; Schepartz, A. Coiled Coil Control of Growth Factor and Inhibitor-Dependent EGFR Trafficking and Degradation. *Manuscr. Rev.*

(81) Friedman, B.; Frackelton, A. R.; Ross, A. H.; Connors, J. M.; Fujiki, H.; Sugimura, T.; Rosner, M. R. Tumor Promoters Block Tyrosine-Specific Phosphorylation of the Epidermal Growth Factor Receptor. *Proc. Natl. Acad. Sci. U. S. A.* **1984**, *81* (10), 3034–3038. https://doi.org/10.1073/pnas.81.10.3034.

(82) Lin, C. R.; Chen, W. S.; Lazar, C. S.; Carpenter, C. D.; Gill, G. N.; Evans, R. M.; Rosenfeld, M. G. Protein Kinase C Phosphorylation at Thr 654 of the Unoccupied EGF Receptor and EGF Binding Regulate Functional Receptor Loss by Independent Mechanisms. *Cell* **1986**, *44* (6), 839–848. https://doi.org/10.1016/0092-8674(86)90006-1.

(83) Huang, F.; Jiang, X.; Sorkin, A. Tyrosine Phosphorylation of the Beta2 Subunit of Clathrin Adaptor Complex AP-2 Reveals the Role of a Di-Leucine Motif in the Epidermal Growth Factor Receptor Trafficking. *J. Biol. Chem.* **2003**, *278* (44), 43411–43417. https://doi.org/10.1074/jbc.M306072200.

(84) Kluba, M.; Engelborghs, Y.; Hofkens, J.; Mizuno, H. Inhibition of Receptor Dimerization as a Novel Negative Feedback Mechanism of EGFR Signaling. *PLOS ONE* **2015**, *10* (10), e0139971. https://doi.org/10.1371/journal.pone.0139971.

(85) Huang, Y.; Ognjenovic, J.; Karandur, D.; Miller, K.; Merk, A.; Subramaniam, S.; Kuriyan, J. A Molecular Mechanism for the Generation of Ligand-Dependent Differential Outputs by the Epidermal Growth Factor Receptor. *eLife* **2021**, *10*, e73218. https://doi.org/10.7554/eLife.73218.

(86) Malhotra, S.; Joseph, A. P.; Thiyagalingam, J.; Topf, M. Assessment of Protein–Protein Interfaces in Cryo-EM Derived Assemblies. *Nat. Commun.* **2021**, *12* (1), 3399. https://doi.org/10.1038/s41467-021-23692-x.

(87) Wu, X.; Rapoport, T. A. Cryo-EM Structure Determination of Small Proteins by Nanobody-Binding Scaffolds (Legobodies). *Proc. Natl. Acad. Sci.* **2021**, *118* (41), e2115001118. https://doi.org/10.1073/pnas.2115001118.

(88) Zhang, K.; Horikoshi, N.; Li, S.; Powers, A. S.; Hameedi, M. A.; Pintilie, G. D.; Chae, H.-D.; Khan, Y. A.; Suomivuori, C.-M.; Dror, R. O.; Sakamoto, K. M.; Chiu, W.; Wakatsuki, S. Cryo-EM, Protein Engineering, and Simulation Enable the Development of Peptide Therapeutics against Acute Myeloid Leukemia. *ACS Cent. Sci.* **2022**, *8* (2), 214–222. https://doi.org/10.1021/acscentsci.1c01090.

(89) Saban, S. D.; Silvestry, M.; Nemerow, G. R.; Stewart, P. L. Visualization of α-Helices in a 6-Ångstrom Resolution Cryoelectron Microscopy Structure of Adenovirus Allows Refinement of Capsid Protein Assignments. *J. Virol.* **2006**, *80* (24), 12049–12059. https://doi.org/10.1128/JVI.01652-06.

(90) Kantsadi, A. L.; Hatzopoulos, G. N.; Gönczy, P.; Vakonakis, I. Structures of SAS-6 Coiled Coil Hold Implications for the Polarity of the Centriolar Cartwheel. *Structure* **2022**, *30* (5), 671-684.e5. https://doi.org/10.1016/j.str.2022.02.005.

(91) Carpenter, E. P.; Beis, K.; Cameron, A. D.; Iwata, S. Overcoming the Challenges of Membrane Protein Crystallography. *Curr. Opin. Struct. Biol.* **2008**, *18* (5), 581–586. https://doi.org/10.1016/j.sbi.2008.07.001.

(92) Kleywegt, G. J.; Jones, T. A. Databases in Protein Crystallography. *Acta Crystallogr. D Biol. Crystallogr.* **1998**, *54* (6), 1119–1131. https://doi.org/10.1107/S0907444998007100.

(93) Usón, I.; Sheldrick, G. M. Advances in Direct Methods for Protein Crystallography. *Curr. Opin. Struct. Biol.* **1999**, *9* (5), 643–648. https://doi.org/10.1016/S0959-440X(99)00020-2.

(94) Ravikumar, A.; Gopnarayan, M. N.; Subramaniam, S.; Srinivasan, N. Comparison of Side-Chain Dispersion in Protein Structures Determined by Cryo-EM and X-Ray Crystallography. *IUCrJ* **2022**, *9* (1), 98–103. https://doi.org/10.1107/S2052252521011945.

(95) Woolfson, D. N. The Design of Coiled-Coil Structures and Assemblies. *Adv. Protein Chem.* **2005**, *70*, 79–112. https://doi.org/10.1016/S0065-3233(05)70004-8.

(96) Scheck, R. A.; Lowder, M. A.; Appelbaum, J. S.; Schepartz, A. Bipartite Tetracysteine Display Reveals Allosteric Control of Ligand-Specific EGFR Activation. *ACS Chem. Biol.* **2012**, *7* (8), 1367–1376. https://doi.org/10.1021/cb300216f.

(97) O'Shea, E. K.; Lumb, K. J.; Kim, P. S. Peptide 'Velcro': Design of a Heterodimeric Coiled Coil. *Curr. Biol.* **1993**, *3* (10), 658–667. https://doi.org/10.1016/0960-9822(93)90063-T.

(98) Harbury, P. B.; Zhang, T.; Kim, P. S.; Alber, T. A Switch Between Two-, Three-, and Four-Stranded Coiled Coils in GCN4 Leucine Zipper Mutants. *Science* **1993**, *262* (5138), 1401–1407. https://doi.org/10.1126/science.8248779.

(99) van Rosmalen, M.; Krom, M.; Merkx, M. Tuning the Flexibility of Glycine-Serine Linkers To Allow Rational Design of Multidomain Proteins. *Biochemistry* **2017**. https://doi.org/10.1021/acs.biochem.7b00902.

(100) Kelly, S. M.; Price, N. C. The Use of Circular Dichroism in the Investigation of Protein Structure and Function. *Curr. Protein Pept. Sci.* **2000**, *1* (4), 349–384.

(101) Kelly, S. M.; Jess, T. J.; Price, N. C. How to Study Proteins by Circular Dichroism. *Biochim. Biophys. Acta BBA - Proteins Proteomics* **2005**, *1751* (2), 119–139. https://doi.org/10.1016/j.bbapap.2005.06.005.

(102) Greenfield, N. J. Using Circular Dichroism Spectra to Estimate Protein Secondary Structure. *Nat. Protoc.* **2006**, *1* (6), 2876–2890. https://doi.org/10.1038/nprot.2006.202.

(103) Fort, A. G.; Spray, D. C. Trifluoroethanol Reveals Helical Propensity at Analogous Positions in Cytoplasmic Domains of Three Connexins. *Biopolymers* **2009**, *92* (3), 173–182. https://doi.org/10.1002/bip.21166.

(104) Maroun, R. G.; Gayet, S.; Benleulmi, M. S.; Porumb, H.; Zargarian, L.; Merad, H.; Leh, H.; Mouscadet, J.-F.; Troalen, F.; Fermandjian, S. Peptide Inhibitors of HIV-1 Integrase Dissociate the Enzyme Oligomers. *Biochemistry* **2001**, *40* (46), 13840–13848. https://doi.org/10.1021/bi011328n.

(105) MacPhee, C. E.; Perugini, M. A.; H. Sawyer, W.; Howlett, G. J. Trifluoroethanol Induces the Self-Association of Specific Amphipathic Peptides. *FEBS Lett.* **1997**, *416* (3), 265–268. https://doi.org/10.1016/S0014-5793(97)01224-6.

(106) Kuroda, Y.; Maeda, Y.; Sawa, S.; Shibata, K.; Miyamoto, K.; Nakagawa, T. Effects of Detergents on the Secondary Structures of Prion Protein Peptides as Studied by CD Spectroscopy. *J. Pept. Sci.* **2003**, *9* (4), 212–220. https://doi.org/10.1002/psc.447.

(107)   Boros, S.; Gáspári, Z.; Batta, G. Accurate NMR Determinations of Proton–Proton Distances. In *Annual Reports on NMR Spectroscopy*; Elsevier, 2018; Vol. 94, pp 1–39. https://doi.org/10.1016/bs.arnmr.2017.12.002.

(108)   Wang, Y.; Shortle, D. Residual Helical and Turn Structure in the Denatured State of Staphylococcal Nuclease: Analysis of Peptide Fragments. *Fold. Des.* **1997**, *2* (2), 93–100. https://doi.org/10.1016/S1359-0278(97)00013-8.

(109)   Wüthrich, K. NMR with Proteins and Nucleic Acids. *Europhys. News* **1986**, *17* (1), 11–13. https://doi.org/10.1051/epn/19861701011.

(110)   Dyson, H. J.; Wright, P. E. Defining Solution Conformations of Small Linear Peptides. *Annu. Rev. Biophys. Biophys. Chem.* **1991**, *20*, 519–538. https://doi.org/10.1146/annurev.bb.20.060191.002511.

(111)   Arkhipov, A.; Shan, Y.; Das, R.; Endres, N. F.; Eastwood, M. P.; Wemmer, D. E.; Kuriyan, J.; Shaw, D. E. Architecture and Membrane Interactions of the EGF Receptor. *Cell* **2013**, *152* (3), 557–569. https://doi.org/10.1016/j.cell.2012.12.030.

(112)   Bocharov, E. V.; Lesovoy, D. M.; Pavlov, K. V.; Pustovalova, Y. E.; Bocharova, O. V.; Arseniev, A. S. Alternative Packing of EGFR Transmembrane Domain Suggests That Protein–Lipid Interactions Underlie Signal Conduction across Membrane. *Biochim. Biophys. Acta BBA - Biomembr.* **2016**, *1858* (6), 1254–1261. https://doi.org/10.1016/j.bbamem.2016.02.023.

(113)   Bragin, P. E.; Kuznetsov, A. S.; Bocharova, O. V.; Volynsky, P. E.; Arseniev, A. S.; Efremov, R. G.; Mineev, K. S. Probing the Effect of Membrane Contents on Transmembrane Protein-Protein Interaction Using Solution NMR and Computer Simulations. *Biochim. Biophys. Acta BBA - Biomembr.* **2018**, *1860* (12), 2486–2498. https://doi.org/10.1016/j.bbamem.2018.09.013.

(114)   Viennet, T.; Bungert-Plümke, S.; Elter, S.; Viegas, A.; Fahlke, C.; Etzkorn, M. Reconstitution and NMR Characterization of the Ion-Channel Accessory Subunit Barttin in Detergents and Lipid-Bilayer Nanodiscs. *Front. Mol. Biosci.* **2019**, *6*, 13. https://doi.org/10.3389/fmolb.2019.00013.

(115)   Goncharuk, M. V.; Schulga, A. A.; Ermolyuk, Ya. S.; Tkach, E. N.; Goncharuk, S. A.; Pustovalova, Yu. E.; Mineev, K. S.; Bocharov, E. V.; Maslennikov, I. V.; Arseniev, A. S.; Kirpichnikov, M. P. Bacterial Synthesis, Purification, and Solubilization of Transmembrane Segments of ErbB Family Receptors. *Mol. Biol.* **2011**, *45* (5), 823–832. https://doi.org/10.1134/S0026893311040066.

(116)   Morrison, E. A.; Henzler-Wildman, K. A. Reconstitution of Integral Membrane Proteins into Isotropic Bicelles with Improved Sample Stability and Expanded Lipid Composition Profile. *Biochim. Biophys. Acta BBA - Biomembr.* **2012**, *1818* (3), 814–820. https://doi.org/10.1016/j.bbamem.2011.12.020.

(117)   Glück, J. M.; Wittlich, M.; Feuerstein, S.; Hoffmann, S.; Willbold, D.; Koenig, B. W. Integral Membrane Proteins in Nanodiscs Can Be Studied by Solution NMR Spectroscopy. *J. Am. Chem. Soc.* **2009**, *131* (34), 12060–12061. https://doi.org/10.1021/ja904897p.

(118)   Günsel, U.; Hagn, F. Lipid Nanodiscs for High-Resolution NMR Studies of Membrane Proteins. *Chem. Rev.* **2022**, *122* (10), 9395–9421. https://doi.org/10.1021/acs.chemrev.1c00702.

(119)   Hagn, F.; Etzkorn, M.; Raschle, T.; Wagner, G. Optimized Phospholipid Bilayer Nanodiscs Facilitate High-Resolution Structure Determination of Membrane Proteins. *J. Am. Chem. Soc.* **2013**, *135* (5), 1919–1925. https://doi.org/10.1021/ja310901f.

(120)   Bengtsen, T.; Holm, V. L.; Kjølbye, L. R.; Midtgaard, S. R.; Johansen, N. T.; Tesei, G.; Bottaro, S.; Schiøtt, B.; Arleth, L.; Lindorff-Larsen, K. Structure and Dynamics of a Nanodisc by Integrating NMR, SAXS and SANS Experiments with Molecular Dynamics Simulations. *eLife* **2020**, *9*, e56518. https://doi.org/10.7554/eLife.56518.

(121)   Nakanishi, H.; Hayashida, K.; Nishizawa, T.; Oshima, A.; Abe, K. Cryo-EM of the ATP11C Flippase Reconstituted in Nanodiscs Shows a Distended Phospholipid Bilayer Inner Membrane around Transmembrane Helix 2. *J. Biol. Chem.* **2022**, *298* (1), 101498. https://doi.org/10.1016/j.jbc.2021.101498.

(122)   Redhair, M.; Clouser, A. F.; Atkins, W. M. Hydrogen-Deuterium Exchange Mass Spectrometry of Membrane Proteins in Lipid Nanodiscs. *Chem. Phys. Lipids* **2019**, *220*, 14–22. https://doi.org/10.1016/j.chemphyslip.2019.02.007.

(123)   Ritchie, T. K.; Grinkova, Y. V.; Bayburt, T. H.; Denisov, I. G.; Zolnerciks, J. K.; Atkins, W. M.; Sligar, S. G. Reconstitution of Membrane Proteins in Phospholipid Bilayer Nanodiscs. In *Methods in Enzymology*; Elsevier, 2009; Vol. 464, pp 211–231. https://doi.org/10.1016/S0076-6879(09)64011-8.

(124)   Reis, R. I.; Moraes, I. Probing Membrane Protein Assembly into Nanodiscs by In Situ Dynamic Light Scattering: A2A Receptor as a Case Study. *Biology* **2020**, *9* (11), 400. https://doi.org/10.3390/biology9110400.

(125)   Orekhov, P. S.; Bozdaganyan, M. E.; Voskoboynikova, N.; Mulkidjanian, A. Y.; Karlova, M. G.; Yudenko, A.; Remeeva, A.; Ryzhykau, Y. L.; Gushchin, I.; Gordeliy, V. I.; Sokolova, O. S.; Steinhoff, H.-J.; Kirpichnikov, M. P.; Shaitan, K. V. Mechanisms of Formation, Structure, and Dynamics of Lipoprotein Discs Stabilized by Amphiphilic Copolymers: A Comprehensive Review. *Nanomaterials* **2022**, *12* (3), 361. https://doi.org/10.3390/nano12030361.

(126)   Polovinkin, V.; Gushchin, I.; Sintsov, M.; Round, E.; Balandin, T.; Chervakov, P.; Schevchenko, V.; Utrobin, P.; Popov, A.; Borshchevskiy, V.; Mishin, A.; Kuklin, A.; Willbold, D.; Chupin, V.; Popot, J.-L.; Gordeliy, V. High-Resolution Structure of a Membrane Protein Transferred from Amphipol to a Lipidic Mesophase. *J. Membr. Biol.* **2014**, *247* (9), 997–1004. https://doi.org/10.1007/s00232-014-9700-x.

(127)   Tribet, C.; Audebert, R.; Popot, J.-L. Amphipols: Polymers That Keep Membrane Proteins Soluble in Aqueous Solutions. *Proc. Natl. Acad. Sci.* **1996**, *93* (26), 15047–15050. https://doi.org/10.1073/pnas.93.26.15047.

(128)   Zoonens, M.; Popot, J.-L. Amphipols for Each Season. *J. Membr. Biol.* **2014**, *247* (9), 759–796. https://doi.org/10.1007/s00232-014-9666-8.

(129)   Hein, C.; Henrich, E.; Orbán, E.; Dötsch, V.; Bernhard, F. Hydrophobic Supplements in Cell-Free Systems: Designing Artificial Environments for Membrane Proteins. *Eng. Life Sci.* **2014**, *14* (4), 365–379. https://doi.org/10.1002/elsc.201300050.

(130)   Stepien, P.; Polit, A.; Wisniewska-Becker, A. Comparative EPR Studies on Lipid Bilayer Properties in Nanodiscs and Liposomes. *Biochim. Biophys. Acta BBA - Biomembr.* **2015**, *1848* (1, Part A), 60–66. https://doi.org/10.1016/j.bbamem.2014.10.004.

(131)   Rideau, E.; Dimova, R.; Schwille, P.; Wurm, F. R.; Landfester, K. Liposomes and Polymersomes: A Comparative Review towards Cell Mimicking. *Chem. Soc. Rev.* **2018**, *47* (23), 8572–8610. https://doi.org/10.1039/C8CS00162F.

(132)   Jesorka, A.; Orwar, O. Liposomes: Technologies and Analytical Applications. *Annu. Rev. Anal. Chem.* **2008**, *1* (1), 801–832. https://doi.org/10.1146/annurev.anchem.1.031207.112747.

(133)   Danmaliki, G. I.; Hwang, P. M. Solution NMR Spectroscopy of Membrane Proteins. *Biochim. Biophys. Acta BBA - Biomembr.* **2020**, *1862* (9), 183356. https://doi.org/10.1016/j.bbamem.2020.183356.

(134)   Bugge, K.; Lindorff-Larsen, K.; Kragelund, B. B. Understanding Single-pass Transmembrane Receptor Signaling from a Structural Viewpoint—What Are We Missing? *FEBS J.* **2016**, *283* (24), 4424–4451. https://doi.org/10.1111/febs.13793.

(135)   Planchard, N.; Point, É.; Dahmane, T.; Giusti, F.; Renault, M.; Le Bon, C.; Durand, G.; Milon, A.; Guittet, É.; Zoonens, M.; Popot, J.-L.; Catoire, L. J. The Use of Amphipols for Solution NMR Studies of Membrane Proteins: Advantages and Constraints as Compared to Other Solubilizing Media. *J. Membr. Biol.* **2014**, *247* (9), 827–842. https://doi.org/10.1007/s00232-014-9654-z.

(136)   Bayburt, T. H.; Grinkova, Y. V.; Sligar, S. G. Self-Assembly of Discoidal Phospholipid Bilayer Nanoparticles with Membrane Scaffold Proteins. *Nano Lett.* **2002**, *2* (8), 853–856. https://doi.org/10.1021/nl025623k.

(137)   Civjan, N. R.; Bayburt, T. H.; Schuler, M. A.; Sligar, S. G. Direct Solubilization of Heterologously Expressed Membrane Proteins by Incorporation into Nanoscale Lipid Bilayers. *BioTechniques* **2003**, *35* (3), 556–563. https://doi.org/10.2144/03353rr02.

(138)   Nath, A.; Atkins, W. M.; Sligar, S. G. Applications of Phospholipid Bilayer Nanodiscs in the Study of Membranes and Membrane Proteins. *Biochemistry* **2007**, *46* (8), 2059–2069. https://doi.org/10.1021/bi602371n.

(139)   Glück, J. M.; Wittlich, M.; Feuerstein, S.; Hoffmann, S.; Willbold, D.; Koenig, B. W. Integral Membrane Proteins in Nanodiscs Can Be Studied by Solution NMR Spectroscopy. *J. Am. Chem. Soc.* **2009**, *131* (34), 12060–12061. https://doi.org/10.1021/ja904897p.

(140)   Glover, K. J.; Whiles, J. A.; Wu, G.; Yu, N.; Deems, R.; Struppe, J. O.; Stark, R. E.; Komives, E. A.; Vold, R. R. Structural Evaluation of Phospholipid Bicelles for Solution-State Studies of Membrane-Associated Biomolecules. *Biophys. J.* **2001**, *81* (4), 2163–2171.

(141)   Foster, M. P.; McElroy, C. A.; Amero, C. D. Solution NMR of Large Molecules and Assemblies. *Biochemistry* **2007**, *46* (2), 331–340. https://doi.org/10.1021/bi0621314.

(142)   Vold, R. R.; Prosser, R. S. Magnetically Oriented Phospholipid Bilayered Micelles for Structural Studies of Polypeptides. Does the Ideal Bicelle Exist? *J. Magn. Reson.* **1996**, *113*, 267–271. https://doi.org/10.1006/jmrb.1996.0187.

(143)   Denisov, I. G.; Grinkova, Y. V.; Lazarides, A. A.; Sligar, S. G. Directed Self-Assembly of Monodisperse Phospholipid Bilayer Nanodiscs with Controlled Size. *J. Am. Chem. Soc.* **2004**, *126* (11), 3477–3487. https://doi.org/10.1021/ja0393574.

(144)   Puthenveetil, R.; Nguyen, K.; Vinogradova, O. Nanodiscs and Solution NMR: Preparation, Application and Challenges. *Nanotechnol. Rev.* **2017**, *6* (1), 111–125. https://doi.org/10.1515/ntrev-2016-0076.

(145) Bayburt, T. H.; Sligar, S. G. Membrane Protein Assembly into Nanodiscs. *FEBS Lett.* **2010**, *584* (9), 1721–1727. https://doi.org/10.1016/j.febslet.2009.10.024.

(146) Vance, J. E. Phospholipid Synthesis and Transport in Mammalian Cells. *Traffic* **2015**, *16* (1), 1–18. https://doi.org/10.1111/tra.12230.

(147) Shah, N. R.; Voisin, T. B.; Parsons, E. S.; Boyd, C. M.; Hoogenboom, B. W.; Bubeck, D. Structural Basis for Tuning Activity and Membrane Specificity of Bacterial Cytolysins. *Nat. Commun.* **2020**, *11* (1), 5818. https://doi.org/10.1038/s41467-020-19482-6.

(148) Rieth, M. D. The Best of Both Worlds: A New Lipid Complex Has Micelle and Bicelle-like Properties. *bioRxiv* **2022**, 437327. https://doi.org/10.1101/437327.

(149) Chen, Q.; Vishnivetskiy, S. A.; Zhuang, T.; Cho, M.-K.; Thaker, T. M.; Sanders, C. R.; Gurevich, V. V.; Iverson, T. M. The Rhodopsin-Arrestin-1 Interaction in Bicelles. *Methods Mol. Biol. Clifton NJ* **2015**, *1271*, 77–95. https://doi.org/10.1007/978-1-4939-2330-4_6.

(150) Homewood, C. A.; Warhurst, D. C.; Peters, W.; Baggaley, V. C. Lysosomes, PH and the Anti-Malarial Action of Chloroquine. *Nature* **1972**, *235* (5332), 50–52. https://doi.org/10.1038/235050a0.

(151) Fenteany, G.; Standaert, R. F.; Lane, W. S.; Choi, S.; Corey, E. J.; Schreiber, S. L. Inhibition of Proteasome Activities and Subunit-Specific Amino-Terminal Threonine Modification by Lactacystin. *Science* **1995**, *268* (5211), 726–731. https://doi.org/10.1126/science.7732382.

(152) Chen, Y.; Leng, M.; Gao, Y.; Zhan, D.; Min Choi, J.; Song, L.; Li, K.; Xia, X.; Zhang, C.; Liu, M.; Ji, S.; Jain, A.; Saltzman, A. B.; Malovannaya, A.; Qin, J.; Jung, S. Y.; Wang, Y. A Cross-Linking-Aided Immunoprecipitation/Mass Spectrometry Workflow Reveals Extensive Intracellular Trafficking in Time-Resolved, Signal-Dependent Epidermal Growth Factor Receptor Proteome. *J. Proteome Res.* **2019**, *18* (10), 3715–3730. https://doi.org/10.1021/acs.jproteome.9b00427.

(153) Tong, J.; Taylor, P.; Moran, M. F. Proteomic Analysis of the Epidermal Growth Factor Receptor (EGFR) Interactome and Post-Translational Modifications Associated with Receptor Endocytosis in Response to EGF and Stress. *Mol. Cell. Proteomics MCP* **2014**, *13* (7), 1644–1658. https://doi.org/10.1074/mcp.M114.038596.

(154) Lam, S. S.; Martell, J. D.; Kamer, K. J.; Deerinck, T. J.; Ellisman, M. H.; Mootha, V. K.; Ting, A. Y. Directed Evolution of APEX2 for Electron Microscopy and Proximity Labeling. *Nat. Methods* **2015**, *12* (1), 51–54. https://doi.org/10.1038/nmeth.3179.

(155) Hung, V.; Udeshi, N. D.; Lam, S. S.; Loh, K. H.; Cox, K. J.; Pedram, K.; Carr, S. A.; Ting, A. Y. Spatially Resolved Proteomic Mapping in Living Cells with the Engineered Peroxidase APEX2. *Nat. Protoc.* **2016**, *11* (3), 456–475. https://doi.org/10.1038/nprot.2016.018.

(156) Hung, V.; Lam, S. S.; Udeshi, N. D.; Svinkina, T.; Guzman, G.; Mootha, V. K.; Carr, S. A.; Ting, A. Y. Proteomic Mapping of Cytosol-Facing Outer Mitochondrial and ER Membranes in Living Human Cells by Proximity Biotinylation. *eLife* **2017**, *6*, e24463. https://doi.org/10.7554/eLife.24463.

(157) Lobingier, B. T.; Hüttenhain, R.; Eichel, K.; Miller, K. B.; Ting, A. Y.; von Zastrow, M.; Krogan, N. J. An Approach to Spatiotemporally Resolve Protein Interaction Networks in Living Cells. *Cell* **2017**, *169* (2), 350-360.e12. https://doi.org/10.1016/j.cell.2017.03.022.

(158) Deb, T. B.; Su, L.; Wong, L.; Bonvini, E.; Wells, A.; David, M.; Johnson, G. R. Epidermal Growth Factor (EGF) Receptor Kinase-Independent Signaling by EGF*. *J. Biol. Chem.* **2001**, *276* (18), 15554–15560. https://doi.org/10.1074/jbc.M100928200.

(159)   Ozer, B. H.; Wiepz, G. J.; Bertics, P. J. Activity and Cellular Localization of an Oncogenic Glioblastoma Multiforme-Associated EGF Receptor Mutant Possessing a Duplicated Kinase Domain. *Oncogene* **2010**, *29* (6), 855–864. https://doi.org/10.1038/onc.2009.385.

(160)   Red Brewer, M.; Yun, C.-H.; Lai, D.; Lemmon, M. A.; Eck, M. J.; Pao, W. Mechanism for Activation of Mutated Epidermal Growth Factor Receptors in Lung Cancer. *Proc. Natl. Acad. Sci. U. S. A.* **2013**, *110* (38), E3595–E3604. https://doi.org/10.1073/pnas.1220050110.

(161)   Green, A. P.; Hayashi, T.; Mittl, P. R. E.; Hilvert, D. A Chemically Programmed Proximal Ligand Enhances the Catalytic Properties of a Heme Enzyme. *J. Am. Chem. Soc.* **2016**, *138* (35), 11344–11352. https://doi.org/10.1021/jacs.6b07029.

(162)   Liu, J.; Conboy, J. C. Phase Transition of a Single Lipid Bilayer Measured by Sum-Frequency Vibrational Spectroscopy. *J. Am. Chem. Soc.* **2004**, *126* (29), 8894–8895. https://doi.org/10.1021/ja031570c.

(163)   Shapiro, R. A.; Brindley, A. J.; Martin, R. W. Thermal Stabilization of DMPC/DHPC Bicelles by Addition of Cholesterol Sulfate. *J. Am. Chem. Soc.* **2010**, *132* (33), 11406–11407. https://doi.org/10.1021/ja1041012.

(164)   Bürck, J.; Wadhwani, P.; Fanghänel, S.; Ulrich, A. S. Oriented Circular Dichroism: A Method to Characterize Membrane-Active Peptides in Oriented Lipid Bilayers. *Acc. Chem. Res.* **2016**, *49* (2), 184–192. https://doi.org/10.1021/acs.accounts.5b00346.

(165)   Svergun, D. I.; Koch, M. H. J. Small-Angle Scattering Studies of Biological Macromolecules in Solution. *Rep. Prog. Phys.* **2003**, *66* (10), 1735–1782. https://doi.org/10.1088/0034-4885/66/10/R05.

(166)   Schneider, C. A.; Rasband, W. S.; Eliceiri, K. W. NIH Image to ImageJ: 25 Years of Image Analysis. *Nat. Methods* **2012**, *9* (7), 671–675. https://doi.org/10.1038/nmeth.2089.

(167)   Bolte, S.; Cordelières, F. P. A Guided Tour into Subcellular Colocalization Analysis in Light Microscopy. *J. Microsc.* **2006**, *224* (Pt 3), 213–232. https://doi.org/10.1111/j.1365-2818.2006.01706.x.

(168)   Dunn, K. W.; Kamocka, M. M.; McDonald, J. H. A Practical Guide to Evaluating Colocalization in Biological Microscopy. *Am. J. Physiol. Cell Physiol.* **2011**, *300* (4), C723-742. https://doi.org/10.1152/ajpcell.00462.2010.

(169)   Mozumdar, D.; Doerner, A.; Zhang, J. Y.; Rafizadeh, D. N.; Schepartz, A. Discrete Coiled Coil Rotamers Form within the EGFRvIII Juxtamembrane Domain. *Biochemistry* **2020**, *59* (41), 3965–3972. https://doi.org/10.1021/acs.biochem.0c00641.